

Ultracold Atomic Gases

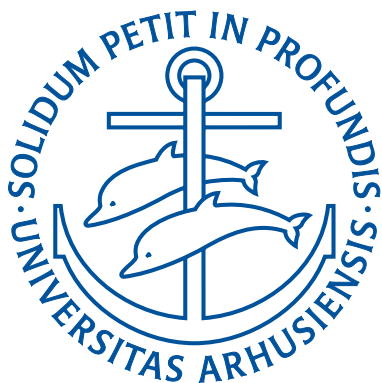
Mixtures and Molecules

Jesper Fevre Bertelsen

Danish National Research Foundation Center
for Quantum Optics (QUANTOP)

Department of Physics and Astronomy
University of Aarhus

PhD thesis
August 2007



Contents

Preface and outline	vii
1 Background	1
1.1 The Bose-Einstein Condensate	1
1.2 Atomic Quantum Gas Mixtures	3
1.3 Optical lattices	4
1.3.1 The Mott-insulator transition	5
1.3.2 Harmonic approximation of the lattice potential	8
1.3.3 Mixtures in optical lattices	8
1.4 Elastic scattering and tuning of interactions	10
1.4.1 Scattering length and bound states	10
1.4.2 Collision rates	13
1.4.3 Feshbach resonances	14
1.5 Ultracold molecules	16
1.5.1 Feshbach molecules in optical lattices	17
2 Building up a quantum gas experiment	21
2.1 Overview of the experimental setup	21
2.2 Cooling atoms	22
2.2.1 The Rubidium atom	22
2.2.2 Laser Cooling and the MOT	23
2.2.3 Compressed MOT and transfer to the magnetic trap	25
2.2.4 Optical pumping	25
2.3 The diode laser system	26
2.3.1 The Diode Lasers	27
2.3.2 Locking to an atomic resonance	28
2.3.3 Optical Table Setup	30
2.4 Trapping and moving atoms	32
2.4.1 Principles of magnetic trapping	32
2.4.2 The quadrupole trap	34
2.4.3 Moving schemes	36
2.4.4 The QUIC trap	36
2.5 Forced evaporation	37

2.6	Imaging atoms	37
2.6.1	Temperature measurements	39
2.7	Future plans	43
3	Mixing ultracold atoms	45
3.1	Purpose	45
3.2	Experimental procedure	46
3.3	Magnetic field and trapping potential	47
3.4	Classical simulation of the dynamics	52
3.4.1	Thermodynamics of the quadrupole trap	56
3.4.2	Initial conditions	60
3.5	Results	60
3.5.1	Dependence on trap current ratio	61
3.5.2	Dependence on trap depth	64
3.5.3	Theoretical dependence on the initial temperature	65
3.6	Mixing different species	66
3.7	An alternative mixing scheme	68
3.8	Conclusion	71
4	Two interacting atoms in an optical lattice well	75
4.1	Two interacting atoms in a harmonic potential	75
4.1.1	The Separating Case	76
4.1.2	The Non-separating Case	77
4.2	The Interaction Potential	80
4.3	The spectrum and the wave functions	84
4.3.1	The isotropic harmonic oscillator without interactions	84
4.3.2	The Separating Case	85
4.3.3	The Non-separating Case	89
4.4	Conclusion	92
5	Resonant Dynamics near a Feshbach resonance	95
5.1	Dynamical equations	97
5.2	Small amplitude modulations	100
5.2.1	Adiabatic passages	104
5.2.2	Three-level resonances	104
5.3	Large amplitude modulations	105
5.3.1	Association spectra	106
5.4	Associating heteronuclear molecules	112
5.5	Creating nonzero angular momentum states	112
5.6	Conclusion	115
6	Conclusion and Outlook	117
7	Acknowledgements	119

A Appendix: Optical table setup	121
B Appendix: Two interacting particles in an external harmonic oscillator	123
C Appendix: Calculation of matrix elements	129
C.1 The angular integral	130
C.2 The overlap of two parabolic cylinder wave functions	131
C.3 The radial integral for harmonic oscillator wave functions	132
C.4 Matrix element with parabolic cylinder and harm. osc. functions	133
D List of abbreviations	135

Preface and outline

This thesis is presented for the Faculty of Science at the University of Aarhus, Denmark in order to fulfill the requirements for the PhD degree in physics. It summarizes the work that I have carried out under supervision of Michael Budde and Klaus Mølmer at the Department of Physics and Astronomy since 2003.

When I joined Michael's new quantum gas group in the spring 2003, the starting point was an empty laboratory and the first goal was to produce a Bose-Einstein condensate of ^{87}Rb atoms (we achieved that in March 2006). I spent the first one and a half year building up various parts of the experimental setup in close collaboration with Michael and Henrik Kjaer Andersen who is another PhD student in our group. Since then, Sune Mai has also joined us, first as a master student in 2006 and now as a PhD student. My main contribution is the setup of the laser system that we use to cool and image rubidium atoms, but I have been involved in most parts of the experimental setup to a greater or lesser degree.

During my time as a PhD student I have fortunately also had the opportunity to do quite a bit of theory work in collaboration with Klaus. Initially we believed that this work was going to be a support for our experimental plans in the quantum gas group. In the end, however, it has become more or less uncoupled from our current experiment, at least in the short-term perspective.

The outline of the thesis is as follows: In chapter 1, I begin with a brief, general introduction to ultracold atomic physics and the concepts used later on. My intention is not to attempt a general review of the field (that would be a formidable task) but rather to set the stage for the presentation of my contribution described in the later chapters. Therefore, the main focus is on quantum gas mixtures, optical lattices, and creation of ultracold molecules using Feshbach resonances. After the introduction, the work presented in this thesis can be divided into three major parts:

- I introduce the experimental setup in chapter 2. A complete account of our experimental setup would be a thesis in itself so the chapter

necessarily focuses on topics that I have been directly involved in and which are relevant for the rest of the thesis: The laser system, the magnetic quadrupole trap, and time-of-flight imaging. On the other hand, important parts of the experiment such as the computer control system are hardly mentioned.

- Chapter 3 deals with a novel scheme for producing mixtures of ultracold atoms that I have studied intensively through experiments and computer simulations. I have mixed two clouds of ultracold atoms, caught in two different magnetic quadrupole traps, by merging the two traps. The essential results are also published in [1].
- Chapter 4 and 5 are purely theoretical and cover the work that I have carried out in collaboration with Klaus. In chapter 4 I solve a model for two interacting atoms in a harmonic oscillator potential in the homonuclear as well as in the heteronuclear case. In chapter 5, the model is applied to creation of molecules in an optical lattice well using a resonantly oscillating magnetic field and some interesting dynamical phenomena are discussed. Some parts of the work are published in [2] and other parts have just been accepted for publication [3].

Even though the three topics can be regarded as independent, there are also strong relationships among them: My experimental work on the new mixing process for thermal clouds of atoms suggests an alternative way of producing quantum gas mixtures that our quantum gas group can use to create quantum degenerate mixtures of rubidium and lithium atoms in the future. It is also the plan to put this mixture into an optical lattice (Henrik is currently finalizing an optical lattice setup). A quantum gas mixture is a prerequisite for producing heteronuclear molecules and solving a model for creation of heteronuclear molecules in an optical lattice well was a major challenge in my theoretical work on molecule creation. Furthermore, I spent 5 months at JILA at the University of Colorado working on one of the rubidium-potassium mixture experiments in the group of Debbie Jin where we managed to use a Feshbach resonance to produce heteronuclear molecules.

I give a general conclusion in chapter 6. Last, but not least, there are several people whom I want to thank in chapter 7. A list of abbreviations can be found in Appendix D.

Jesper Fevre Bertelsen
Aarhus, August 2007

A few misprints have been corrected and the references have been updated in this printing (September 2007).

Chapter 1

Background

1.1 The Bose-Einstein Condensate

A Bose-Einstein condensate (BEC) is a collection of bosonic particles where a macroscopic number of them are occupying a definite single-particle quantum state (see e.g. [4–6]). It is a prominent example of a macroscopic quantum phenomena. In general, a necessary condition for macroscopic quantum phenomena to show up is that the de Broglie wavelength $\lambda_{\text{dB}} = h/\sqrt{2\pi mkT}$ where k is Boltzmann's constant, h is Planck's constant, m is the particle mass and T is the temperature (one might roughly think of it as the spatial extension of a quantum state) becomes comparable to the inter-particle spacing. Introducing the phase space density $n\lambda_{\text{dB}}^3$ where n is the particle density, we have

$$n\lambda_{\text{dB}}^3 = n \left(\frac{h^2}{2\pi mkT} \right)^{3/2} \gtrsim 1 \quad (1.1)$$

If we isolate the temperature

$$T \lesssim \frac{h^2}{2\pi mk} n^{2/3} \quad (1.2)$$

we see that macroscopic quantum phenomena are inherently low temperature phenomena. However, for light particles at high densities, the temperature in (1.2) can be quite high. For instance for free electrons in metals ($n \approx 10^{22} \text{ cm}^{-3}$) it is on the order of 10^4 K so they are quantum degenerate already at room temperature and many properties of metals - e.g. their incompressibility and their heat capacity - can be regarded as macroscopic quantum phenomena [7].

At temperatures below about 2 K, liquid ^4He undergoes a transition to a superfluid state which can be regarded as a BEC [5, 6, 8]. However, the atoms in liquid helium are strongly interacting and far from the ideal case of noninteracting bosons. Furthermore, although neutron scattering can be

used to obtain some information about the superfluid phase [8], it is impossible to obtain a very detailed knowledge about this system experimentally.

In contrast to that, the atomic vapor quantum gases which have been created in laboratories since 1995 are very dilute which means that the interatomic interactions are weak and that the sample is sufficiently optically transparent that the cloud can be imaged with laser light. The price to pay for the diluteness is a much lower transition temperature (see 1.2), but this obstacle can be overcome, because dilute clouds of some elements can be laser cooled (see Ch. 2).

The first BEC of this kind contained about 2×10^4 ^{87}Rb atoms and was produced in the group of Carl Wieman and Eric Cornell at JILA in 1995 [9, 10] and shortly after, condensates with up to 5×10^5 ^{23}Na atoms were produced at MIT in the group of Wolfgang Ketterle [11, 12]. During the latest years a few monographs on BECs have emerged [5, 13, 14].

BECs of dilute atomic gases are almost exclusively made of alkali metal isotopes (^7Li [15], ^{23}Na [11], ^{39}K [16], ^{41}K [17], ^{85}Rb [18], ^{87}Rb [9], and ^{133}Cs [19]) because well established laser cooling and magnetic trapping techniques can be applied to the stable isotopes. ^{87}Rb is very popular because it can be laser cooled at a wavelength that is suitable for cheap and stable diode lasers and because it has a favorable ratio of elastic to inelastic collision rate which makes evaporative cooling feasible. The alkali metal-like ^4He in the metastable ^3P state has also been condensed [20, 21] as well as ^1H [22] and ^{52}Cr [23].

Atomic quantum gases are made in magnetic or optical traps which are typically harmonic at the trap bottom:

$$V(x, y, z) = \frac{1}{2}m(\omega_x^2 x^2 + \omega_y^2 y^2 + \omega_z^2 z^2) \quad (1.3)$$

For bosons confined in a harmonic potential the condensation temperature is given by [5]

$$kT_c = \hbar \left(\frac{\omega_x \omega_y \omega_z}{\zeta(3)} N \right)^{1/3} + \mathcal{O}(N^0) \approx 0.94 \hbar (\omega_x \omega_y \omega_z N)^{1/3} + \mathcal{O}(N^0) \quad (1.4)$$

In our experimental setup we typically have a radial harmonic oscillator frequency of $\omega_x = \omega_y = 2\pi \times 224$ Hz and an axial frequency of $\omega_z = 2\pi \times 16.2$ Hz yielding a condensation temperature of $T_c = 0.2$ μK for 2×10^5 atoms. But it should be said that interactions cause a shift in the transition temperature [24].

A brief review of the BEC setup that we have built in our laboratory is given in Ch. 2. For more details on how to make a BEC, see [25, 26]. A recent review on modern topics in the field of ultracold quantum gases including Feshbach resonances and optical lattices can be found in [27].

1.2 Atomic Quantum Gas Mixtures

Today there are several quantum gas laboratories that cool down mixtures of two elements into the quantum regime. A main reason for the interest in mixtures is that a gas of spin-polarized fermions cannot be evaporatively cooled because there are no s-wave collisions to thermalize the sample due to the Pauli exclusion principle (because of the centrifugal barrier, higher partial wave collisions are thermally suppressed at the ultralow temperatures needed). But a bosonic gas can be used to sympathetically cool down a fermionic gas since only collisions between identical fermions are subject to the Pauli exclusion principle. Thereby mixtures of ^{87}Rb (boson) and ^{40}K (fermion) as well as mixtures of $^{23}\text{Na}/^6\text{Li}$, $^{87}\text{Rb}/^6\text{Li}$, $^7\text{Li}/^6\text{Li}$ and most recently $^4\text{He}/^3\text{He}$ have been used to create a degenerate atomic Fermi gas (for references see Tab. 1.1). However, it is also possible to evaporatively cool a spin mixture of a fermionic isotope as demonstrated in [28] since fermions with different spins are not identical.

Today quantum gas mixtures are also studied in their own right. Theoretical predictions of collapse and phase separation phenomena have been around for a while [29, 30] and these phenomena have recently been observed experimentally [31, 32]. Theory also predicts that mixtures in optical lattices should be able to exhibit an extraordinarily rich collection of quantum phases with or without analogies in condensed matter [33, 34]. Furthermore, there is a large interest in creating heteronuclear molecules because they have a permanent dipole moment [35, 36]. Dipolar molecules can be used to make sensitive measurements of some of the constants of nature like the electrical dipole moment of the electron [37] and quantum computing schemes using heteronuclear molecules in optical lattices have also been proposed [38, 39].

Experimentally the most well studied mixture is $^{87}\text{Rb}/^{40}\text{K}$. This is due to the fact that Rb and K are very similar from a cooling and trapping point of view so almost the same kind of optics and laser technology can be used for the two elements [40, 41]. Furthermore the large magnitude of the inter-species scattering length ($|a_{\text{RbK}}| = 250 a_0$ for ^{87}Rb in the $|F = 2, m_F = 2\rangle$ hyperfine state and ^{40}K in the $|F = 9/2, m_F = 9/2\rangle$ state [42]) makes sympathetic cooling quite efficient. Besides the boson-fermion mixtures mentioned above, boson-boson mixtures such as $^{87}\text{Rb}/^{85}\text{Rb}$ [43] and $^{87}\text{Rb}/^7\text{Li}$ [44] have also been prepared in the quantum regime and they can also be used to condense isotopes which are otherwise difficult to condense as demonstrated for ^{41}K mixed with ^{87}Rb [17] and lately also for ^{39}K mixed with ^{87}Rb [16]. The mixtures mentioned above are summarized in Tab. 1.1. Several other mixtures in the ultracold, but not yet quantum, regime have been studied (see e.g. [45–52]).

Even if the goal is to enter the quantum regime by means of evaporative

Boson 1	Fermion 2	Boson 2	References
^{87}Rb	^{40}K		[53–55]
^{87}Rb		^{41}K	[17]
^{87}Rb		^{39}K	[16]
^{87}Rb	^6Li		[56]
^{87}Rb		^7Li	[44]
^{87}Rb		^{85}Rb	[43, 57]
^{23}Na	^6Li		[58]
^7Li	^6Li		[59, 60]
^4He	^3He		[61]

Table 1.1: List of some binary atomic quantum gas mixtures that have been produced in experiments.

cooling, the starting point is a mixture which has already been cooled to the 100 μK regime by means of laser cooling. The standard approach used to produce such cold mixtures is to cool and trap the two [41, 51, 62] or even three [63] species simultaneously in the same magneto-optical trap (MOT). This method is simple in principle and it works very well for $^{87}\text{Rb}/^{40}\text{K}$ mixtures, but it also has some drawbacks. First of all the two species generally affect each other (see e.g. [46, 51, 62, 64]) and it might not be possible to optimize the cooling and trapping process independently for the two species. Another drawback is that the experimental setup has to be designed for two specific species from the beginning. It can be difficult to add a second species to an already existing setup. Furthermore in the case of species of two different elements, the wavelength of the cooling transitions are differing by several nm meaning that one either has to use optics which can handle both wavelengths or to use two sets of cooling beams which is typically unpractical due to limited optical access around the glass cell where the atoms are cooled. This led us to investigate the potential of a new way of producing ultracold mixtures (Ch. 3).

1.3 Optical lattices

The presence of laser light coupling to atomic transitions slightly perturbs the atomic energy levels. This gives rise to the so-called light shift or AC stark shift. A consequence of the light shift is that an atom at a point with light intensity I will feel a potential. For a 2-level atom the potential is [65]:

$$V(\mathbf{r}) = \frac{3\pi c^2}{2\omega_0^3} \frac{\Gamma}{\Delta} I(\mathbf{r}) \quad (1.5)$$

where ω_0 is the atomic transition angular frequency, Γ the linewidth of the transition, $\Delta = \omega_{\text{laser}} - \omega_0$ is the detuning from resonance, and c is the speed of light.

For linearly polarized light, a generalization of this simple formula to include both the D1 ($S_{1/2} \rightarrow P_{1/2}$) and D2 ($S_{1/2} \rightarrow P_{3/2}$) transitions from the ground state term in alkali metal atoms while still neglecting the hyperfine structure of the excited states reads [65]

$$V(\mathbf{r}) = \frac{\pi c^2 \Gamma}{2\omega_0^3} \left(\frac{2}{\Delta_{D2}} + \frac{1}{\Delta_{D1}} \right) I(\mathbf{r}) \quad (1.6)$$

Here ω_0 is the transition frequency without fine structure and Δ_{D1} and Δ_{D2} are the detunings from the D1 respectively D2 transition frequencies.

Experimentally optical lattices are made of the standing waves of laser light produced by two counter-propagating beams. In the middle of a single standing wave with a Gaussian beam profile and wavelength λ the intensity is

$$I(x) = I_0 \sin^2(kx) \quad k = \frac{2\pi}{\lambda} \quad (1.7)$$

Ultracold atoms in this standing wave will feel a $\lambda/2$ -periodic potential due to the light shift (1.6)

$$V(x) = V_0 \sin^2(kx), \quad V_0 = \frac{\pi c^2 \Gamma}{2\omega_0^3} \left(\frac{2}{\Delta_{D2}} + \frac{1}{\Delta_{D1}} \right) I_0 \quad (1.8)$$

Depending on the sign of the detuning, this potential drives the atoms towards either intensity minima (blue detuning) or intensity maxima (red detuning) of the standing wave and the atoms will arrange in pancake structures. Similarly, two orthogonal standing wave laser beams with orthogonal polarizations can be used to confine atoms in rod like structures and three orthogonal laser beams with mutually orthogonal polarizations will lead to a cubic lattice. This is illustrated in Fig. 1.1.

1.3.1 The Mott-insulator transition

Ultracold bosons in an optical lattice are phenomenologically well described by the so-called Bose-Hubbard model which is difficult to solve but gives a good intuitive picture of the behaviour of the system. In that model, the many-body Hamiltonian of the system in second quantized notation reads [66]

$$H = \sum_i \epsilon_i a_i^\dagger a_i - J \sum_{\langle ij \rangle} a_i^\dagger a_j + \frac{1}{2} U \sum_i a_i^\dagger a_i (a_i^\dagger a_i - 1) \quad (1.9)$$

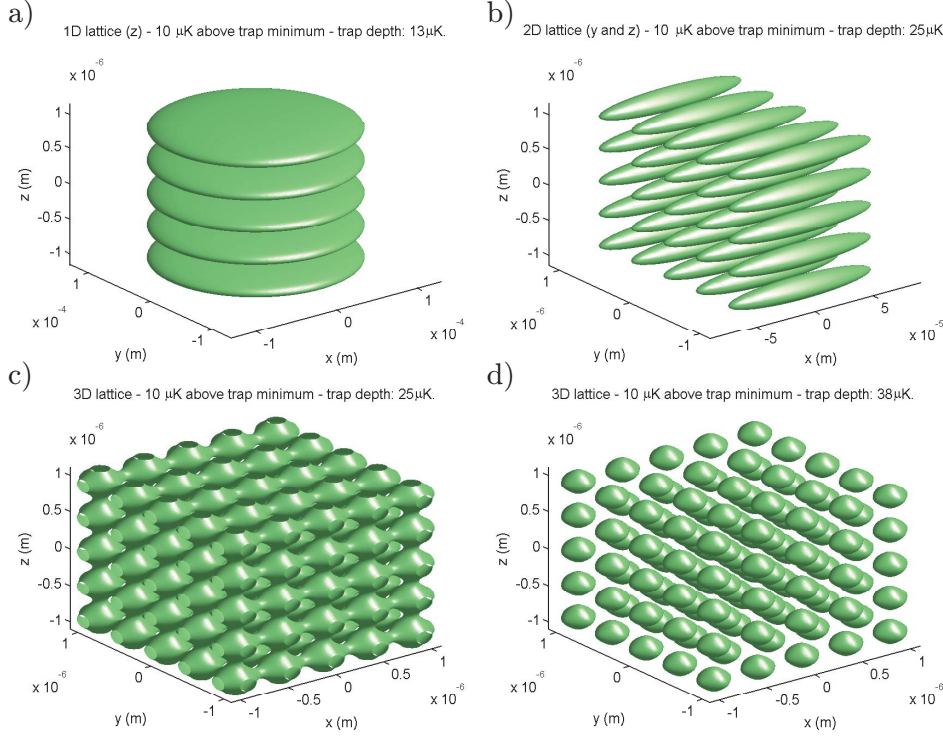


Figure 1.1: Isosurfaces of the potential energy of an atom in 1D, 2D and 3D optical lattices. It shows that if the atoms are cooled enough they will arrange in disks in a 1D lattice (a), in thin cylinders in a 2D lattice (b) and in a simple cubic structure in a 3D lattice (c) and (d). The figure is kindly provided by Henrik Kjaer Andersen who made them from calculations on the 920 nm optical lattice that he has set up in our laboratory.

where i is the lattice site index, a_i^\dagger and a_i are the bosonic operators for creation and annihilation of an atom on site i and $\sum_{\langle ij \rangle}$ denotes summation of nearest neighbour lattice sites. The first term is the trapping potential which each atom feels. The second term describes quantum mechanical tunneling of atoms from one lattice site to its nearest neighbour characterized by the tunneling energy J . The last term includes the energy due to the on-site interaction of the atoms and is characterized by the energy U .

The ratio U/J is crucial for the state of system. This is because the on-site interaction tends to confine the atoms at single sites thus favoring a quantum state with a well-defined number of atoms in each well, whereas the tunneling tends to spread out the atoms and restore the phase coherence among different lattice sites thus favoring a superfluid state.

If a BEC is loaded into an optical lattice with a small value of U/J , the tunneling dominates over the interaction such that the system is still in a

phase coherent superfluid state. If the lattice potential is increased, U/J will increase and it turns out that if this ratio reaches a critical value, the system undergoes a phase transition from the superfluid phase, to a state with a well defined number of atoms in each lattice well, a so-called Mott-insulating state. In a quantum optics terminology, the coherent BEC state which has a Poissonian number distribution turns into a number state. The Mott-insulator transition in an atomic quantum gas was suggested in [66] and demonstrated experimentally for the first time in the famous paper [67] by Greiner et al.

An important reason why optical lattices are interesting is that there are clear analogies between atomic quantum gases in optical lattices and electrons in crystalline solids, simply because both are quantum gases in periodic potentials. This means that well known concepts from solid state physics such as band structure can be applied to atoms in lattices [68, 69] and the Mott-insulator transition is somewhat similar to the conductor-insulator transition in solid state physics (the superfluid state where the atoms can move freely around representing the conductor and the Mott-insulator where the atoms are confined in the wells representing the insulator). Whereas I will not make use of the specific properties of the Mott-insulator transition in this thesis, its existence is crucial for the validity of the theoretical model in Ch. 4-5.

One of the virtues of optical lattices is that several physical parameters that would be fixed in a condensed matter system can be adjusted continuously in an experiment. The depth of the lattice can be controlled by varying the power of the standing wave laser beams, the interatomic interaction can be adjusted with the help of Feshbach resonances as described in Sec. 1.4. Even the effective dimensionality can be changed: For instance in a 3-dimensional lattice where the intensity of two of the three standing wave laser beams is sufficiently large, the atoms will be confined in one dimension since they are forced into the motional ground state in the two other directions. Such 1-dimensional systems are currently subject to intensive research since the scattering properties of atoms confined in one dimension are quite different from the scattering properties in the 3-dimensional case [70]. For instance under suitable conditions bosons that are confined to one dimension might form a so-called Tonks-Girardeau gas where they behave somewhat like fermions. This was realized experimentally for the first time in an optical lattice experiment in 2004 [71]. Due to this large tunability of physical parameters, ultracold atoms in lattices may be used to improve the understanding of, or even simulate, condensed matter systems that cannot be solved theoretically [34].

1.3.2 Harmonic approximation of the lattice potential

The potential for a cubic and isotropic, 3D optical lattice can be written

$$V(\mathbf{r}) = V_0 \sum_{i=x,y,z} \sin^2(kx_i) \quad (1.10)$$

where $k = 2\pi/\lambda$ is the length of the wave vector of the lattice light. If the lattice is sufficiently deep ($V_0 \gg J$) atoms placed in the lattice will be in a Mott-insulating state as described in section 1.3. In this situation there is a well defined number of atoms in each well and they do not interact strongly with atoms in the other wells. Placing the origin of our coordinate system in a specific well, the expansion of the lattice potential (1.10) to second order in x , y and z is

$$V(\mathbf{r}) \simeq V_0 k^2 \sum_{i=x,y,z} x_i^2 = V_0 k^2 r^2 = \frac{1}{2} m \omega^2 r^2, \quad \omega = \sqrt{\frac{2V_0 k^2}{m}} \quad (1.11)$$

where m is the mass of each atom. This harmonic approximation is valid provided that the well is deep enough to contain several bound states and that the temperature is low enough that only states at the bottom of the well are occupied: $kT \lesssim \hbar\omega \ll V_0$. The last inequality can be written $V_0 \gg 2(\hbar k)^2/m$ meaning that the lattice depth has to be much larger than four times the recoil energy of scattering with a lattice photon. Normally this is already fulfilled to a reasonable extent in the Mott-insulating state. For instance the superfluid to Mott-insulator transition of ^{87}Rb in [67] happens at 13 recoil energies. This corresponds to a lattice frequency of $\omega = 2\pi \times 23$ kHz at the 852 nm lattice wavelength used in [67]. At this frequency the first inequality implies $T \lesssim 1.1 \mu\text{K}$ which can be achieved if a BEC is loaded adiabatically into an optical lattice.

1.3.3 Mixtures in optical lattices

Mixtures in optical lattices is a rather new field of study. The first experiments which dealt with $^{87}\text{Rb}/^{40}\text{K}$ were reported in 2006 [72]. One of our long term goals is to study Rb-Li mixtures in an optical lattice.

When one has to settle for a lattice wavelength for an ultracold mixture there are several concerns to take into account. First of all, the AC stark shift needs to have the same sign if one wants to have atoms of both elements in the same lattice wells. This limits the wavelength to the ranges $\lambda < 671$ nm and $\lambda > 795$ nm in the case of Rb/Li. One could aim for having the same overall confinement of the two species, that is, the same $m\omega^2$, but if the extension of the ground state wave functions has to be the same, it is $m\omega$ that should be equal. Another feature that one could aim for is to have the same ω since this leads to separation of the center-of-mass and relative dynamics

of two atoms at a site (see Ch. 4) but this is not compatible with having the same lattice depth. Finally, but maybe most important, some wavelengths are more easily accessible using standard laser technology than others. Today, lattices are typically made either by diode lasers with power amplifiers in the 800 – 900 nm range or by Yttrium Aluminum Garnet (YAG) or fiber lasers having a wavelength in the 1000 – 1100 nm range. We have ended up using 920 nm which gives a lattice depth ratio of $m_{\text{Li}}\omega_{\text{Li}}^2/(m_{\text{Rb}}\omega_{\text{Rb}}^2) = 0.29$ and a confinement frequency ratio of $\omega_{\text{Li}}/\omega_{\text{Rb}} = 2.0$.

Different gravitational sag is also a serious problem when one wants to confine elements with a large mass ratio in the same region of the lattice. Therefore it might be necessary to confine the atoms in a strong magnetic or optical dipole trap in addition to the lattice.

The ratio of lattice depths and harmonic oscillator frequencies for Rb and Li is shown in Fig. 1.2 as a function of the lattice wavelength.

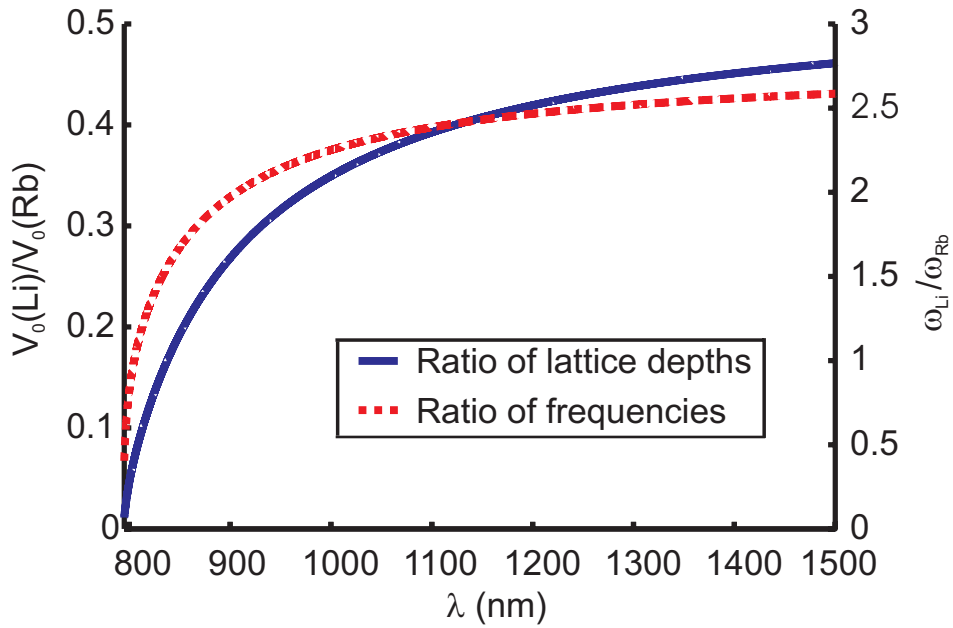


Figure 1.2: Ratio of lattice depths $V_0 = m\omega^2$ and frequencies ω for Rb and Li in an optical lattice with wavelengths from 795 to 1500 nm. The connected, blue line shows $V_0(\text{Li})/V_0(\text{Rb})$ while the red, dotted line shows $\omega_{\text{Li}}/\omega_{\text{Rb}}$.

1.4 Elastic scattering and tuning of interactions

1.4.1 Scattering length and bound states

Scattering of ultracold atoms is a huge subject and I will only briefly review the part of it which is absolutely necessary for the topics in this thesis. More comprehensive treatments can be found in e.g. [5, 73, 74].

The stationary Schrödinger equation for the reduced wave function $u \equiv r\psi$ in a spherically symmetric potential $V(r)$ reads [75, 76]

$$-\frac{\hbar^2}{2\mu} \frac{\partial^2 u}{\partial r^2} + \frac{\hbar^2 l(l+1)}{2\mu r^2} u + V(r)u = Eu \quad (1.12)$$

where μ is the reduced mass, l is the orbital angular momentum and E the energy. For energies much smaller than the potential barrier, that is for $E \ll \hbar^2 l(l+1)/(2\mu R^2)$ where R is a measure of the range of the potential, we can neglect elastic scattering altogether since the particles do not have enough energy to overcome the centrifugal barrier. For partial waves with $l \geq 1$ this inequality will be fulfilled if the temperature is sufficiently low whereas for s-waves it will never be fulfilled since the centrifugal barrier vanishes completely. In the rest of this thesis I will assume that the temperature is always so low that two atoms can only scatter if they are in an s-wave state so we shall discard the centrifugal barrier term in 1.12.

In the extreme low energy limit $E = 0$ (or to be more precise, in the limit $kr \ll 1$ where $k = \sqrt{2mE}/\hbar$ is the wave vector), we might neglect the energy term altogether and write the stationary Schrödinger equation for s-waves as

$$\frac{\hbar^2}{2\mu} \frac{\partial^2 u}{\partial r^2} = Vu \quad (1.13)$$

If we choose the phase such that the wave function is real, this means that the curvature of the wave function has the same sign as the wave function itself in regions where the potential is repulsive and the opposite sign in regions where the potential is attractive. Outside the range of the potential, the curvature is zero and u has to be linear such that

$$\psi(r) = \frac{u(r)}{r} = \frac{b(r-a)}{r} = b \left(1 - \frac{a_{\text{sc}}}{r} \right) \quad (1.14)$$

where a_{sc} and b are real constants. We will take a_{sc} which is the intersection of (the extension of) this line with the r -axis to be the definition of the scattering length. Of course, all these considerations hold only out to the distance from the origin where the inequality $kr \ll 1$ breaks down. Eventually normalizability requires $u(r) \rightarrow 0$ for $r \rightarrow \infty$.

Armed with the information above we can already draw the shape of the wave function for different kinds of potentials (this analysis is somewhat

similar to the one in [73] p. 413). Consider a finite-ranged potential which is repulsive for small distances and attractive further out like the one shown in Fig. 1.3. If the strength of the repulsive part is unchanged while the depth of the attractive part of the potential increases, the shape of the wave function will change as sketched in Fig. 1.4 (a)-(d). If the attractive part is weak, it changes the slope of the wave function very little according to (1.13) such that the scattering length will be positive (Fig. 1.4 (a)). As we increase the strength of the attraction, the scattering length decreases and becomes negative (Fig. 1.4 (b)). If we continue to increase the depth of the attraction, the scattering length continues to decrease towards $-\infty$ until a certain critical point where it flips from $-\infty$ to ∞ (Fig. 1.4 (c)) whereafter the scattering length becomes positive again (Fig. 1.4 (d)).

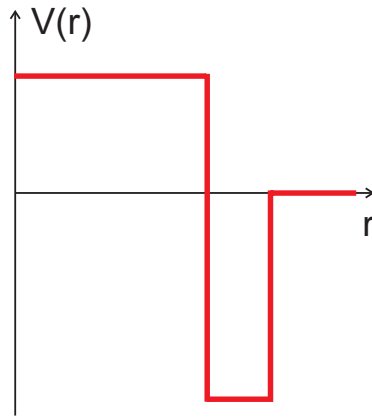


Figure 1.3: The model potential discussed in the text.

In Fig. 1.4 (d) we see that a node has been created in the wave function. This indicates that an extra bound state has been added to the Hilbert space (cf. the node theorem [77]). The bound state has an energy very close to the threshold $E = 0$ and because solutions to the Schrödinger equation evolve continuously with E [73], its energy will be closely related to the scattering length. The connection is seen by comparing the linear scattering solution and a bound state solution outside the range of the potential. Here, the Schrödinger equation reads

$$\frac{-\hbar^2}{2\mu} \frac{\partial^2 u}{\partial r^2} = Eu \quad (1.15)$$

which has the bound state solution

$$\psi(r) = A \frac{e^{-\kappa r}}{r}, \quad \kappa = \frac{\sqrt{-2\mu E_{\text{bound}}}}{\hbar} \quad (1.16)$$

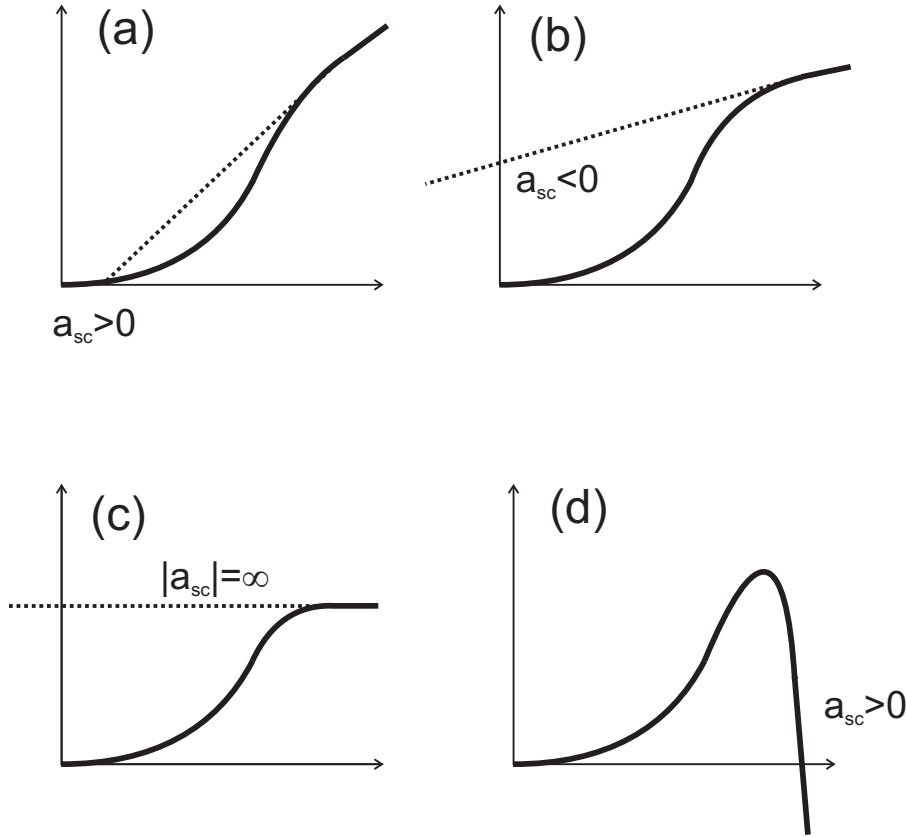


Figure 1.4: Change of the shape of the wave function for the model potential in Fig. 1.3 as the depth of the attractive part of the potential is increased. The figures are explained in the text.

where A is a normalization constant. In the limit of low binding energy $\kappa r \ll 1$ we have the following asymptotic expansion

$$\psi(r) \simeq \frac{A(1 - \kappa r)}{r} = \frac{-A\kappa(r - 1/\kappa)}{r} = -A\kappa \left(1 - \frac{1}{\kappa r}\right) \quad (1.17)$$

Continuity of the solutions of the Schrödinger equation requires that this wave function is identical to the one in 1.14 so

$$a_{sc} = \frac{1}{\kappa} = \frac{\hbar}{\sqrt{-2\mu E_{\text{bound}}}} \quad (1.18)$$

so we have the following universal relation between the scattering length and the binding energy of threshold bound states

$$\text{Binding energy of threshold bound state: } -E_{\text{bound}} = \frac{\hbar^2}{2\mu a_{sc}^2} \quad (1.19)$$

In summary the above analysis reveals the following points about ultracold s-wave scattering which are important for the understanding of Feshbach resonances:

- The scattering length a_{sc} of an attractive potential can both be positive and negative and the magnitude can be much larger than the range of the potential (100 a_0 is a typical order of magnitude for ultracold atoms).
- Even a slight tuning of the shape of the potential can cause the scattering length to change abruptly from $-\infty$ to ∞ or vice versa.
- On the positive scattering length side of such a scattering resonance, the potential supports an extra bound state (that is, a molecular state) with the binding energy $\hbar^2/(2\mu a_{\text{sc}}^2)$.

1.4.2 Collision rates

The cross section for low-energy s-wave elastic scattering of non-identical particles (which might be two different isotopes or the same isotope in two different hyperfine states) is [5, 73]

$$\sigma_{\text{non-identical}} = 4\pi a_{\text{sc}}^2 \quad (1.20)$$

whereas due to symmetrization of the wave function, the elastic scattering cross section for identical bosons (that is, the same isotope in the same hyperfine state) is twice as large [5]:

$$\sigma_{\text{identical bosons}} = 8\pi a_{\text{sc}}^2. \quad (1.21)$$

The cross section for elastic scattering of two identical fermions becomes zero due to anti-symmetrization of the wave function [5].

The elastic collision rate is given by

$$\gamma = \langle n \rangle \sigma \langle v_{\text{rel}} \rangle \quad (1.22)$$

where $\langle n \rangle$ is the mean density, σ is the elastic collision cross section above and $\langle v_{\text{rel}} \rangle$ is the mean value of the relative velocities of the colliding atoms. To calculate $\langle v_{\text{rel}} \rangle$ we consider a gas with atoms of mass m_1 and m_2 in thermal equilibrium (it could be a mixture or a gas of identical atoms in which case $m_1 = m_2$). The thermal equilibrium velocity distribution is Gaussian in each Cartesian direction, let us look at the x direction:

$$p(v_{1x}) \propto \exp\left[-\beta \frac{1}{2} m_1 v_{1x}^2\right], \quad p(v_{2x}) \propto \exp\left[-\beta \frac{1}{2} m_2 v_{2x}^2\right] \quad (1.23)$$

where $\beta = 1/(kT)$ so the distribution of the relative velocity $v_x = v_{1x} - v_{2x}$ is given by the convolution

$$\begin{aligned}
p(v_x) &\propto \int_{-\infty}^{\infty} \exp\left[-\beta\frac{1}{2}m_1(v_x + v_{2x})^2\right] \exp\left[-\beta\frac{1}{2}m_2v_{2x}^2\right] dv_{2x} \\
&= \exp\left[-\beta\frac{1}{2}m_1v_x^2\right] \int_{-\infty}^{\infty} \exp\left[-\beta\frac{1}{2}v_{2x}^2(m_1 + m_2) - \beta m_1 v_x v_{2x}\right] dv_{2x} \\
&= \exp\left[-\beta\frac{1}{2}m_1v_x^2\right] \int_{-\infty}^{\infty} \exp\left[-\beta\frac{1}{2}\left(\sqrt{m_1 + m_2} v_{2x} + \frac{m_1}{\sqrt{m_1 + m_2}} v_x\right)^2\right. \\
&\quad \left. + \beta\frac{1}{2}\frac{m_1^2}{m_1 + m_2}v_x^2\right] dv_{2x} \\
&\propto \exp\left[-\beta\frac{1}{2}\left(m_1 - \frac{m_1^2}{m_1 + m_2}\right)v_x^2\right] \\
&= \exp\left[-\beta\frac{1}{2}\mu v_x^2\right] \tag{1.24}
\end{aligned}$$

where $\mu = m_1m_2/(m_1 + m_2)$ is the reduced mass. So the distribution of relative velocities is the same as the distribution of single atom velocities except that the mass is replaced by the reduced mass. In particular, the mean relative velocity is given by (see [6]):

$$\langle v_{\text{rel}} \rangle = \sqrt{\frac{8kT}{\pi\mu}} \tag{1.25}$$

1.4.3 Feshbach resonances

As illustrated above, any mechanism that modifies the shape of the interatomic potential can cause a scattering resonance under suitable conditions. Magnetic Feshbach resonances is an important example of such a resonance. An external magnetic field can be used to change the shape of the interatomic potential because it couples states in different scattering channels through a second order perturbation (I refer to an interatomic potential curve of two atoms as a scattering channel). This coupling is typically weak, but, as one would expect for a second order perturbation, it exhibits a singular behaviour if the energy of the free atom channel matches the energy of a molecular state in another channel. This is illustrated schematically in Fig. 1.5. If the total magnetic moment is different for the two channels, a magnetic field can be used to shift them with respect to each other to tune the energy difference between them. By tuning this energy difference, the scattering length can be tuned through a resonance.

A Feshbach resonance can be characterized by three parameters: Its position B_0 , its width Δ (both given in terms of a magnetic field) and the

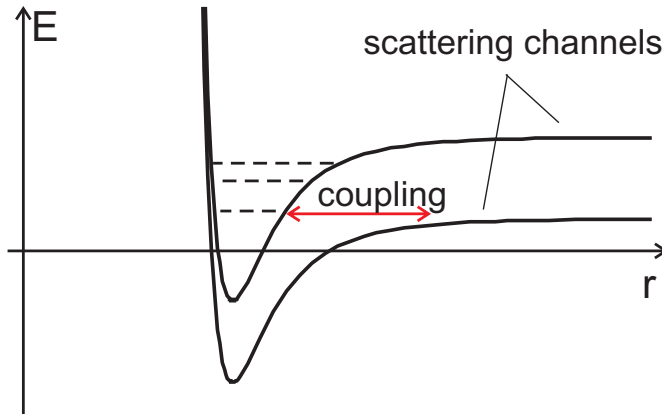


Figure 1.5: The principle of a Feshbach resonance illustrated with interatomic potentials. Normally two free atoms in a definite channel do not couple strongly to states in other scattering channels. However, if the energy of the free atoms match the energy of a bound state in another channel, there will be a strong coupling which alters the effective interatomic potential and thereby can tune the scattering length through the resonance. If the two channels have different magnetic moments, the energy difference, and thus the coupling between the free atoms and the bound state in the other channel, can be controlled using an external magnetic field.

asymptotic background scattering length far away from the resonance, a_{bg} . The change of the scattering length is given by the following simple formula [5, 78]

$$a_{sc}(B) = a_{bg} \left(1 - \frac{\Delta}{B - B_0} \right) \quad (1.26)$$

which is singular at $B = B_0$. We note that Δ might be negative. ^{85}Rb has a 10 G broad Feshbach resonance at 155 G [79] whereas ^{87}Rb has several very narrow Feshbach resonances at high magnetic fields [80, 81]. The broadest one lies at $B_0 = 1007$ G and has a width of only 0.2 G which means that in order to resolve this resonance it is necessary to control a high current in the magnetic field coils with an accuracy on the order of 10 ppm which is a quite difficult task. Feshbach resonances have also been studied experimentally in ^{23}Na [82], ^6Li [83], ^{133}Cs [84], ^{40}K [85], ^{39}K [86] and ^{52}Cr [87] and heteronuclear resonances have been found in mixtures of $^{87}\text{Rb}/^{40}\text{K}$ [88, 89], $^{23}\text{Na}/^6\text{Li}$ [90] and $^{87}\text{Rb}/^{85}\text{Rb}$ [43] but not yet in Rb/Li mixtures.

Normally Feshbach resonances are applied to atoms in optical traps since a magnetic trap contributes with an inhomogeneous magnetic field. However, for very broad resonances where the inhomogeneity of the magnetic trap can be much smaller like the resonance width, as for the 10 G broad Feshbach resonance in ^{85}Rb , experiments using Feshbach resonances in combination with a magnetic trap have been reported [91]. For reference, three

Feshbach resonances referred to in this thesis are shown in Tab. 1.2.

Isotopes	$ F m_F\rangle$ states	B_0 (G)	Δ (G)	a_{bg} (a_0)	Ref.
$^{85}\text{Rb}/^{85}\text{Rb}$	$ 2 -2\rangle$ - $ 2 -2\rangle$	155.041(18)	10.71(2)	-443.(3)	[79]
$^{87}\text{Rb}/^{87}\text{Rb}$	$ 1 1\rangle$ - $ 1 1\rangle$	1007.60(3)	0.20(3)	100.5	[81]
$^{87}\text{Rb}/^{40}\text{K}$	$ 1 1\rangle$ - $ 9/2 -9/2\rangle$	546.7	-2.9 (theory)		[88]

Table 1.2: Table of the three Feshbach resonances referred to in this thesis.

It turns out that the resonance in the elastic scattering properties in the vicinity of a Feshbach resonance is accompanied by a significantly increased inelastic three-body collision rate [92] which gives rise to loss of atoms and heating. This is typically the signature used to find Feshbach resonances in experiments. When I was at JILA in the autumn 2006 we used it to locate the resonance at 547 G in a $^{87}\text{Rb}/^{40}\text{K}$ mixture. Those data are shown in Fig. 1.6.

The tunability of atomic interactions that Feshbach resonances facilitate is inevitable to modern ultracold atomic physics experiments. It can e.g. be used to associate atoms into ultracold molecules (Sec. 1.5), to study fermion pairing [93–95] and to allow for evaporative cooling and creation of a BEC of bosonic isotopes that are otherwise impossible to condense due to unfavorable collision properties (this was demonstrated with ^{85}Rb in [18] and with ^{133}Cs in [19]).

I will not go into the mathematical formalism of magnetic Feshbach resonances. It is rather complex and can be found e.g. in [5, 74, 78, 96]. Feshbach resonances (and scattering properties in general) for ultracold atoms are extremely difficult to predict theoretically because even small uncertainties in the parameters of the interatomic potentials can cause the scattering length to be completely undetermined (cf. the discussion in Sec. 1.4.1). In some cases like the $^{87}\text{Rb}/^{87}\text{Rb}$ interatomic potential, thorough measurements of scattering lengths and Feshbach resonances have finally led to accurate model potentials, but in many cases like e.g. $^{87}\text{Rb}/^7\text{Li}$ the theoretical models are not even good enough to predict the order of magnitude of the scattering length [44].

1.5 Ultracold molecules

As discussed in Sec. 1.4.1, a scattering state can evolve continuously into a molecular bound state when the scattering length is tuned from a negative to a positive value through a resonance. Two unbound atoms can therefore be associated into a molecule by sweeping the magnetic field adiabatically across a Feshbach resonance. To be more specific, we can look at

the spectrum for two confined atoms interacting via a contact interaction parameterized in terms of the scattering length. Such a spectrum is derived in Ch. 4 and shown in Fig. 5.1 on page 96. If we e.g. are on the lowest lying blue curve at $(B - B_0)/\Delta = -0.6$ in the figure and sweep the magnetic field slowly across the resonance to $(B - B_0)/\Delta = 0.6$, the unbound two-atom state evolves adiabatically into a molecular state with negative energy as illustrated by the arrow (1).

Ultracold molecules have been created using such a sweep across a Feshbach resonance both from bosonic [97–99] and fermionic [100, 101] atoms (reviews can be found in [102, 103]).

In the fermionic case, the molecules are quite long-lived (on the order of 100 ms [104]), because the inelastic collision rates for atom-molecule and molecule-molecule collisions are suppressed [105]. This is because the fermionic nature of the constituents of the molecule is not completely masked meaning that Pauli blocking has an effect even if the molecule as a whole is a boson. Therefore, the first clear evidences for the creation of a molecular Bose-Einstein condensate was reported for molecules of fermionic atoms, namely $^{40}\text{K}_2$ [100] and $^6\text{Li}_2$ [101].

On the other hand boson-boson molecules in a gas of bosons and boson-fermion molecules in a gas of bosons and fermions are very short lived, typically on the order of 100 μs . We measured the lifetime of the $^{40}\text{K}/^{87}\text{Rb}$ molecules we created at JILA (see Fig. 1.7) to be about 200-400 μs (there was too large shot-to-shot noise in the number of atoms to get a more precise estimate). This was measured by sweeping across the resonance to create molecules, holding for a variable amount of time and then sweeping back to recover the surviving atoms. Atoms from molecules which have undergone unelastic atom-molecule collisions will not be recovered.

In Ch. 5 we will investigate another approach to molecule association, namely a resonant transfer to the molecular state by small oscillations around a fixed magnetic field on the positive scattering length side of the resonance.

1.5.1 Feshbach molecules in optical lattices

The limited lifetime of boson-boson and boson-fermion Feshbach molecules is due to inelastic atom-molecule and molecule-molecule collisions. Such collisions can be strongly suppressed by putting the two atoms into an optical lattice well. If the sample is in the Mott-insulating state it is possible to prepare a sample where a large fraction of the lattice sites contain exactly two atoms [106]. The atom pairs in the lattice wells can then be efficiently associated into molecules using a Feshbach resonance. In this way $^{87}\text{Rb}_2$ molecules with a lifetime of up to 700 ms have been produced by Thalhammer et al. [107] using a sweep across the Feshbach resonance listed in Tab. 1.2. Also, heteronuclear ^{87}Rb - ^{40}K molecules with a lifetime of up to 120

ms produced using a resonant radio-frequency (RF) transfer from another hyperfine state in the vicinity of the heteronuclear Feshbach resonance in Tab. 1.2 have been reported by Ospelkaus et al. [108].

Another significant advantage of producing the molecules in an optical lattice is that two atoms in a deep optical lattice well is obviously a much simpler system than several thousands of atoms in an optical dipole trap because many-body phenomena can be neglected. As illustrated in Ch. 5 this fact makes it possible to impose a high degree of control on the dynamics and in principle completely undamped coherent processes can be driven.

It lies in the very nature of a Feshbach resonance that the molecules produced are very loosely bound (i.e. they have a high vibrational excitation). This is also the reason why they are so sensitive to atom-molecule and molecule-molecule collisions and it also means that heteronuclear molecules need to be brought down to a low vibrational state in order to gain a permanent dipole moment. Therefore one of the most interesting long-term perspectives within the ultracold molecule business is to de-excite Feshbach molecules in optical lattice wells into the ground state in a controlled way, e.g. using a series of optical Raman transitions [109]. Direct production of molecules in a low vibrational state using photoassociation avoiding the use of a Feshbach resonance altogether has also been proposed [110]. In any case a precise knowledge of the molecular level structure as well as good laser stabilization is required.

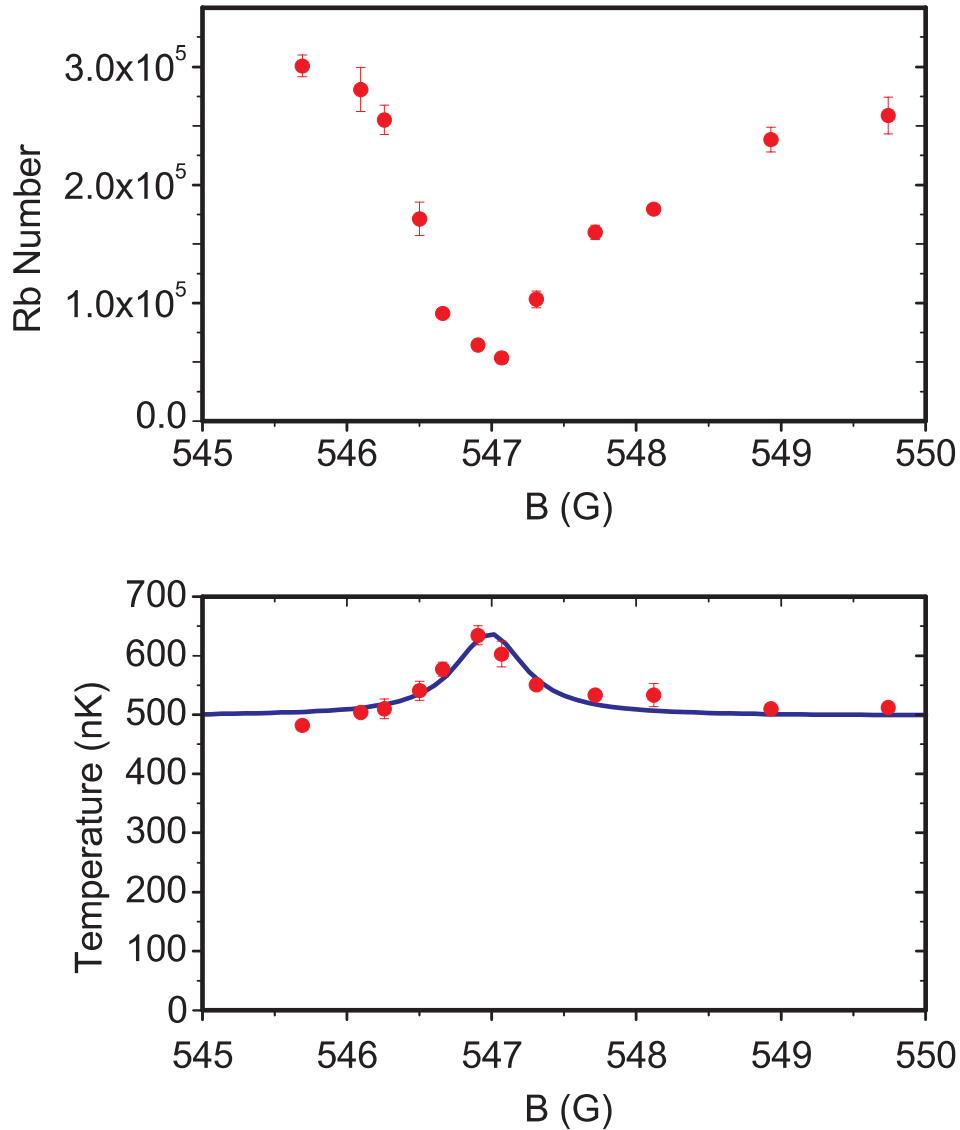


Figure 1.6: An experimental loss feature used to locate the heteronuclear Feshbach resonance at 547 G in a $^{87}\text{Rb}/^{40}\text{K}$ mixture in a far-off-resonance optical dipole trap. From a position sufficiently far away from the resonance, the magnetic field was ramped to the value in the plot and hold there for 10 ms. The upper and lower figures show the number, respectively the temperature, of the ^{87}Rb atoms in the sample. The Feshbach resonance gives rise to some heating and a significant loss of atoms. The blue line in the temperature plot is the best Lorentzian fit to the data points. The Lorentzian has its maximum at $B_0 = 547.0(3)$ G, a FWHM (full width at half maximum) of $0.59(10)$ G and a height of $0.14(2)$ μK (the uncertainties do not take calibration errors of the magnetic field into account). The magnetic field was calibrated using microwave spectroscopy. The data was obtained at JILA in collaboration with Michele Olsen, Tyler Cumby, and Deborah Jin.

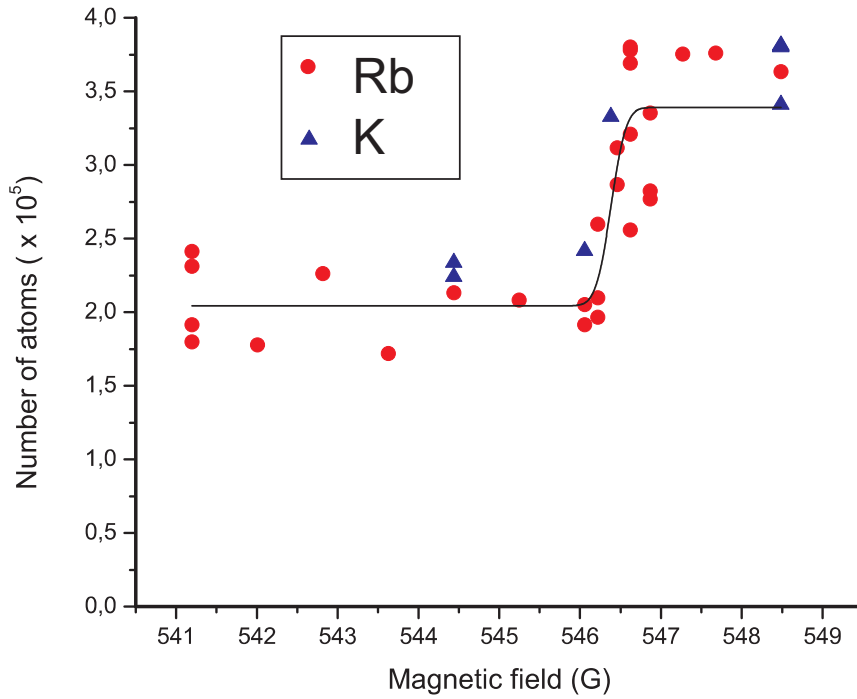


Figure 1.7: Creation of KRb molecules from Rb and K atoms in a far-off-resonance optical dipole trap. The magnetic field is swept in the direction from negative (high magnetic field) to positive (low magnetic field) scattering length at the heteronuclear Feshbach resonance at 547 G (see Tab. 1.2) and the plot shows the number of Rb (\bullet), respectively K (\blacktriangle) atoms as a function of the final magnetic field value of the sweep. Heteronuclear molecules are created if the resonance is crossed in this direction. Therefore the number of remaining atoms drops abruptly when the resonance is crossed compared to when it is not. The solid, black line is a fit of the Rb number to an error function: $N = A \operatorname{erf}((B - B_0)/(\sqrt{2} W)) + A_0$ where $A = 6.7 \times 10^4$, $A_0 = 2.7 \times 10^5$, $B_0 = 546.4$ G, and $W = 0.13(7)$ G. The data was obtained at JILA in collaboration with Michele Olsen, Tyler Cumby, and Deborah Jin.

Chapter 2

Building up a quantum gas experiment

2.1 Overview of the experimental setup

A simplified drawing of our vacuum chamber setup is shown in Fig. 2.1. The chamber consists of two parts separated by a differential pumping hole: A “high pressure” part ($P \sim 2 \times 10^{-10}$ torr) to the right in the figure where we cool and trap ^{87}Rb atoms in a cylindrical glass cell and a “low pressure” part ($P < 10^{-11}$ torr) to the left in the figure where we can produce a BEC. The differential pumping hole has an inner diameter of 4 mm which is large enough that a cloud of cold atoms can pass through it with an acceptable loss of atoms ($\sim 50\%$) but small enough that the pressure difference between the two parts can be maintained.

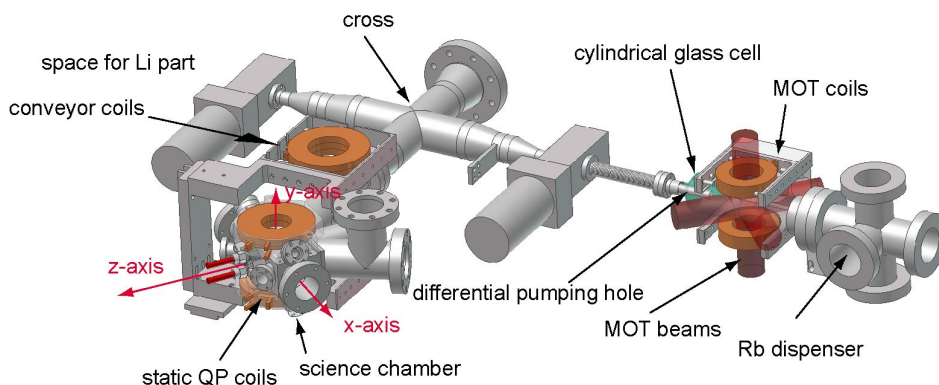


Figure 2.1: Simplified drawing of our vacuum chamber setup.

Each part is continuously pumped with 75 L/s ion pumps (Varian Star-cell 75). In the “low pressure” part of the chamber we also have two Ti-

sublimation pumps. After we had assembled the chamber it was pumped down to a pressure of about 10^{-8} torr with turbo pumps whereafter the ion pumps were turned on and the chamber was baked for two weeks at a temperature of up to 190 °C.

In the cylindrical glass cell in the “low pressure” part, the ^{87}Rb atoms are released from a commercial dispenser and cooled down from room temperature to about 100 μK in a magneto-optical trap (MOT) like in [25]. This is still well above the BEC transition temperature, but an important step on the way towards a BEC. I return to the principle of the MOT and our laser system in Sec. 2.2. After the MOT phase, the cooling laser light is turned off and the atoms are trapped in the magnetic field from the “MOT coils”. The coils (and with them the atomic cloud) are moved to the cross (see Fig. 2.1) with the help of a commercial motorized translation stage with good position and velocity control. At the cross, the atoms can be transferred to another set of moving coils which can move them the final way to the science chamber. The principles of magnetic trapping and moving of atoms are introduced in Sec. 2.4. In the science chamber, the cloud of cold atoms can be transferred to a different kind of magnetic trap (see Sec. 2.4.4) and cooled further down by means of evaporative cooling (Sec. 2.5).

The reason why the MOT and the BEC must be in two different parts of the chamber is that to cool and trap Rb atoms in the MOT, a relative high partial pressure of Rb is needed. On the other hand, the production of a BEC and the mixing process described in Ch. 3 are time consuming processes that require a much lower pressure. Otherwise collisions with room temperature background atoms will destroy the cloud of ultracold atoms during a few seconds. We have measured the vacuum lifetime of trapped Rb atoms to be about 2 min. in the “low pressure” part of the chamber.

Everything is controlled from a computer with a Delphi-based experimental control system written and maintained by Henrik. 48 digital outputs can be controlled with 1 μs time resolution and 32 analog outputs (created by 16 bit digital-to-analog conversion of a digital signal) can be controlled with down to 50 μs time resolution.

2.2 Cooling atoms

2.2.1 The Rubidium atom

An energy level diagram for the 5s and 5p states of ^{87}Rb with fine and hyperfine structure is shown in Fig. 2.2 (a detailed compilation of the spectroscopic details for the ^{87}Rb D-lines can be found in [111]). Since 28 % of naturally occurring Rb is ^{87}Rb (the rest is ^{85}Rb) one can use natural Rubidium as a source. We do laser cooling on the dipole-allowed D2-

transition ($5S_{1/2} \rightarrow 5P_{3/2}$). The thermal energies at $100 \mu\text{K}$ is on the order

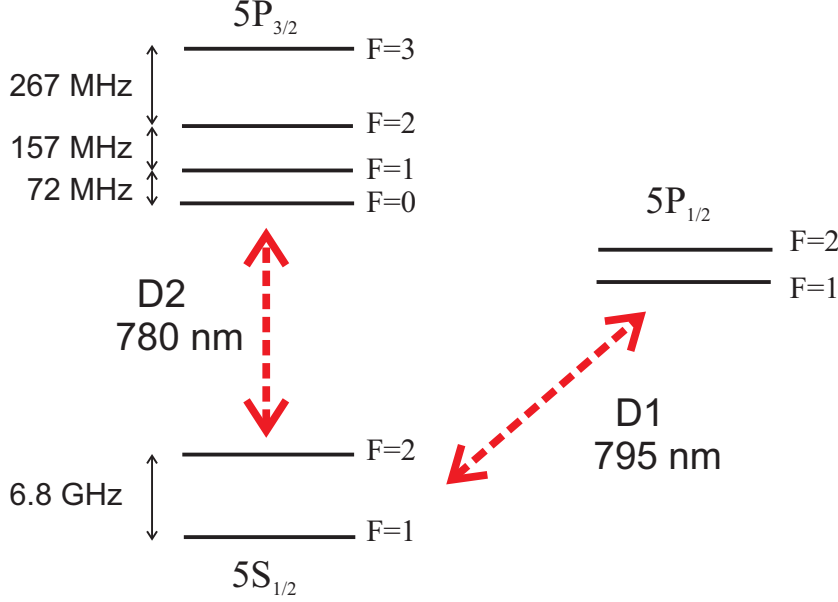


Figure 2.2: Hyperfine levels in ^{87}Rb (not to scale). Notice that the hyperfine splitting of the electronic ground state is much larger than that of the electronically excited state.

of $k_{\text{B}}T \sim 9 \times 10^{-9} \text{ eV} \sim h \times 2 \text{ MHz}$ and the hyperfine levels are clearly resolved optically since the Doppler shift at this low temperature is

$$\nu' - \nu = \frac{v}{c}\nu = \frac{v}{\lambda} \sim 0.2 \text{ MHz} \quad (2.1)$$

here taking v to be the thermal mean velocity: $v = \sqrt{8kT/(\pi m)} = 16 \text{ cm/s}$ [6]. This is an order of magnitude smaller than the natural linewidth which is 6 MHz for the ground state levels. The linewidth should be compared to the bandwidth of our laser which we have measured to be less than 1 MHz (FWHM) when it is locked.

2.2.2 Laser Cooling and the MOT

Laser cooling relies on the Doppler effect: If a stationary light source emits at a specific frequency, then the frequency in the rest frame of an atom moving *towards* the light source is higher. This means that if the light source is red detuned (has a frequency slightly lower than an atomic transition frequency) then atoms moving towards the light source will have an increased probability for absorbing a photon thus getting a momentum kick in the opposite direction slowing it down. From an energy point of view, the atoms

are forced to emit radiation with a slightly higher frequency than the frequency of the light used to excite them. In this way energy is pumped out of the system. The basic principles of laser cooling can be found in [112].

In the MOT this idea is further refined by introducing a spatial variation of the atomic transition frequency with the help of a magnetic quadrupole field (which contains a zero-point). This makes it possible not only to cool down the atoms (trapping in momentum space), but also to trap them spatially at the same time through a damping force that is given by [112–116]

$$\mathbf{F} = -k\mathbf{v} - \kappa\mathbf{r}. \quad (2.2)$$

where \mathbf{v} is the atomic velocity and \mathbf{r} is the position with respect to the center of the trap. The principle of the MOT is most easily understood in a simplified case in 1D (see Fig. 2.3).

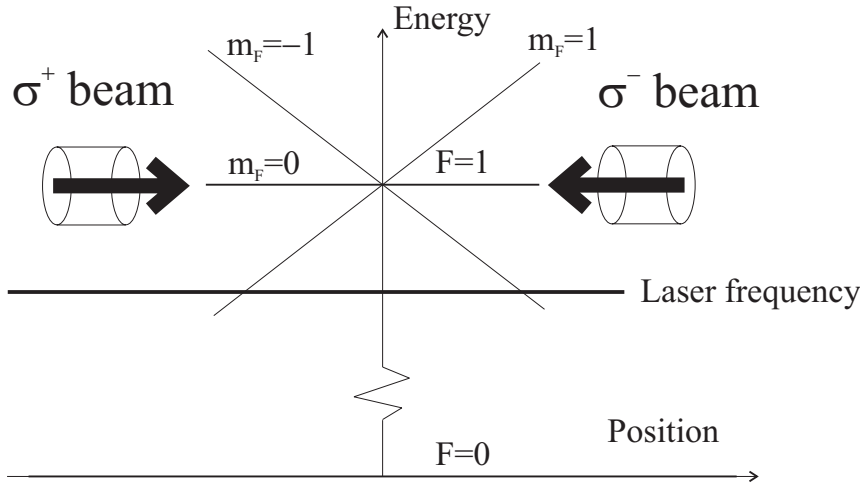


Figure 2.3: Principle of the MOT in a simplified situation where the cooling transition is from an $F=0$ ground state to an $F=1$ excited state (similar to Fig. 11.4 in [112]). Because of the varying magnetic field, the degeneracy in m_F is lifted due to the Zeeman effect. σ^+ means that the light is circularly polarized such that it drives only $\Delta m = +1$ transitions. Similarly σ^- drives $\Delta m = -1$ transitions. For atoms to the left, the energy of the $m_F = 1$ excited state is closest to the laser frequency, so here the ground state atoms scatter primarily σ^+ -light coming from the left side meaning that the atoms are pushed towards the center. Similarly the atoms to the right preferentially scatter the σ^- light and are pushed towards the center, too. Although it is not obvious from this simplified picture, the principle works well for cooling and trapping room-temperature ^{87}Rb -atoms in 3D using the $F=2 \rightarrow F'=3$ transition and it is surprisingly robust against misalignments.

To obtain cooling in all 6 spatial directions we use 3 mutually orthogonal pairs of counter-propagating laser beams. The total available power is 150

mW and the beam waists are 20 mm. We use the $F=2$ to $F'=3$ transition for cooling, because this is a cycling transition: Because of the total angular momentum selection rules for dipole transitions, atoms in the $F'=3$ state can only decay back to the $F=2$ state meaning that the system is effectively a 2-level one. The laser frequency is 3.5 times the natural linewidth (3.5×6 MHz) below resonance.

However, atoms in the $F=1$ ground state do not see the laser light because of the large hyperfine splitting of the ground state so additional laser light with a frequency corresponding to the $F=1$ to (in our case) $F'=2$ transition is needed, too. The laser source for this purpose is called the repump laser because it pumps atoms accidentally ending up in the $F=1$ state back to the cycling transition.

The magnetic field is provided by the same coils which we later use for the magnetic transport to the cross of the vacuum chamber (see Fig. 2.1). The current through the coils is 17 A giving a magnetic field gradient of 12 G/cm along the coil axis.

2.2.3 Compressed MOT and transfer to the magnetic trap

When we have caught sufficiently many atoms in the MOT, we need to turn off the lasers and transfer them to the magnetic trap so that they can be transported to the science chamber. During the MOT process, the magnetic field gradient is so small that it does not even support the atoms against gravity, so the current in the coils has to be ramped up to create a sufficiently deep trap (the maximum current that we can use is 400 A which gives a trap depth of $k_B \times 21$ mK if the atomic magnetic moment is μ_B).

However, the MOT cloud is relatively big (~ 0.5 cm) so if the current is just ramped up right away, the atoms that are most far away from the field minimum get a serious increase in potential energy which causes heating when this is transformed into kinetic energy. Therefore the MOT cloud is compressed in the final stage of the MOT process. This compression is achieved by increasing the detuning of the cooling lasers to give less light scattering (the frequency is put about 6.5 natural linewidths below resonance by changing the laser current slightly) and at the same time lowering the repump power [25]. Of course this situation should only be maintained for a relatively short time (~ 10 ms), because this compressed MOT (CMOT) is inefficient from a cooling and trapping point of view.

2.2.4 Optical pumping

For ^{87}Rb the $|F=1, m_F=-1\rangle$, $|F=2, m_F=2\rangle$ and $|F=2, m_F=1\rangle$ sub-states can be trapped (see Sec. 2.4), but atoms in other states are lost when the magnetic trap is turned on. If we imagine that the repump laser is turned off slightly before the cooling laser, all the atoms will end up in

the $F=1$ ground state (it becomes a dark state). About $1/3$ of these atoms are in the $m_F=-1$ state, so when the cooling laser is turned off and the current is ramped up, about $1/3$ of the atoms are expected to be trapped. Experimentally we trap about 40 %.

However, when we make a BEC, we use atoms in the $|F = 2, m_F = 2\rangle$ substate. We can actively pump the atoms into this substate by applying a homogeneous magnetic bias field of ~ 1 G (to make sure that the atoms stay in a specific magnetic substate) while turning on σ^+ light resonant with the $F=2 \rightarrow F'=2$ transition (see Fig. 2.4).

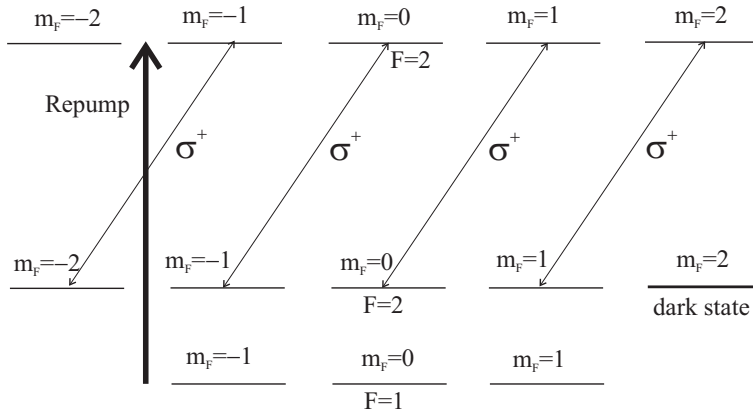


Figure 2.4: Optical pumping into the $F=2, m_F=2$ substate. Spontaneous decay can happen to both the $F=1$ and $F=2$ ground states obeying the selection rules $\Delta m=0$ or ± 1 (not shown). A small Zeeman shift (~ 1 MHz) is present due to the bias field.

The magnetic bias field comes from two extra coils that are placed outside the quadrupole coils. The coils have the following parameters:

$$25 \text{ windings (each)} \quad L=190 \mu\text{H (in total)} \quad R=0.5 \Omega \quad (2.3)$$

The natural time constant for turning on a current in the coils is $L/R=0.4$ ms which is not fast enough compared to the desired optical pumping time ($250 \mu\text{s}$). This problem is fixed by draining current from a capacitor at a high voltage (90 V) and controlling the current with a servo circuit.

A typical timing sequence of the MOT to magnetic trap processes is shown in Tab. 2.1.

2.3 The diode laser system

The present laser system is used for 3 purposes:

	MOT	CMOT	Opt. pumping	Magnetic catch
duration	~ 10 s	5 ms	250 μ s	1 ms
cooling power	150 mW	150 mW	0	0
repump power	4 mW	10 μ W	in pump beam	0
cooling detuning	-3.5 Γ	-6.5 Γ	0	0
current in coils	17 A	17 A	0	0 \rightarrow 150 A

Table 2.1: Typical (simplified) timing sequence from MOT to magnetic catch. If the optical pumping process is included, one ends up with almost all atoms in the $|F = 2 m_F = 2\rangle$ state. If it is omitted, the final result after magnetic catch is atoms in the $|F = 1 m_F = -1\rangle$ state. “Cooling detuning” is the detuning of the cooling laser light from the $|F = 2 m_F = 2\rangle$ to $|F' = 3 m'_F = 3\rangle$ transition and $\Gamma=6$ MHz is the natural linewidth.

- Laser cooling
- Optical pumping
- Absorption imaging

2.3.1 The Diode Lasers

Diode lasers are very well suited for manipulating atoms at a wavelength of 780 nm [117–119]. The main advantages of using diode lasers are probably their stability (once they are set up they need very little tuning in day-to-day use) and their price (at this wavelength, the lasers can be home made with commercial laser diodes produced for CD writers). A disadvantage is that the power produced by the lasers (~ 40 mW) is not quite enough for laser cooling meaning that we have to use a semiconductor amplifier to get enough power (~ 500 mW). The semiconductor amplifier is in principle a medium which becomes population inverted by means of a current. Laser light sent through the medium is then amplified by stimulated emission. There is a picture of one of our diode lasers in Fig. 2.5.

To work properly the lasers need to be temperature stabilized to within 1 mK. The temperature is controlled by a Peltier element lying between the main block and the laser base plate and a servo circuit that uses proportional-integral (PI) regulation:

$$\text{Peltier current} \propto A(T_{\text{actual}} - T_{\text{aimed}}) + B \int (T_{\text{actual}} - T_{\text{aimed}}) dt \quad (2.4)$$

where A and B are constants set by some resistor and capacitor values in the circuit. The laser diode current is controlled by a very stable current supply designed by the local electronics workshop.

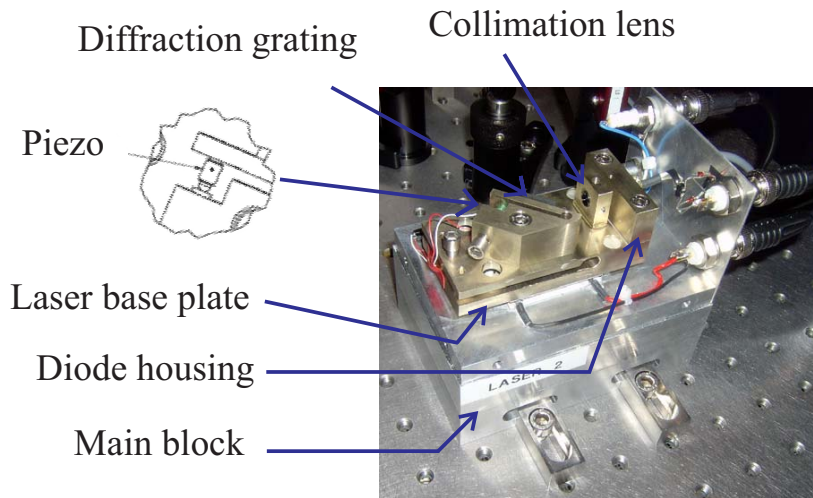


Figure 2.5: One of our home built diode lasers.

The purpose of the diffraction grating is to control the frequency of the laser. If the 1st order diffracted beam from the grating strikes directly back into the laser diode, it will stimulate the diode to lase at this frequency. So by adjusting the angle of the grating (and thus the frequency which is diffracted back into the diode) one can roughly tune the laser frequency. This is done only once when setting up the laser.

Because the grating sends some light back into the laser diode, it also extends the effective laser cavity. Therefore the piezo crystal can be used to tune the cavity and thus the frequency of a specific laser mode by a small, controllable amount. This is used all the time.

2.3.2 Locking to an atomic resonance

The frequencies of the lasers are locked with a precision of about 1 MHz using saturated absorption spectroscopy and the so-called Pound-Drever-Hall locking principle [120].

The idea of saturated absorption spectroscopy is to circumvent the Doppler broadening which, for room temperature Rb atoms, is several hundred MHz, thus smearing out the hyperfine structure of the excited state (cf. Fig. 2.2). The principle is the following: A laser beam - the pump beam - is sent through a glass cell containing Rb (at room temperature and with low background pressure). The intensity is well above the saturation intensity. The absorption is now measured with another beam which is counter-propagating and has a lower intensity but the same frequency - the probe beam (see Fig. 2.6).

If the frequency is such that many atoms are resonant with both beams, the absorption of the probe beam will *decrease*, because the pump beam has excited half of the atoms. This can be seen as a small top in the absorption spectrum (see the blue absorption curve in Fig. 2.6).

Now, since the beams are counter-propagating, the Doppler shift experienced by a specific atom with respect to the two beams is equal in magnitude and of opposite sign. So the atom can only be resonant with both beams if it

- either has zero velocity along the beam axis such that there is no Doppler shift. In this case the frequency has to match that of a specific hyperfine transition.
- or a velocity giving a Doppler shift which is half the difference between the transition frequency from a common ground level to two different excited, hyperfine levels. In that case the light frequency is the average of the frequencies in the two hyperfine transitions. Such absorption peaks are called crossover peaks.

By modulating the laser diode current with a small radio-frequency (RF) signal and using some sophisticated electronics, it is possible to effectively probe the dispersion instead of the absorption and in this way obtain a spectrum with zero-crossings at the resonances (see Fig. 2.6). This signal is suitable for locking the laser to a specific resonance by connecting the piezo crystal and the laser diode current supply to a servo circuit which tends to stabilize the locking signal at zero.

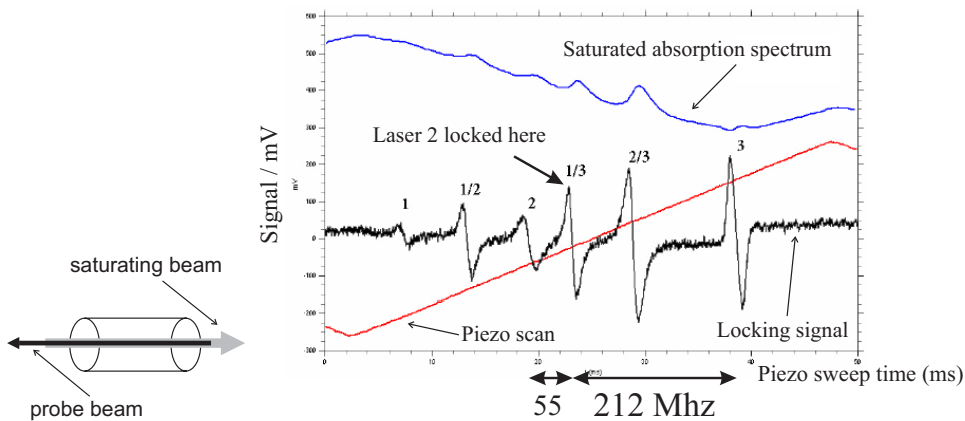


Figure 2.6: Saturated absorption spectroscopy and the locking signal. The laser frequency is scanned with the piezo crystal. 1/3 means the crossover peak corresponding to the $F=2 \rightarrow F'=1$ and $F=2 \rightarrow F'=3$ transitions.

2.3.3 Optical Table Setup

The laser system is very roughly sketched in Fig. 2.7, and I have also made a detailed drawing of our optical table setup (Appendix A). Some of the optics was already set up when I made the drawing, but for the rest, it was an indispensable help in finding a sensible layout before actually setting up the components. A detailed description of the setup would not make sense here, but I shall give an overview.

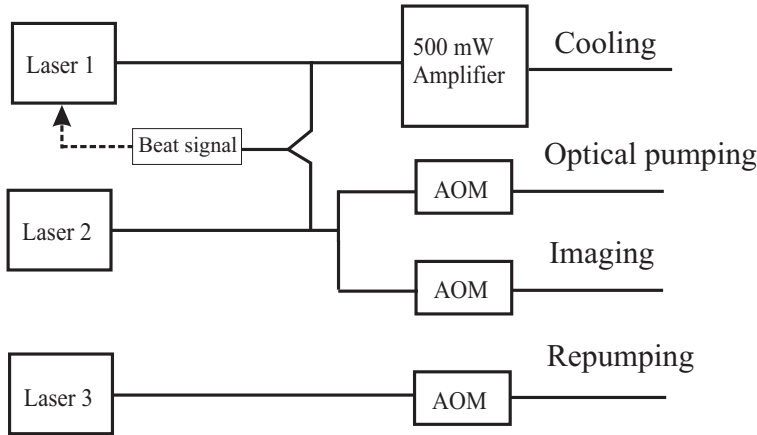


Figure 2.7: Rough sketch of the laser system.

There are 3 lasers. A portion of the light from each laser is sent into a saturated absorption spectroscopy setup. Laser 1 on the sketch provides the cooling light in the MOT beams. The beam is sent through the amplifier (TA on the detailed drawing). Some of the light from the lasers 1 and 2 is mixed and the co-propagating beam is sent into a photodetector with 300 MHz bandwidth. If the frequency of the 2 lasers differs slightly by an amount $\Delta\nu$, the light intensity is beating with this frequency. The beat signal is amplified in the photodetector and the resulting signal is used to control the frequency of Laser 1 relative to that of Laser 2 by electronic means [121]. Laser 2 is locked to the $F=2 \rightarrow F=1/3$ crossover resonance.

Besides acting as a frequency reference for the cooling laser, Laser 2 is furthermore used for imaging and optical pumping and is shifted to the relevant frequencies by means of Acousto Optical Modulators (AOMs). Laser 3 supplies the repump light. The repump light is mixed with the cooling light after the amplifier and also with the imaging and optical pumping light separately. The beams can be turned on and off quickly by means of electro-mechanical shutters (precise on a ms time scale) and the AOMs (precise on a μs time scale). A photograph of the optical table taken right after I had finished most of the setup is shown in Fig. 2.8.

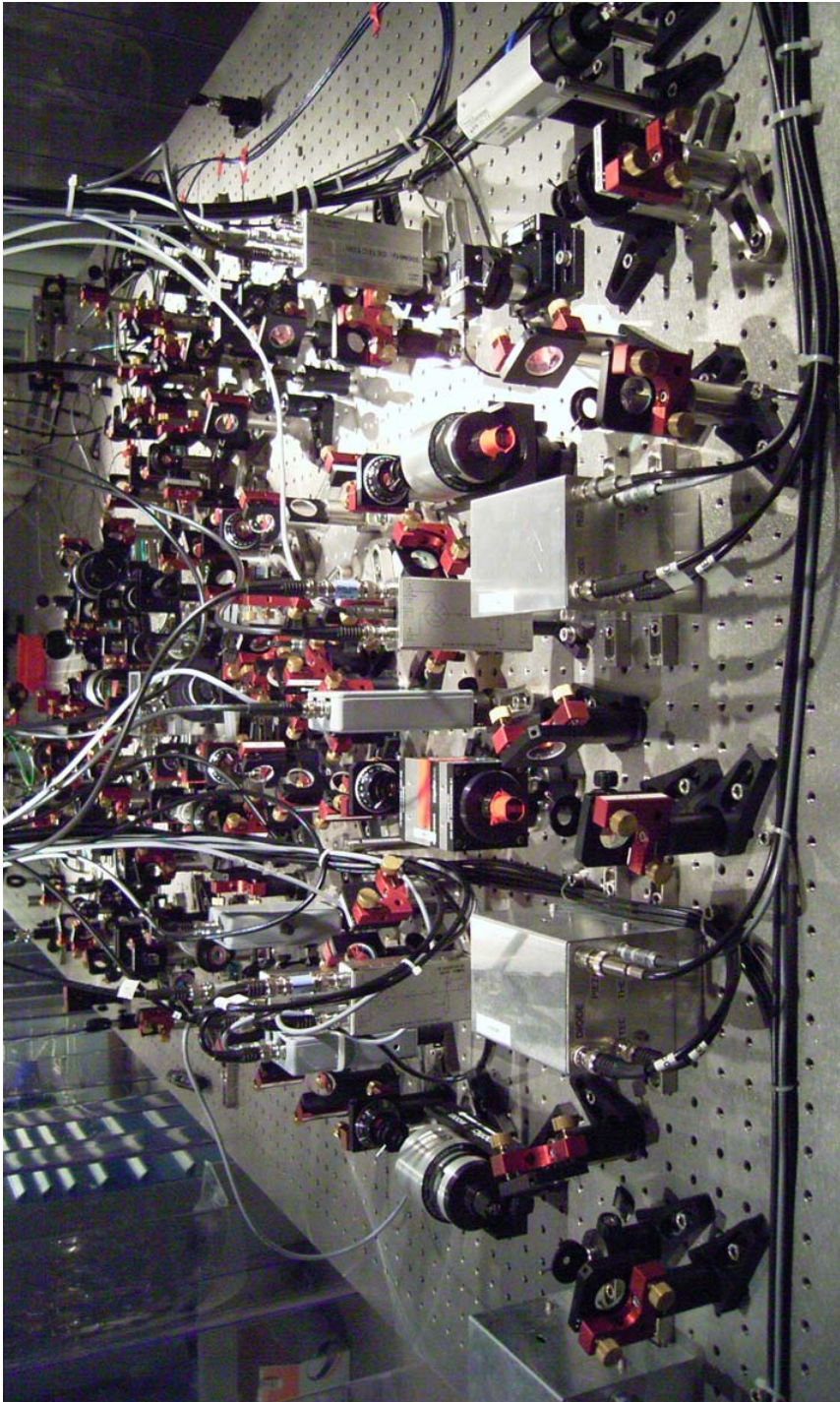


Figure 2.8: Photograph of the optical table setup with the diode lasers in front. Taken June 2005.

All the laser beams are eventually coupled into polarization maintaining, singlemode optical fibers that go to the vacuum chamber table. Besides providing a proper transportation line for the light from the laser table to the vacuum chamber table, the fibers serve to clean up the spatial beam profile, because the beam coming out of a singlemode fiber has an almost perfectly Gaussian profile. However, there is some loss in the coupling-in process (40-60% for the MOT beams due to a very ugly beam profile from the amplifier and 30-40 % for the other fibers).

The fibers that we use for the MOT beams contain a polarization maintaining fiber splitter (Canadian Instrumentation and Research) such that the power that we couple into the fiber input is equally split between two fiber outputs. The two fiber outputs are then used for a counter-propagating pair of beams in the MOT. One of the advantages is that ideally the two outputs remain balanced even if the total power coupled into the fiber is drifting slightly. Another advantage is that it is only necessary to couple light into 3 optical fibers which also saves some optics (unfortunately for one of the fiber splitters, the power share between the two outputs is fluctuating on a few % level).

It is of significant importance that the polarization of the beam coming out of the fiber is stable: Both because the polarization of the MOT beams needs to be stable and because polarization fluctuations turn into intensity fluctuations when the beam is sent through a polarizing beam splitter cube (PBS). In order to achieve a stable polarization, the polarization of the beam coupled into the fiber needs to be strictly linear and aligned with the polarization maintaining axis of the fiber. In particular I learnt that a reflected beam from our PBSs is slightly elliptically polarized and therefore needs to be transmitted through another PBS to obtain a clean polarization. For the fibers with splitters (those used for the MOT beams) the polarization fluctuations are below 1 % of the intensity (typically 0.4 %). For the other fibers 2-3 % is more typical.

2.4 Trapping and moving atoms

2.4.1 Principles of magnetic trapping

Magnetic trapping of atoms relies on the Zeeman splitting of the hyperfine ground states: $H_{\text{Zeeman}} = -\boldsymbol{\mu} \cdot \mathbf{B}$ where the magnetic moment $\boldsymbol{\mu}$ has contributions from both electronic angular momentum ($\mathbf{J} = \mathbf{L} + \mathbf{S}$) and nuclear spin (\mathbf{I}). If the Zeeman interaction ($\sim \mu_B B$) is comparable to the hyperfine interaction in magnitude, H_{Zeeman} must be diagonalized together with the hyperfine ($\mathbf{J} \cdot \mathbf{I}$) interaction. In the case $L=0$ which is relevant for the ground state of alkali metal atoms, the result of this is given analytically

(the Breit-Rabi formula) [26, 111, 122]:

$$E = \text{constant} + (-1)^F \frac{\Delta E_{\text{HF}}}{2} \sqrt{1 + \frac{4m_F}{2I+1}x + x^2} \quad (2.5)$$

where ΔE_{HF} is the hyperfine splitting of the unperturbed ground state and x is a scaled magnetic field:

$$x = \frac{(g_I + g_s)\mu_B B}{\Delta E_{\text{HF}}} \quad (2.6)$$

Here $g_s = 2.00$ is the g-factor of the electron and $g_I = 1 \times 10^{-3}$ for ^{87}Rb is the nuclear g-factor (with respect to μ_B). It is assumed that the quantization axis points in the direction of the magnetic field. The result of the Breit-Rabi formula is plotted for ^{87}Rb in Fig. 2.9.

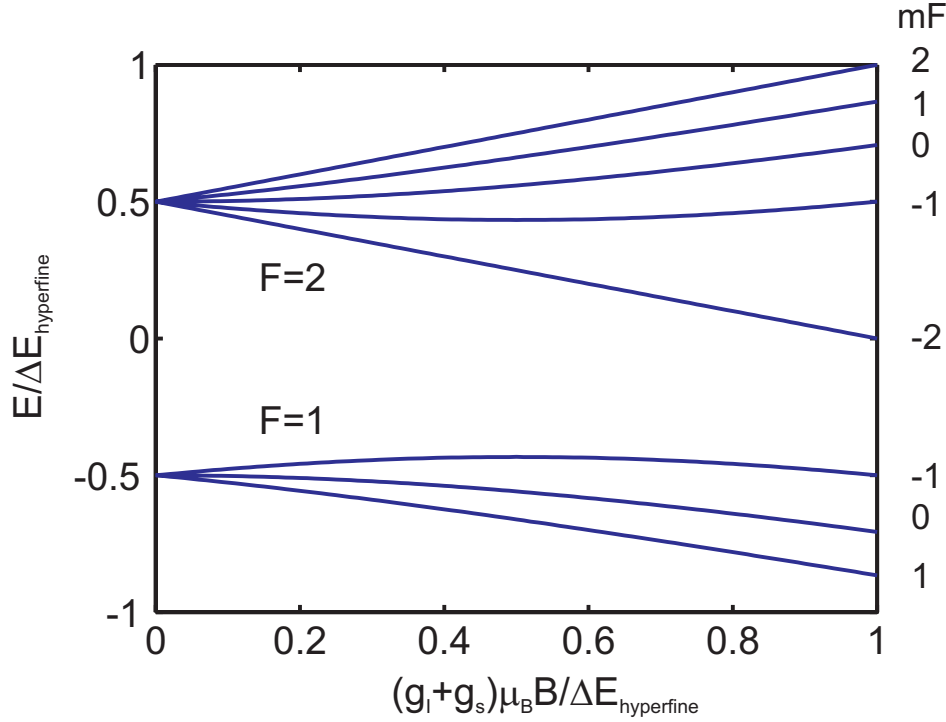


Figure 2.9: Zeeman shift of the ground state term in ^{87}Rb . The zero of the energy is chosen midway between the $F = 1$ and $F = 2$ states at zero magnetic field and $\Delta E_{\text{hyperfine}}$ denotes the hyperfine energy splitting.

However, even for the strongest fields that our ^{87}Rb atoms experience during magnetic transport (~ 100 G), we have

$$x \approx \frac{2\mu_B B}{\Delta E_{\text{HF}}} = 0.04 \quad (2.7)$$

so to a good approximation the Zeeman interaction is just a perturbation of the hyperfine states. If we furthermore neglect the small contribution from the interaction with the nuclear spin, we can calculate the linear Zeeman shift either from (2.5) or by calculating the 1st order perturbation in the hyperfine states:

$$\Delta E_{\text{Zeeman}} = g_s \frac{\mu_B}{\hbar} \mathbf{B} \cdot \langle F m_F | \mathbf{S} | F m_F \rangle = g_F m_F \mu_B B \quad (2.8)$$

where $g_F = (-1)^F \frac{1}{2I+1} g_s$. For ^{87}Rb , $I = 3/2$.

Since it is impossible to make a stationary magnetic field configuration with a local maximum [123], only states that have a lower energy at lower fields can be magnetically trapped (that is, states with $g_F m_F > 0$ if we take only the first order Zeeman shift into account). For ^{87}Rb , the trapable states are listed in Tab. 2.2.

F	m_F	g_F
1	-1	-1/2
2	1	1/2
2	2	1/2

Table 2.2: The trapable hyperfine states of the ground term in ^{87}Rb .

2.4.2 The quadrupole trap

The magnetic trap that we use for transport and mixing is a quadrupole trap ideally consisting of two circular current loops with the same radius, axis of symmetry and with currents of equal magnitude and opposite direction (see Fig. 2.10). The actual coils that we use are made of $4.25 \times 4.25 \text{ mm}^2$ square, copper tubing with cooling water flowing in the middle. The coils are cast in epoxy for stability and each coil has outer dimensions of about $10 \times 10 \times 2 \text{ cm}^3$ (see Fig. 2.10). More details about the coils are given in Chap. 3.

The $B = 0$ point midway between the coils provides the magnetic field minimum. Around the zero-point, the magnetic field increases linearly in all directions. The gradient in the z -direction is twice the gradient in the radial direction. This is clear from the Maxwell equation $\nabla \cdot \mathbf{B} = 0$ and cylindrical symmetry:

$$0 = \nabla \cdot \mathbf{B} = \frac{\partial B}{\partial x} + \frac{\partial B}{\partial y} + \frac{\partial B}{\partial z} = 2 \frac{\partial B}{\partial x} + \frac{\partial B}{\partial z} \Rightarrow \frac{\partial B}{\partial z} = -2 \frac{\partial B}{\partial x}. \quad (2.9)$$

The exact magnetic field in the ideal quadrupole trap is given by elliptic integrals [124]. Near the zero of the magnetic field, the magnitude (for our

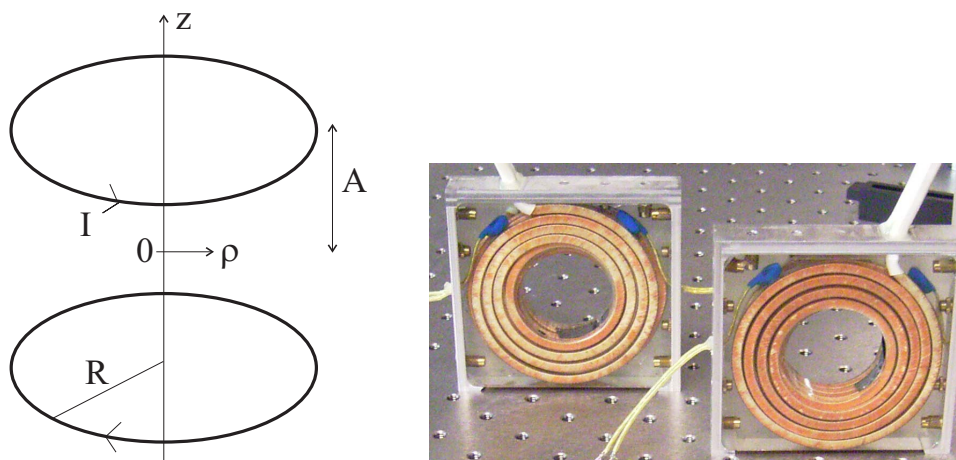


Figure 2.10: Idealized quadrupole coils (left) and the real ones that we use in the laboratory (right). The size of the squares is about $10 \text{ cm} \times 10 \text{ cm}$.

coils up to about 1 cm away which is much more than the size of the trapped atomic cloud) can be approximated by [112]

$$B(\rho, z) \approx \left. \frac{\partial B}{\partial \rho} \right|_{\mathbf{r}=\mathbf{0}} \times \sqrt{\rho^2 + 4z^2} \quad (2.10)$$

This formula shows that the potential energy isosurfaces near the minimum are ellipsoids. The detailed thermodynamic properties of the quadrupole trap are derived in Sec. 3.4.1.

The particles in a magnetic trap move around and thus feel a changing magnetic field. The trapable states are defined with respect to a quantization axis pointing in the direction of the local magnetic field vector, so the trapped atoms effectively move in a potential depending only on the *magnitude* of the magnetic field

$$U(\mathbf{r}) = g_F m_F \mu_B B(\mathbf{r}). \quad (2.11)$$

For an atom to remain trapped, it must stay in the trapable state with respect to the local magnetic field vector all the time. This is only fulfilled if the change of the instantaneous magnetic field vector felt by an atom is not too fast compared to the Larmor spin precession frequency $\omega_{\text{Larmor}} = g_F m_F \mu_B B / \hbar$ [4] (in a semi-classical picture the spin precession axis has to adiabatically follow the magnetic field vector). Otherwise the atom undergoes transitions to other (possibly untrapped) spin states with respect to the instantaneous magnetic field, so-called Majorana spin-flips.

Since ω_{Larmor} scales proportional to B , Majorana spin flips is only a problem in regions where the magnitude of the magnetic field is close to 0,

in practice that means for $B \lesssim 1$ G [4, 26]. For a quadrupole trap which has a zero in the middle, the loss rate due to Majorana spin-flips is related to the amount of time each atom spends in the region of very low magnetic field so cold clouds, which are dense and tightly confined around the point of zero field, have a larger loss rate than hot clouds. A theoretical estimate of the loss rate carried out in [125] leads to the following simple, approximate formula for the lifetime of an atomic cloud trapped in a quadrupole trap and subject to Majorana spin-flips

$$\tau \approx \frac{m}{\hbar} l^2 = 1.4 \times 10^3 \text{ s} \times \left(\frac{l}{\text{mm}} \right)^2 \quad (2.12)$$

where l is a measure of the extension of the cloud. The clouds used in the mixing process in Chap. 3 have a temperature of about $200 \mu\text{K}$ at a radial trap gradient of 100 G/cm giving an axial RMS extension of about 0.6 mm (see formula 3.15 derived in Sec. 3.4.1). This corresponds to a Majorana spin-flip lifetime of 500 s , but the cloud does not have to be much colder than that, until Majorana losses must be considered. Therefore a trap where the bottom has a nonzero magnetic field is needed to create a BEC (Sec. 2.4.4).

2.4.3 Moving schemes

Once the atoms are trapped in a quadrupole trap, they can be moved by moving the magnetic field minimum. One way to do that is to have a chain of overlapping, stationary coils. By running suitable currents through 3 coil pairs at a time, it is possible to move the potential minimum in such a way that the aspect ratio of the atomic cloud remains unchanged such that heating can be avoided if the movement is slow enough. This was demonstrated by Greiner et al. in 2001 [126].

The other approach, which we use, is to run a stationary current through a single pair of coils which is moved mechanically. This scheme was introduced by Lewandowski et al. in 2003 [25] and has the clear advantage that we only need one pair of coils and that there is only one current to control. Especially when one has to move the atoms a long distance, this saves a lot of cost and effort. Initially we considered using the other approach because we were afraid that vibrations caused by movement of the coils would heat up the atoms, but it turns out not to be a problem. We use a commercial computer controlled conveyor belt to move the trap coils (Parker 402XR series).

2.4.4 The QUIC trap

The quadrupole trap is easy to construct and gives a tight confinement, but the zero of the magnetic field in the middle of the trap eventually becomes

a problem when the cloud is cooled below the temperature where Majorana spin-flips are important. The solution is to use a magnetic trap which has a bias field (i.e. the trap bottom has a nonzero magnetic field).

We use the so-called QUadrupole Ioffe Configuration (QUIC) trap invented by T. Esslinger et al. [127]. It has the advantage that it is easy to make compact since it only consists of three circular coils: A quadrupole trap created by the “static QP coils” in Fig. 2.1 with a third coil added. The disadvantage is that, since the configuration is asymmetric, the value of the bias field depends critically on the placement of the third coil. Since all the work on mixing of atomic clouds in Ch. 3 was done with quadrupole traps I will not go into details about the QUIC trap.

2.5 Forced evaporation

We use standard forced evaporative cooling to cool the atomic cloud in the science chamber further down to the BEC transition temperature [5, 25, 112, 128]. The principle is to successively remove the most energetic atoms by transferring them to an untrapped hyperfine state using a radio frequency (RF) magnetic field from some extra coils *inside* the science chamber. I have spent some time measuring the magnetic field from these coils and finding out how powerful the RF power supply for the coils should be, but I will not describe that here. The evaporative cooling is the part of the BEC creation process which takes the longest time ($\sim 1/2$ -1 min.), because it relies on the atoms having time to thermally equilibrate by elastic collisions during the evaporation process.

We use a home-made Direct Digital Synthesizer (DDS) based RF generator to create a low power RF signal whose frequency can be tuned from 10 kHz to 70 MHz and amplify it with a class A 75 W amplifier with an amplifying range from 10 kHz to 250 MHz (Amplifier Research 75A250).

2.6 Imaging atoms

The diagnostics of the ultracold Rb gas in the science chamber is done by absorption imaging: A short pulse of laser light, which is on or close to resonance with the $F = 2$ to $F' = 3$ cycling transition, is sent through the atomic cloud and an image is taken with a CCD camera and analyzed on the computer. Let us call the imaging axis the x-axis (see Fig. 2.11). For a dilute cloud of many atoms, the probability that a photon is absorbed within an infinitesimal distance dx is proportional to dx :

$$\frac{\partial I(x, y, z)}{\partial x} = -\sigma n(x, y, z) \quad (2.13)$$

where σ is the absorption cross section and $n(x, y, z)$ is the spatial density of atoms. Therefore the light intensity is exponentially damped through the

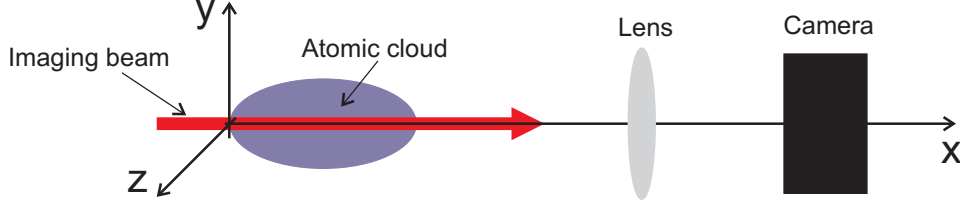


Figure 2.11: Schematic imaging setup.

cloud [4]:

$$I(x, y, z) = I_0 \exp\left(-\sigma \int_0^x n(x', y, z) dx'\right) = I_0 e^{-OD(y, z)} \quad (2.14)$$

where the optical density $OD(y, z)$ has been defined in the last equality:

$$OD(y, z) = \sigma \int_0^x n(x', y, z) dx'. \quad (2.15)$$

The total number of atoms is given by

$$N = \iiint n(x, y, z) dx dy dz = \frac{1}{\sigma} \iint OD(y, z) dy dz \quad (2.16)$$

where the last double integral can be obtained either from a Gaussian fit or from a sum of pixel values.

We take three images in each imaging sequence: An image with atoms, $RAW(y, z)$, to infer $I(y, z)$, an image taken after 1 s where all the atoms have flown away, $REF(y, z)$, to infer I_0 and a background image without any laser light, $BCKGRD(y, z)$, taken after an additional 1 s to infer the background light level. The optical density is then

$$OD(y, z) = -\ln \frac{I(y, z)}{I_0(y, z)} = -\ln \frac{RAW(y, z) - BCKGRD(y, z)}{REF(y, z) - BCKGRD(y, z)}. \quad (2.17)$$

This three-image sequence ensures that fluctuations in the laser beam and background light intensities has a minimal influence on the measured optical density. We have two different imaging systems: To image large, thermal clouds, including the clouds studied in Chap. 3, we use a camera manufactured by Point Grey Research (Scorpion 20SO). It has 1600x1200 pixels and 12 bit resolution. To image very cold, thermal clouds and BECs we use a more dedicated scientific camera (DTA CHROMA C3) which has lower noise and whose CCD chip can be cooled down to -12°C . The CCD chip of this camera has 2184x1472 pixels with 14 bit resolution. I have spent some time testing and adapting the driver of the DTA camera to our experimental control system.

To image atoms in the $F = 1$ hyperfine ground state, we first shine in a repumping beam resonant with the $F = 1$ to $F' = 2$ transition for $100 \mu\text{s}$ in order to pump all the atoms up into the $F = 2$ ground state.

Normally the magnetic trap is turned off a couple of ms before the RAW image is taken such that the atoms are in free flight. Typical images after 7 and 13 ms time-of-flight are shown in Fig. 2.12. It is important that the magnetic field (including residual fields from eddy currents) is turned off on a timescale that is much shorter than the time-of-flight. The current in the quadrupole part of the QUIC trap can be turned off during $340 \mu\text{s}$.

Collisions can be neglected during the time-of-flight since the average collision time is on the order of a second. Neglecting also gravity, the position of each atom evolves in time as

$$\mathbf{r}(t) = \mathbf{r}_0 + \mathbf{v}t \quad (2.18)$$

where \mathbf{r}_0 is the initial position and \mathbf{v} is the velocity. Since the velocity distribution is Gaussian, the spatial distribution will approach a Gaussian shape as the cloud expands. For a cloud at $200 \mu\text{K}$ the mean thermal velocity is $\langle v \rangle = 0.22 \text{ mm/ms}$ so it only takes the spatial distribution a few ms to become Gaussian even if the initial spatial distribution in the quadrupole trap is not. Therefore we can fit $OD(y, z)$ to a two-dimensional Gaussian function:

$$OD(y, z) = \frac{N\sigma}{w_y w_z \pi} e^{-(y-y_c)^2/w_y^2} e^{-(z-z_c)^2/w_z^2} + \text{offset} \quad (2.19)$$

where a constant offset is included, (y_c, z_c) is the center position of the cloud, and w_y and w_z are the vertical and horizontal widths of the cloud. Thus, the number of atoms, N , can be directly extracted from this fit.

2.6.1 Temperature measurements

In order to measure the temperature of the cloud, we assume a Gaussian initial spatial density such that the initial phase space density relative to the center of the cloud is

$$\rho(\mathbf{r}_0, \mathbf{p}) \propto \prod_{i=x,y,z} \exp\left[-\frac{p_i^2}{2mkT}\right] \exp\left[-\frac{m\omega_i^2 r_{0i}^2}{2kT}\right]. \quad (2.20)$$

where ω_i are constants with dimension inverse time. The density at time t after the magnetic trap is turned off is then given by a convolution

$$n(\mathbf{r}, t) = \iiint d^3\mathbf{r}_0 d^3\mathbf{p} \rho(\mathbf{r}_0, \mathbf{p}) \delta\left(\mathbf{r} - \mathbf{r}_0 - \frac{\mathbf{p}t}{m}\right) \quad (2.21)$$

$$\propto \prod_{i=x,y,z} \int_{-\infty}^{\infty} dp_i \exp\left[-\frac{p_i^2}{2mkT}\right] \exp\left[-\frac{1}{2kT}m\omega_i^2\left(x_i - \frac{p_it}{m}\right)^2\right] \quad (2.22)$$

$$= \prod_{i=x,y,z} \exp\left[-x_i^2/w_i(t)^2\right] \quad (2.23)$$

where the widths $w_i(t)$ are given by

$$w_i(t)^2 = w_{i0}^2 + \frac{2kT}{m}t^2, \quad w_{i0} = \frac{2kT}{m\omega_i^2}. \quad (2.24)$$

In conclusion, the widths in the y and z directions evolve according to

$$w^2 = w_0^2 + \frac{2kT}{m}t^2 \quad (2.25)$$

so a plot of w^2 as a function of the squared time-of-flight t^2 will be straight line for sufficiently long time-of-flights and the temperature can be calculated from the slope of the line. An example is shown in Fig. 2.12.

The fact that the initial distribution in the quadrupole trap is not Gaussian leads to small deviations between the actual temperature and the temperature that one finds from the method above. In order to quantify this deviation we have performed the convolution (2.21) numerically with the actual equilibrium density in the quadrupole trap (Eq. 3.13 in Sec. 3.4.1) for 7, 9, 11, and 13 ms time-of-flight, made a Gaussian fit to the resulting distribution and plotted w^2 as a function of $(2k/m)t^2$ to model what we do experimentally.

The result of such a calculation is shown in Fig. 2.13. In this figure, the expansion of a 200 μK cloud was modeled. The linear fit to the smallest (vertical) widths suggests a temperature of 203.7(9) μK (2% deviation from the actual temperature) whereas a fit to the largest (horizontal) width suggests a temperature of 219(3) μK (9% deviation from the actual temperature). For a 400 μK cloud, there is also a 2% deviation when the vertical widths are used, but a 19% deviation when the horizontal widths are used.

Experimentally we also see that the fit where the horizontal widths are used suggests a larger temperature than the fit where the vertical widths are used. This makes sense because the Gaussian velocity distribution, which is isotropic, will start to dominate the density distribution $n(\mathbf{r}, t)$ of the atoms after a shorter time-of-flight in the vertical than in the horizontal

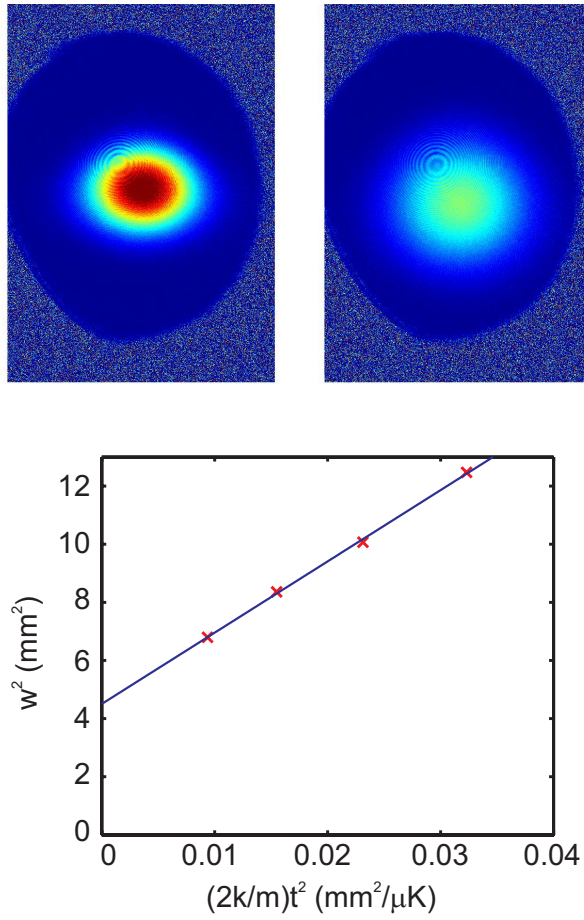


Figure 2.12: Upper figures: Images of a ^{87}Rb cloud after 7 and 13 ms time-of-flight. Lower figure: Determination of temperature using the Gaussian widths of clouds in images taken after 7, 9, 11, and 13 ms time-of-flight.

direction since the cloud has a smaller extension in the vertical direction. The theoretical simulation tells that the temperature derived from Gaussian fits after 7, 9, 11, and 13 ms time-of-flight is reliable to within 2% both for 200 μK and 400 μK clouds provided that the vertical widths are used.

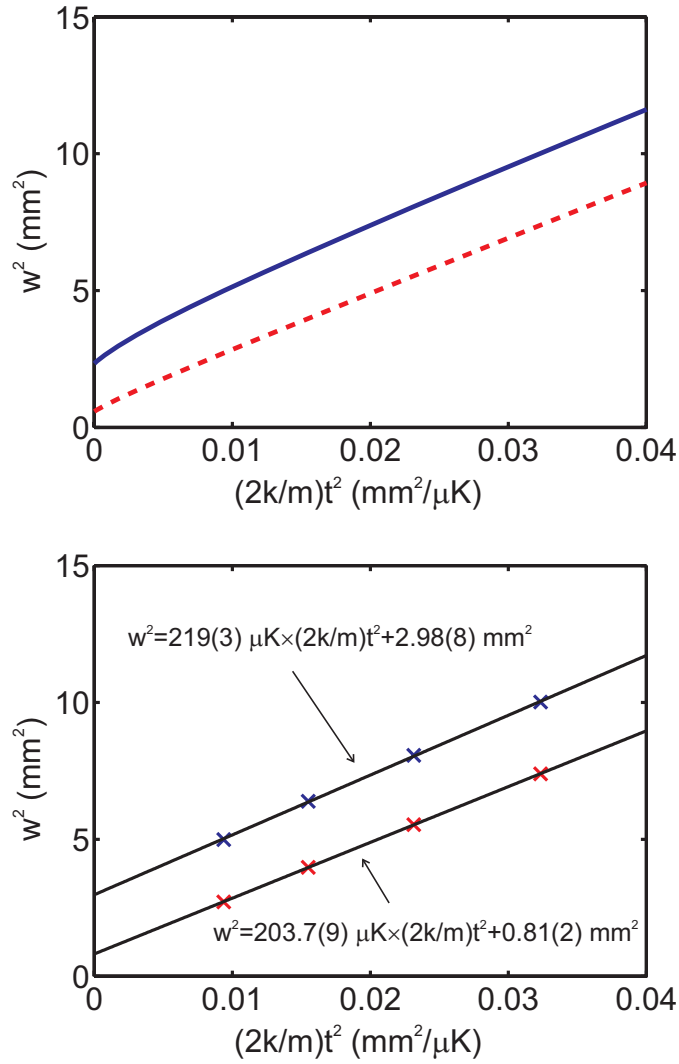


Figure 2.13: Theoretical modelling of a $T = 200 \mu\text{K}$ cloud expanding from a quadrupole trap with a radial gradient of $\partial|B|/\partial\rho = 84 \text{ G/cm}$. The upper figure shows the squared widths from a Gaussian least squares fit, w^2 , as a function of the squared time-of-flight, t^2 . After a few ms the curve becomes linear in accordance with (2.24). The lower figure shows linear fits to the points at $t = 7, 9, 11,$ and 13 ms.

2.7 Future plans

In the near future it is the plan to add a Li MOT to the system (see Fig. 2.14). Atomic clouds from the two MOTs are then to be mixed at the cross. This will give a flexible system with possibilities for studying boson-boson ($^{87}\text{Rb}/^7\text{Li}$) as well as boson-fermion ($^{87}\text{Rb}/^6\text{Li}$) mixtures.

The Li part is going to be based on a laser diode-amplifier setup similar to the one that we use for Rb (but with the important difference that more repump power is needed because the hyperfine structure of the excited state in Li is not resolved). Both the laser system and the vacuum chamber of the Li part will be built and optimized in another room such that the existing experiment is not disturbed. The existing vacuum chamber is shut off with a valve such that the two vacuum chambers can be connected without breaking the vacuum when the Li MOT is working.

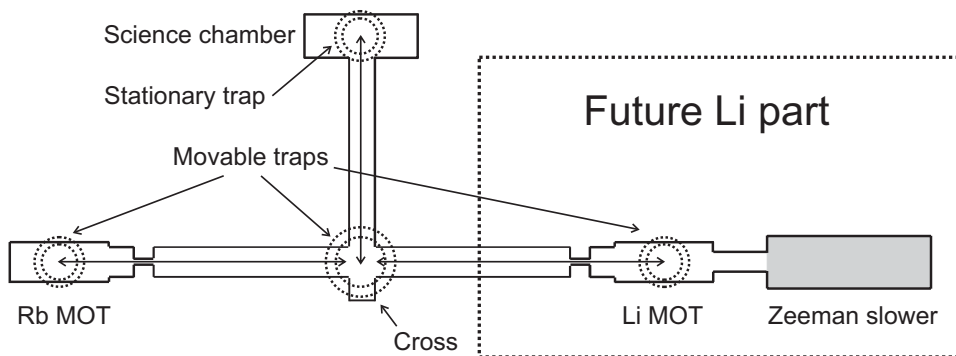


Figure 2.14: In the future it is the plan to add a setup for cooling and trapping Li. Since Li is much lighter than Rb, it needs to be pre-cooled in e.g. a Zeeman slower [112] before it can be captured in a MOT, but otherwise the Li part of the vacuum chamber is going to be similar to the Rb part. The Rb and Li atoms are going to be mixed at the cross using the method introduced in Ch. 3.

Henrik is currently finishing the setup of a three-dimensional optical lattice with a lattice wavelength of $\lambda = 920$ nm. This setup can also be used to create a one-, two- or three-dimensional optical dipole trap. In the short term perspective he is going to use the lattice to study adiabatic transfers between a dipole trap and an optical lattice. In the long term perspective it is a possibility to put a Rb-Li mixture into the lattice to e.g. study phase phenomena. Sune is currently doing theoretical and experimental studies of RF and microwave transfers that exploit the nonlinear Zeeman shift in Rb.

Chapter 3

Mixing ultracold atoms

The main results in this section are published in [1].

3.1 Purpose

In this chapter I present the experimental and theoretical studies of the process of mixing two ultracold, but still thermal, atomic clouds caught in two quadrupole traps. The studies are motivated by the fact that the Quantum Gas Laboratory in Aarhus is going to study quantum gas mixtures in the future and that we wanted to investigate an alternative method for preparing the ultracold clouds, a method that does not make use of a two-species MOT. However, the mixing process has turned out to be quite nontrivial and interesting in its own right and I have definitely learnt that the dynamics of atoms in the potential created by two merging magnetic quadrupole traps is very complicated.

The basic idea is to cool and trap the two elements in separate MOTs and then mix the two clouds afterwards. After the atoms are cooled down in the MOTs, the two clouds are caught in distinct magnetic quadrupole traps and then mixed by merging the two traps mechanically. I have demonstrated that the method is indeed feasible and a promising new way of producing mixtures of cold atoms, but it requires a suitable experimental setup and accurate control of various parameters. The procedure makes it possible to optimize the cooling and trapping process of each species individually and it is a modular approach where one can build the setup needed for producing one species and then add the other one when needed.

I describe the experimental procedure in Sec. 3.2. Section 3.3 is devoted to a discussion of the trapping potential and its evolution during the mixing process. In section 3.4 I introduce a simple theoretical model which I use to simulate the atomic particle trajectories in order to make predictions about the outcome and to understand the physics of the mixing process. In

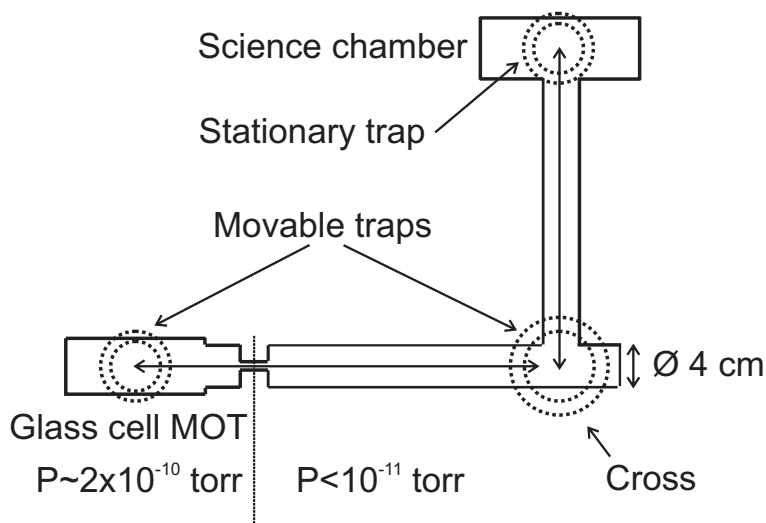


Figure 3.1: Schematic experimental setup. The coils constituting the magnetic traps are symbolized by the dashed circles. The distance from the MOT to the cross and from the cross to the science chamber is 49 cm and 37 cm, respectively.

section 3.5 I discuss our experimental results and compare them with the results of the theoretical model which turn out to reproduce the essential features quite well. I examine the dependence on essential parameters such as relative and absolute trap depths. Finally the mixing process is put into perspective in Sec. 3.6 where calculations on mixing of different elements is presented and in Sec. 3.7 where an alternative mixing scheme is discussed. I conclude in section 3.8.

3.2 Experimental procedure

To mix the atomic clouds I use the two movable magnetic traps termed “MOT coils” and “conveyor coils” in Fig. 2.1. The setup is shown schematically in Fig. 3.1. From now on, I will refer to the trap created by the “MOT coils” as Trap 1 and to the trap created by the “conveyor coils” as Trap 2. To study the principle of mixing by merging two magnetic traps I have mixed two clouds of ^{87}Rb in the $|F = 1, m_F = -1\rangle$ hyperfine state. About 40 % of the atoms are caught in Trap 1 when the current in the coils is ramped up to 150 A (see Tab. 2.1). After a wait of 55 ms the current is increased further to 250 A in 200 ms before moving the atoms through the differential pumping hole.

The mixing procedure is explained in detail in Fig. 3.2. When atoms have been caught in the traps, Trap 1 is moved towards Trap 2 at a speed of 5 cm/s. Trap 2 is stationary during the process. Both clouds are situated in

the “low pressure” part of the chamber during the process. After the mixing process the atoms are moved to the science chamber and transferred to the quadrupole trap created by the “static QP coils” in Fig. 2.1. Here I let the atoms wait for 10 s to allow for thermalization before I take absorption images after 7, 9, 11 and 13 ms time-of-flight to measure the temperature and number of atoms.

In order to study how each of the atomic clouds is influenced by the process, I can choose to have atoms in one or the other of the two traps or in both of them. I do this by having the cooling light either on or off during each of the two MOT phases.

3.3 Magnetic field and trapping potential

The coils of Trap 1 and Trap 2 have 16, respectively 31, windings. I have calculated the magnetic field from the coils using a numerical implementation of the Biot-Savart law. As it turns out, these calculations show that for our purposes the magnetic field from the coils can be very accurately approximated by the field from two circular windings, if A , R and I are chosen properly (see Fig. 2.10). The validity of this approximation makes the numerical simulations much faster and it is also important from a more fundamental point of view, because it shows that if the mixing process works with our coils, it should work just as well for other coils with the same effective values of A , R and I .

Due to the interference between the fields from the two traps during the mixing process, the magnetic field from each trap needs to be accurately determined in the radial direction even at distances up to 20 cm. Therefore, to find optimum values of A , R and I , I fit the Biot-Savart calculation for $B_\rho(\rho)$ in the $z = 0$ plane with 1 A through the actual coils with the corresponding function for a single pair of circular windings using A , R and I as fitting parameters.

This representation is very good: Within 2 cm from the $z=0$ plane the maximum deviation is 8 mG. The fits are shown in Figs. 3.3-3.4 and the best fitting values of A , R and I are listed in Tab. 3.1.

Table 3.1: Circular coil pair parameters.

Coil	Trap 1	Trap 2
A (cm)	3.941	7.082
R (cm)	3.2	4.21
I (A)	16.0	32.17
Radial field gradient (G/cm)/A	0.36	0.20
Field barrier height (G/A)	0.77	0.59

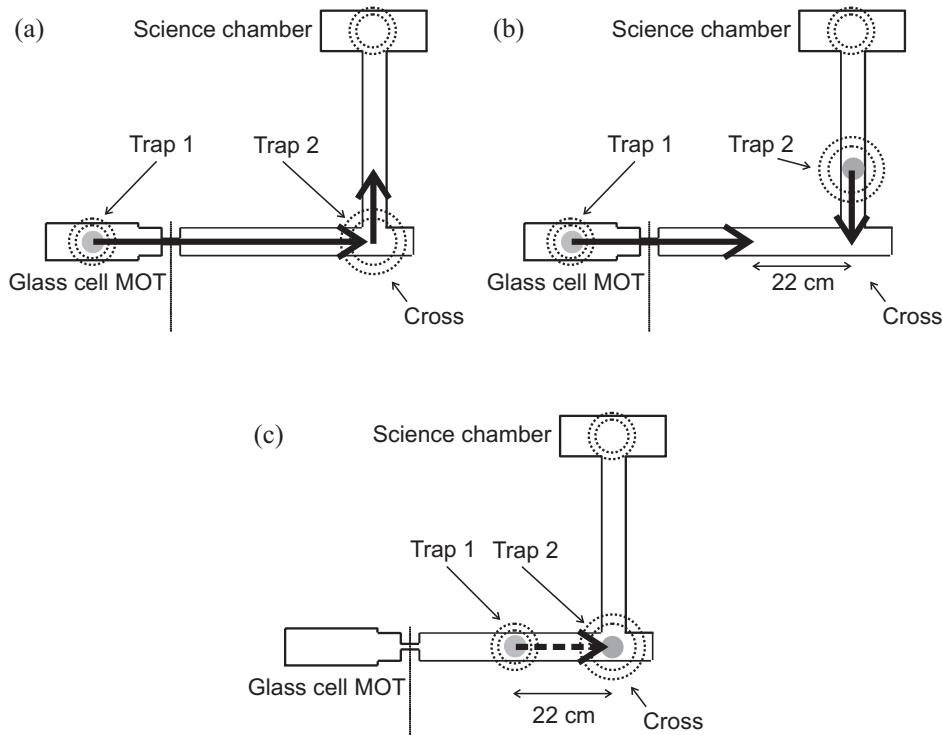


Figure 3.2: The procedure used to mix two Rb clouds. (a): First atoms are collected in the MOT and trapped in Trap 1. Then the trap is moved to the cross where the atoms are transferred into the other movable trap (Trap 2). This trap is moved 7 cm towards the science chamber to shield the atoms from scattered light. (b): Trap 1 is moved back and a second cloud of atoms is collected. This cloud is moved into the “low pressure” part of the chamber to a position 22 cm from the cross. The trap current is slowly changed to the initial value wanted during the mixing. Trap 2 is moved back to the cross. (c): Finally the two traps are merged by slowly (5 cm/s) moving Trap 1 towards the cross until the trap axes are 2 cm apart. This is the mixing process. The traps cannot be moved closer together due to the limited space around the vacuum chamber. For the same reason Trap 2 is displaced 5 mm from the transport axis of Trap 1.

I use the current ramps sketched in Fig. 3.5. The current in the coils constituting Trap 2 is constant throughout the mixing process. The current in the moving Trap 1 is constant in the beginning but is linearly ramped down to 0 A towards the end such that it is 0 exactly when the movement stops. Also shown is the position of Trap 1 as a function of time. I use soft acceleration and deceleration phases (with constant time derivative of the acceleration), but most of the time the velocity is constant. The velocity

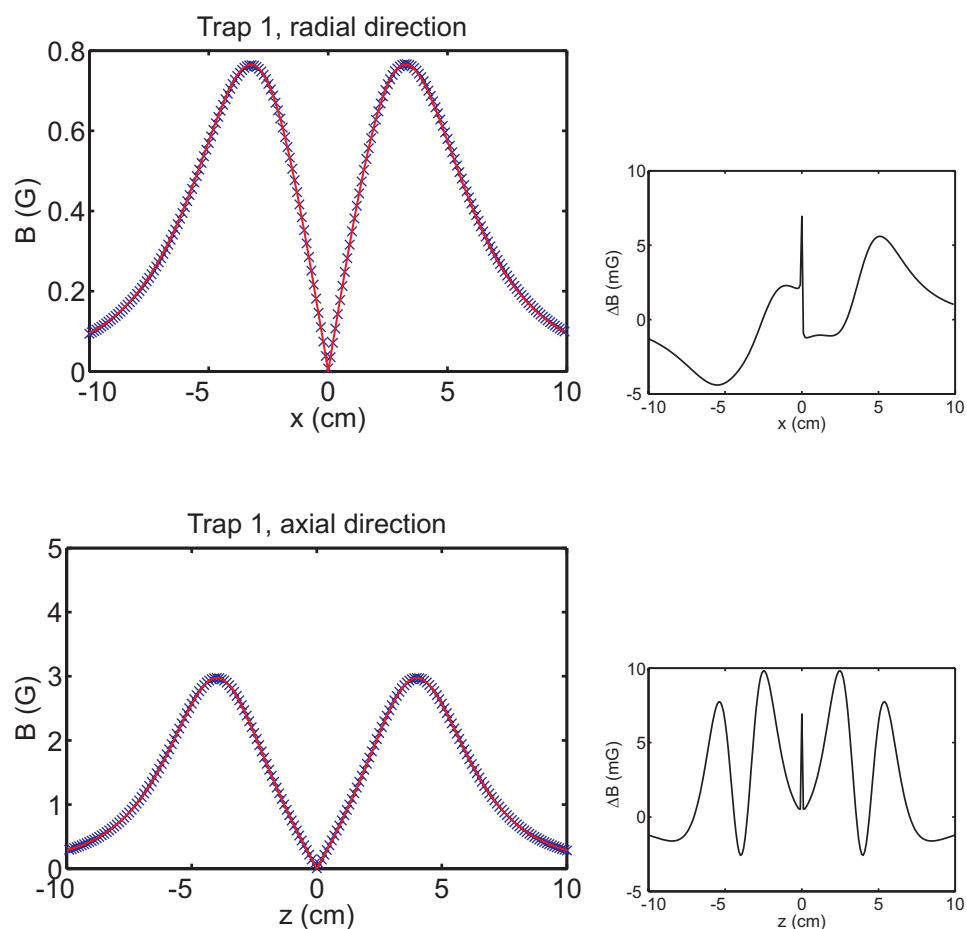


Figure 3.3: Plot of the fit of the magnetic field from Trap 1 to the field from a circular coil pair (the fit is carried out in the radial direction). The blue crosses are Biot-Savart law calculations of the field from the real coils and the red line is the best fit. The small plots to the right show the residues in mG. The sharp peak of the residues in the middle of the trap occurs because there the Biot-Savart implementation is inaccurate due to the discontinuity of the field gradient (so in the middle of the trap the fit is actually better than the Biot-Savart calculation).

during the acceleration phase is given by

$$v(t) = \begin{cases} \frac{1}{2} \frac{a^2}{V} t^2 & t \leq V/a \\ V - \frac{1}{2} \frac{a^2}{V} \left(\frac{2V}{a} - t \right)^2 & V/a \leq t \leq 2V/a \\ V & t \geq 2V/a \end{cases} \quad (3.1)$$

where $a = 20 \text{ cm/s}^2$ and $V = 5 \text{ cm/s}$ is the final velocity. The deceleration is similar, but reversed.

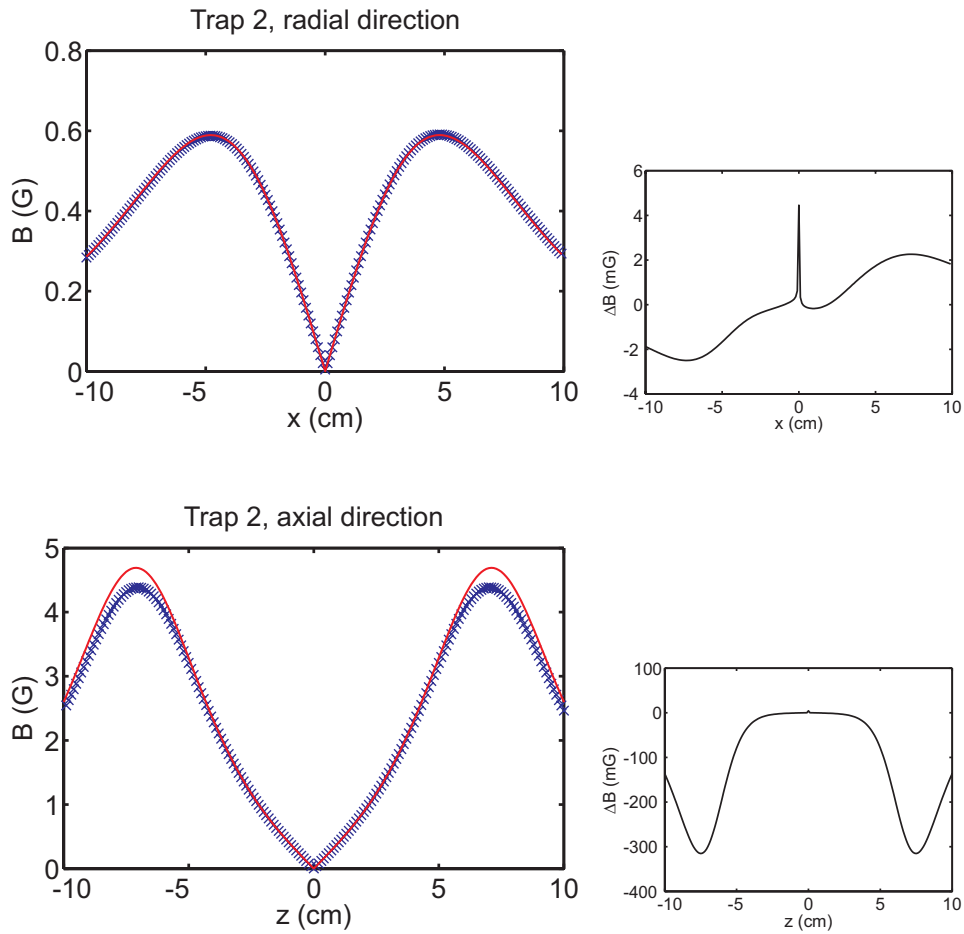


Figure 3.4: Plot of the fit of the magnetic field from Trap 2 to the field from a circular coil pair (the fit is carried out in the radial direction). See the caption of Fig. 3.3 for further details.

I have tried to vary the time Δt , during which the current of Trap 1 is ramped down, keeping the total mixing time constant (see Fig. 3.5). I found that the exact value of Δt is not critical as long as it is larger than 1.5 s. Ramping down the current of Trap 1 faster than that causes additional heating (but essentially no loss of atoms). The optimal ratio of initial currents in the two traps is strongly dependent on the value of Δt .

I have also tried to make deviations from the current ramp in Fig. 3.5 by ramping down in two linear steps instead of one. This, however does not lead to any improvement of the results. One could imagine that a suitably tailored soft curve would lead to marginally better results, but since the results using the simple linear ramp are quite satisfactory I have not pursued this issue further.

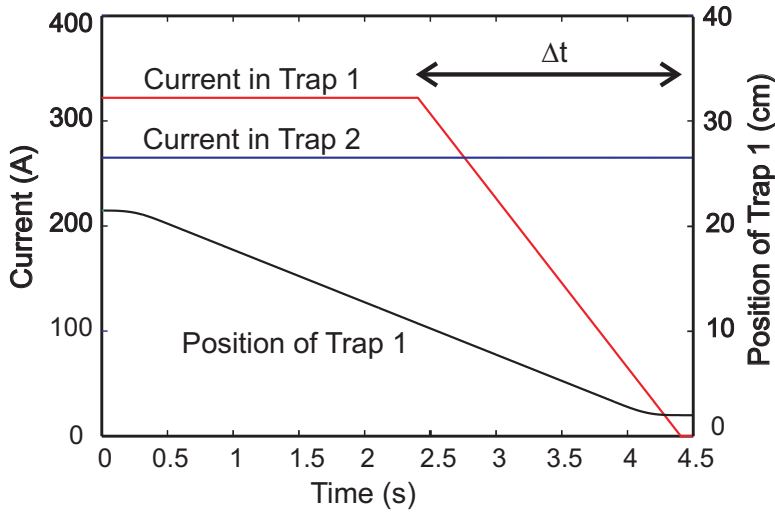


Figure 3.5: Current ramps and the position of Trap 1 during the mixing process.

The current ramp must be accurately synchronized with the movement of Trap 1. We apply a reset procedure on the mechanical positioning system to eliminate day-to-day drifts in the trap position. After reset the uncertainty in the coil position is about $50 \mu\text{m}$. By taking images of the trap coils during the movement I have determined the exact position as a function of time (Fig. 3.6) and used this information to time the current ramp such that the current in Trap 1 becomes zero exactly when the trap has reached the final position. By using the same procedure we can conclude that the timing drifts of the trap movement is less than 10 ms and this level of stability is indeed necessary to get reproducible results.

Armed with a precise magnetic field calculation it is possible to study the geometry of the trap potential during the mixing process. This is best viewed by plotting potential energy isosurfaces of the magnetic field. Some representative isosurfaces are shown in Fig. 3.7. The shown isosurfaces correspond to an energy of $k \times 1 \text{ mK}$ for $F = 1$ atoms where k is Boltzmann's constant. Gravity is also included in the calculations. If the atomic clouds were in thermal equilibrium during the mixing process (and I stress that they are not) 35 % of the atoms would reside outside these isosurfaces at a temperature of $200 \mu\text{K}$ as shown in Sec. 3.4.1. Therefore it is certainly not clear from these isosurfaces that the mixing can be done successfully, but nevertheless they give an impression of what is going on.

When the two traps are far apart there are 3 isosurfaces - one around the two trap centers and one between the two traps. The isosurface in the middle contains no atoms in the beginning.

As the traps are moving closer together, the potential gets weaker and

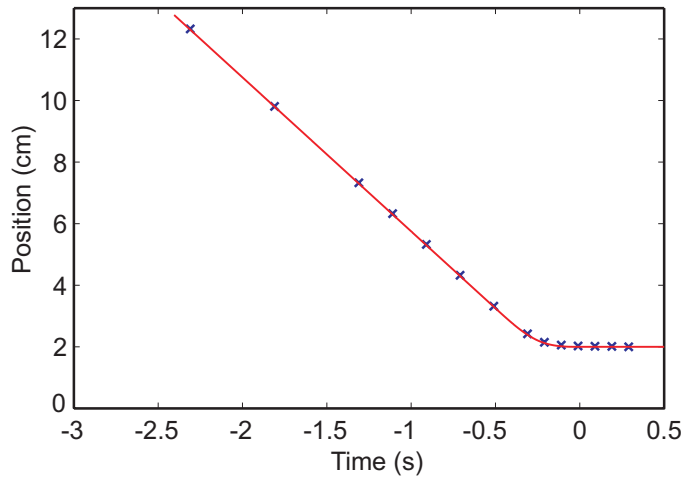


Figure 3.6: Position of Trap 1 during the mixing process (blue crosses) together with the calculated position of the trap using the velocity and the stop time as fitting parameters (red curve). The trap position was determined from digital images of the coils taken at well defined times during the process. The calculated position only fits the measured one if the stop time is correctly chosen to within about 10 ms.

the isosurfaces begin to mix which makes it possible for the atoms to leak into the region in the middle. This is the critical point since the atoms are thermodynamically allowed to spread out over a large volume. That can eventually cause heating when the trap potential tightens again at the end of the mixing process and can lead to loss if atoms hit the wall of the \varnothing 40 mm vacuum chamber tube. Shortly after this, all 3 isosurfaces are merged and in the end we are left with only one isosurface which ideally contains all the atoms.

If the current I_1 in Trap 1 is too small compared to the current I_2 in Trap 2, then the isosurface of Trap 1 mixes with the isosurface in the middle too early and the atoms in this trap are lost. On the other hand, if the ratio I_1/I_2 is too large, the atoms in Trap 2 are lost (see Fig. 3.8). This is exactly what we see experimentally (Fig. 3.9), and fortunately there is a well defined current ratio which leads to successful mixing.

3.4 Classical simulation of the dynamics

In order to get a theoretical understanding of the mixing process I have carried out simulations of the particle dynamics. The temperature of the clouds is so high that quantum effects can be safely neglected. One way to see this, is to consider the typical spacing between quantum mechanical energy levels in the linear trap potential. From dimensional arguments, or

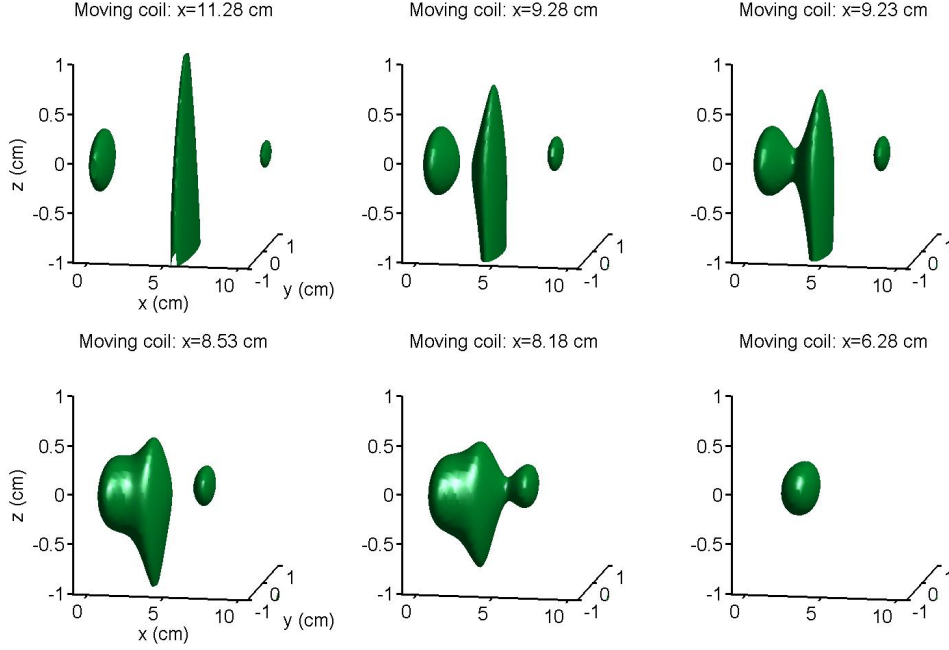


Figure 3.7: Selection of potential energy isosurfaces during the mixing process with optimal parameters. The surfaces correspond to a potential energy of $k \times 1$ mK for $F = 1$ atoms. At a temperature of $200 \mu\text{K}$ 65 % of the atoms would stay inside these isosurfaces in thermal equilibrium (however, I stress that the atoms are not in thermal equilibrium during the mixing process). Notice that the time interval between the third and the fifth plot is only 0.2 s. The vertical asymmetry at large distances from the $z=0$ plane is due to gravity. The current ramps are as in Fig. 3.5. The current in Trap 2 (situated at $x = 0$ cm) is $I_2=265$ A and the initial current in Trap 1 is $I_1 = 322$ A corresponding to the ratio $I_1/I_2 = 1.215$.

by looking at the energy levels in the 1-dimensional potential $V(x) = C|x|$ ([73] p. 109), this spacing is of the order of

$$E = \left(\frac{C^2 \hbar^2}{m} \right)^{1/3} = k \times 0.2 \mu\text{K} \quad (3.2)$$

where k is Boltzmann's constant using the worst case parameter $C = \mu_B \times 150$ G/cm. This is 3 orders of magnitude smaller than the typical thermal energy¹. Furthermore I neglect interactions and collisions between the particles. See section 3.4.1 for a discussion of this approximation.

So I propagate the particles classically:

$$\mathbf{v}_i = \frac{d\mathbf{r}_i}{dt} \quad m_i \frac{d\mathbf{v}_i}{dt} = -\nabla U(\mathbf{r}_i) \quad (3.3)$$

¹For a reference on the quantum theory of the quadrupole trap, see [129].

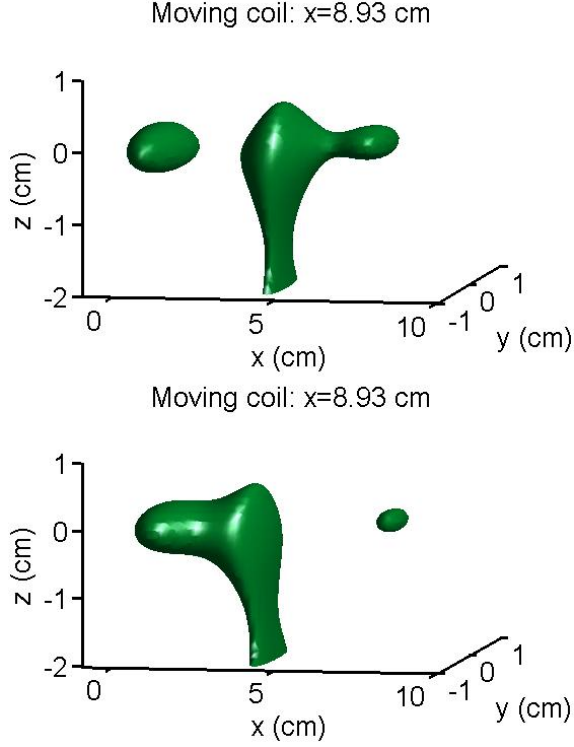


Figure 3.8: Isosurfaces corresponding to a potential energy of $k \times 1$ mK for current ratios which are far from optimal. The current in the coils of Trap 2 (situated at $x = 0$ cm) is $I_2 = 265$ A. The initial current in Trap 1 (situated at $x = 8.93$ cm) is respectively $I_1 = 280$ A (upper figure) and 350 A (lower figure). The figure shows that if the current ratio I_1/I_2 is too small, the atoms in Trap 1 are likely to become lost or heated. If it is too large, the atoms in Trap 2 are likely to suffer from loss or heating. Notice that the scales of the axes are different from those in Fig. 3.7.

\mathbf{r}_i being the position of each particle. I implement $\nabla U = g_F m_F \mu_B \nabla B + mg \hat{z}$ numerically and solve the equations using a standard multi-order Runge-Kutta method with error control in Matlab. The dynamics is rather complicated and cannot be described analytically. However, all particle trajectories exhibit some oscillatory kind of behaviour with a characteristic period with an order of magnitude given by the cyclotron period

$$2\pi \sqrt{\frac{m\rho}{g_F m_F \mu_B \times \partial|B|/\partial\rho}} \quad (3.4)$$

which is about 40 ms initially. Two examples of particle trajectories are shown in Fig. 3.10.

From the result of such a simulation it is possible to extract various interesting quantities like position, extension and temperature (Fig. 3.11)

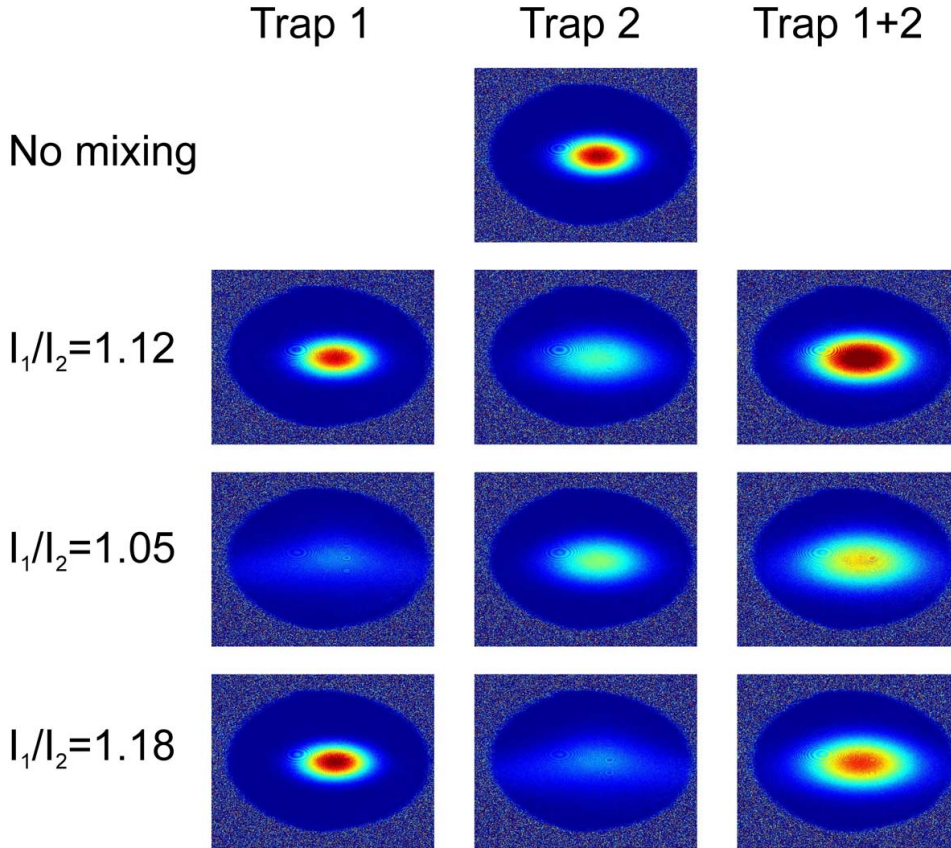


Figure 3.9: Representative images of atomic clouds from experimental runs. The uppermost image shows an atomic cloud which has just been moved to the science chamber without going through the mixing process. All the other images show atomic clouds which have gone through a mixing process with current ratios of 1.12, 1.05, and 1.18, respectively. The images in the left column were taken with atoms only in Trap 1 initially, the images in the middle column were taken with atoms only in Trap 2 initially, while the images in the right column were taken with atoms both in Trap 1 and 2 initially. Each image corresponds to a physical size of $19.8 \text{ mm} \times 14.9 \text{ mm}$ (1600×1200 pixels with $12.4 \mu\text{m}/\text{pixel}$). The images illustrate the fact that the atoms in Trap 1 suffer from loss and heating if the current ratio is too low (the cloud becomes very diffuse). Similarly, if the current ratio is too high, the cloud in Trap 2 becomes very diffuse.

of the atomic clouds as a function of time. It is easy to discriminate the lost particles from the particles that stay trapped since the former perform a nearly free fall in the field of gravity and will quickly travel far away from the trapping region. Since our vacuum chamber tube has a diameter of 4 cm, particles which during the process reach a position which is more than 2 cm away from the transport axis are considered lost and removed from

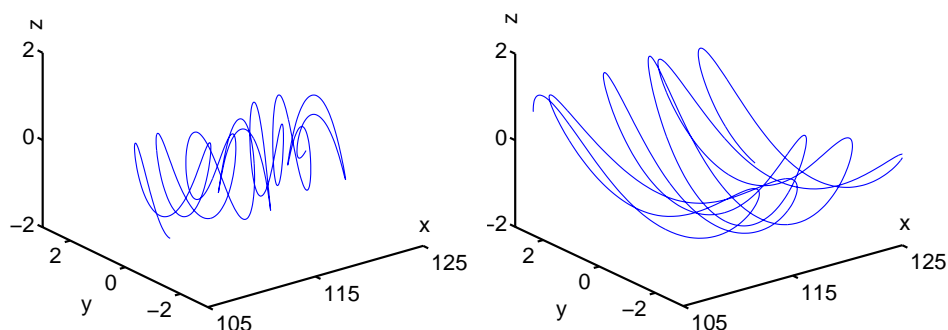


Figure 3.10: Two examples of particle trajectories of atoms in Trap 1 during the mixing process from $t = 2.0$ s to $t = 2.3$ s. The trap moves in the negative direction of the x -axis. The unit of position is mm.

the calculation before calculating the thermodynamic quantities.

Using optimal parameters it turns out that if we consider the atoms originating from Trap 1 and Trap 2 individually, then the kinetic and potential energies correspond to the same effective temperature and there is almost no anisotropy of the velocity distribution. This means that these ensembles are not far from thermal equilibrium at the end of the mixing process. But the ensemble from Trap 1 is not in thermal equilibrium with the ensemble from Trap 2. However, since thermalization takes place through elastic collisions, the equilibrium temperature of the mixed cloud as a whole can be found from the conserved mean energy, since in thermal equilibrium $\langle E \rangle = \langle E_{\text{kin}} \rangle + \langle U \rangle = (9/2)kT$ as described in section 3.4.1. Also the equilibrium phase space density can be calculated.

3.4.1 Thermodynamics of the quadrupole trap

A basic understanding of the thermodynamic properties of the quadrupole trap is important both in order to interpret experimental results correctly and in order to understand the mixing process theoretically. Using the approximation (2.10) thermodynamic equilibrium quantities of the trapped atoms can be calculated. We introduce the radial trap potential gradient

$$C = g_{\text{F}} m_{\text{F}} \mu_{\text{B}} \left. \frac{\partial |B|}{\partial \rho} \right|_{\mathbf{r}=0}. \quad (3.5)$$

The probability $P(\mathbf{r}, \mathbf{p})$ of finding an atom within a certain volume $d^3\mathbf{r}$ in position space and $d^3\mathbf{p}$ in momentum space is given by the Boltzmann distribution:

$$P(\mathbf{r}, \mathbf{p}) d^3\mathbf{r} d^3\mathbf{p} = \frac{e^{-\beta E}}{Z} = \frac{e^{-\beta p^2/2m}}{Z_{\mathbf{r}}} \frac{e^{-\beta C \sqrt{\rho^2 + 4z^2}}}{Z_{\mathbf{p}}} \quad (3.6)$$

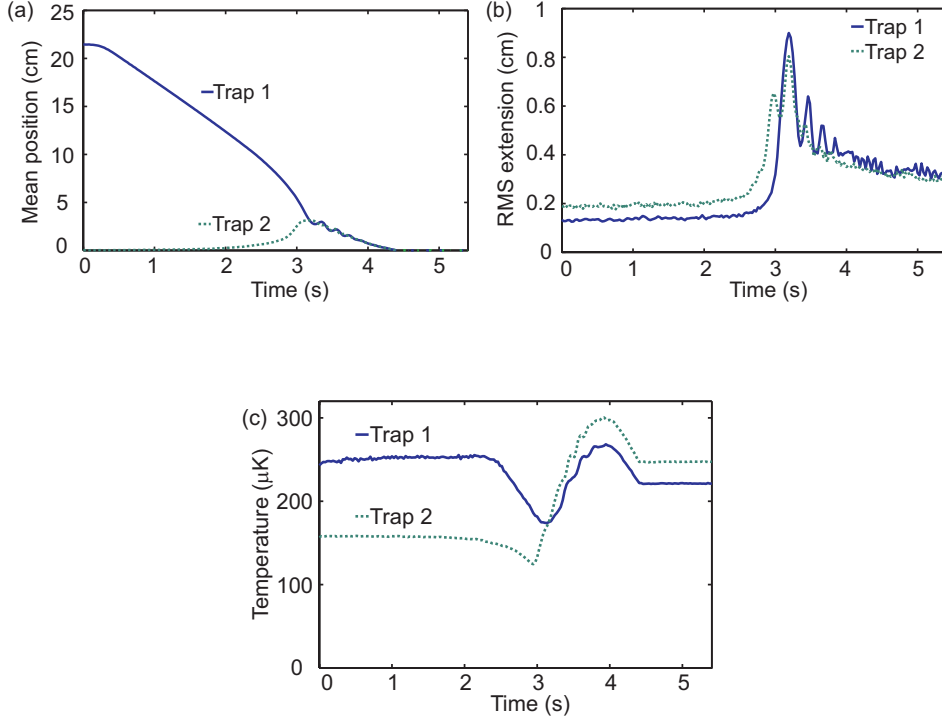


Figure 3.11: Results of a simulation of the particle dynamics using the current ratio $I_1/I_2 = 1.215$ which gives the optimal mixing results according to the simulations. (a) shows the position of the two clouds (the mean position of the atoms) as a function of time. (b) shows the RMS extension of the clouds in the mixing direction. (c) shows the mean energy of the two clouds expressed as the corresponding equilibrium temperature $T = (2/9k)\langle E \rangle$. The temperature temporarily decreases just before the clouds merge, because the trap potential opens up. Since the potential energy gradient of Trap 2 is smaller than the initial gradient of Trap 1 the phase space density of the cloud in Trap 1 decreases even if the final temperature is not higher than the initial one. Particles which are lost during the mixing process have been removed from the calculation.

where $\beta = 1/(kT)$ and the partition function $Z = Z_{\mathbf{r}}Z_{\mathbf{p}}$ is given by

$$Z_{\mathbf{r}} = \int d^3\mathbf{r} e^{-\beta C \sqrt{\rho^2 + 4z^2}} = 2\pi \int_{-\infty}^{\infty} dz \int_0^{\infty} d\rho \rho e^{-\beta C \sqrt{\rho^2 + 4z^2}} \quad (3.7)$$

$$Z_{\mathbf{p}} = \int d^3\mathbf{p} e^{-\beta p^2/2m} = 4\pi \int_0^{\infty} p^2 e^{-\beta p^2/2m} dp = \left(\frac{2\pi m}{\beta}\right)^{3/2}. \quad (3.8)$$

To calculate the spatial integral $Z_{\mathbf{r}}$ we introduce the scaled lengths

$$\rho' = \beta C \rho \quad z' = 2\beta C z \quad (3.9)$$

to give

$$Z_{\mathbf{r}} = \frac{\pi}{(\beta C)^3} \int_{-\infty}^{\infty} dz' \int_0^{\infty} d\rho' \rho' e^{-\sqrt{\rho'^2 + z'^2}} \quad (3.10)$$

$$= \frac{\pi}{(\beta C)^3} \int_{-\pi/2}^{\pi/2} d\theta' \cos \theta' \int_0^{\infty} dr' r'^2 e^{-r'} \quad (3.11)$$

$$= \frac{4\pi}{(\beta C)^3} \quad (3.12)$$

where polar coordinates in the (ρ', z') -plane are used in the last step. So the spatial density is

$$\boxed{n(\mathbf{r}) = \frac{N}{4\pi} \left(\frac{C}{kT} \right)^3 e^{-C\sqrt{\rho^2 + 4z^2}/kT}} \quad (3.13)$$

where N is the number of atoms. The velocity has the same distribution as that of an untrapped, ideal gas. It is worth noting that the fact that the Boltzmann distribution factorizes into spatial and momentum parts means that the probability that a particle has a certain velocity is independent of its position in the trap (naively one might guess that atoms which are close to the bottom of the trap are faster).

From the density we can calculate the RMS extensions of the cloud. For instance

$$\rho_{\text{RMS}} = \sqrt{\int \rho^2 n(\mathbf{r}) d^3\mathbf{r}} = 0.42 \text{ mm} \cdot \frac{T}{100 \mu\text{K}} \cdot \frac{1}{g_{\text{F}} m_{\text{F}}} \frac{100 \text{ G/cm}}{\partial|B|/\partial\rho} \quad (3.14)$$

$$z_{\text{RMS}} = \sqrt{\int z^2 n(\mathbf{r}) d^3\mathbf{r}} = 0.15 \text{ mm} \cdot \frac{T}{100 \mu\text{K}} \cdot \frac{1}{g_{\text{F}} m_{\text{F}}} \frac{100 \text{ G/cm}}{\partial|B|/\partial\rho} \quad (3.15)$$

The peak phase space density is

$$\boxed{n(\mathbf{r} = \mathbf{0}) \lambda_{\text{dB}}^3 = \frac{N}{4\pi} \left(\frac{C}{kT} \right)^3 \left(\frac{h^2}{2\pi m kT} \right)^{3/2} \propto N C^3 T^{-9/2}.} \quad (3.16)$$

The mean kinetic energy per atom is

$$\langle E_{\text{kin}} \rangle = -\frac{\partial}{\partial\beta} \ln Z_{\mathbf{p}} = \frac{3}{2} kT \quad (3.17)$$

as for an ideal, untrapped gas. The potential energy per atom becomes

$$\langle U \rangle = -\frac{\partial}{\partial\beta} \ln Z_{\mathbf{r}} = 3kT \quad (3.18)$$

These two results can be traced back to the fact that the energy is quadratic in momentum and linear in position.

In order to determine the mean elastic collision rate we need to know the mean density which is given by

$$\langle n(\mathbf{r}) \rangle = \int d^3\mathbf{r} n(\mathbf{r}) \frac{n(\mathbf{r})}{N} \quad (3.19)$$

$$= \frac{1}{N} \int d^3\mathbf{r} n(\mathbf{r} = 0)^2 e^{-2C\sqrt{\rho^2+4z^2}} \quad (3.20)$$

$$= \frac{n(\mathbf{r} = 0)}{N} \int d^3\mathbf{r} n(2\mathbf{r}) \quad (3.21)$$

$$= \frac{n(\mathbf{r} = 0)}{8N} \int d^3(2\mathbf{r}) n(2\mathbf{r}) \quad (3.22)$$

$$= \frac{1}{8} n(\mathbf{r} = 0) \quad (3.23)$$

The mean time between elastic collisions is (see 1.22)

$$\tau_{\text{el}} = (\langle n \rangle \sigma \langle v_{\text{rel}} \rangle)^{-1} \quad (3.24)$$

$$= 19 \text{ ms} \cdot \frac{10^8}{N} \left(\frac{T}{100 \mu\text{K}} \right)^{5/2} \left(\frac{1}{g_{\text{F}} m_{\text{F}}} \frac{100 \text{ G/cm}}{\partial|B|/\partial\rho} \right)^3 \quad (3.25)$$

using the scattering length $a = 106 a_0$ from [57, 130], the cross section $\sigma = 8\pi a^2$ (see 1.21) and the mean relative velocity $\langle v_{\text{rel}} \rangle = \sqrt{8kT/(\pi m/2)}$ (see 1.25). For the experimental parameters used in this work τ lies in the range 1-8 s in the science chamber trap.

The density of states can also be calculated (I use the formula for the density of states from [128]):

$$\begin{aligned} g(E) &= \frac{2\pi(2m)^{3/2}}{h^3} \int_{U(\mathbf{r}) \leq E} d^3\mathbf{r} \sqrt{E - U(\mathbf{r})} \\ &= \frac{2\pi(2m)^{3/2}}{h^3} \frac{2\pi}{2C^3} E^{7/2} \int_{-\pi/2}^{\pi/2} d\theta' \cos \theta' \int_0^1 dr' r'^2 \sqrt{1 - r'^2} \\ &= \frac{2\pi(2m)^{3/2}}{h^3} \frac{2\pi}{2C^3} \frac{32}{105} E^{7/2} \end{aligned} \quad (3.26)$$

the important thing here being the $E^{7/2}$ -dependence. Knowing this, we can for instance calculate the probability that an atom has a total energy which is larger than $5kT$:

$$\text{Probability that } E > 5kT : \frac{\int_{5kT}^{\infty} g(E) dE e^{-\beta E}}{\int_0^{\infty} g(E) dE e^{-\beta E}} = \frac{\int_5^{\infty} d\epsilon \epsilon^{7/2} e^{-\epsilon}}{\int_0^{\infty} d\epsilon \epsilon^{7/2} e^{-\epsilon}} = 35 \%. \quad (3.27)$$

so in thermal equilibrium 35 % of the atoms would have an energy exceeding $5kT$.

3.4.2 Initial conditions

In each trap, an ensemble of 500 particles obeying Boltzmann statistics is prepared. I assume that the phase space density is conserved during transport and adiabatic compression [4] so I choose the initial temperature such that the phase space density matches the one determined from temperature measurements in the science chamber. At a radial trap gradient of $\partial|B|/\partial\rho = 84$ G/cm I measure the temperature of a cloud which has not gone through the mixing process to be $195 \mu\text{K}$. Using the scaling of the phase space density (3.16) we see that the proper initial temperature is

$$T_{\text{init}} = \left(\frac{84 \text{ G/cm}}{\partial|B|/\partial\rho} \right)^{-2/3} \times 195 \mu\text{K} \quad (3.28)$$

so the two clouds have different temperatures but the same phase space density.

The initial velocities are found by selecting each Cartesian component randomly from the Gaussian distribution:

$$P(v_j) \propto e^{-\frac{1}{2}mv_j^2/kT_{\text{init}}}, \quad j = x, y, z. \quad (3.29)$$

I distribute the positions using a rejection method: First I choose random coordinates uniformly (within intervals so large that the probability for being outside this volume is less than 10^{-4}). The probability that the chosen position occurs physically is proportional to $e^{-U(\mathbf{r})/kT_{\text{init}}}$ so by choosing another random number p uniformly between 0 and 1 we can decide whether this position shall be accepted (if $p < e^{-U(\mathbf{r})/kT_{\text{init}}}$) or rejected (if $p > e^{-U(\mathbf{r})/kT_{\text{init}}}$).

3.5 Results

Using optimal parameters I get the following experimental main result: If I mix two clouds with about 1.7×10^8 atoms each, I loose only about 5% of the atoms and the measured temperature in the science chamber increases from $195 \mu\text{K}$ to $295 \mu\text{K}$. This means that according to Eq. (3.16) the final phase space density relative to the initial phase space density of the clouds is 32 %. Using optimal parameters in the theoretical model I get a relative phase space density of 27 % in very good agreement with the experimental result. The elastic collision rate is also important in relation to subsequent evaporative cooling. It scales as $N/T^{5/2}$ (see Eq. 3.25) which means that the mixed cloud has an elastic collision rate of about 70 % of the rate of the initial clouds. Based on this I conclude that it should be possible to cool the mixed cloud to quantum degeneracy using evaporative cooling.

The most critical parameter of the mixing process is the ratio I_1/I_2 of the currents in the coils of Trap 1 and Trap 2. This is discussed in section 3.5.1. There are several other parameters which can be varied in order to optimize the process. Here I look at the trap depth (section 3.5.2) and the initial temperature (3.5.3).

3.5.1 Dependence on trap current ratio

Keeping I_2 constant at 265 A which corresponds to a radial magnetic field gradient of 53 G/cm and changing the current ratio by varying I_1 , I get the experimental results shown in Fig. 3.12². The corresponding results of the theoretical simulations with the same parameters lead to the results in Fig. 3.13. The figures show (a) the number of atoms staying trapped during the process, (b) the final temperature, and (c) the final phase space density. In each of these plots the results are given for atoms in both traps and with atoms in only one or the other of the two traps. Thereby it is possible to determine which of the two clouds is lost or heated most during the process. It should be stressed that the uncertainty of the phase space density value is relatively large, because it decreases rapidly with temperature (see Eq. 3.16). A change in phase space density by a factor of 2 corresponds only to a temperature change of 17 %.

Both the experimental and theoretical plots show that, for large current ratios, the atoms in Trap 1 stay trapped during the mixing process without loss or heating, whereas a small current ratio favors the atoms in Trap 2. This confirms what one could expect from the isosurface plots in Fig. 3.8. Experimentally I see that when I have atoms in Trap 1 only and use a current ratio less than 1.06, I get a diffuse cloud which is very elongated in the horizontal direction (see Fig. 3.9) and not in thermal equilibrium. Therefore we cannot attribute a temperature to these clouds³. This is the reason why the curve for Trap 1 stops in the temperature and phase space density plots. The same situation applies when we have atoms only in Trap 2 at a current ratio exceeding 1.14. The number of atoms in these cases is determined from a sum of pixel values after 2 ms time-of-flight.

Fortunately it is possible to choose a current ratio which constitutes a compromise where the heating of the mixed cloud as a whole is small and almost no atoms are lost. Both experimentally and theoretically there is a

²The results plotted in (b) and (c) differ slightly from the ones in [1], because they are now based on the temperature given by the vertical widths as they should be according to Sec. 2.6.1. When we submitted the article we did not pay attention to the fact that the temperature determined from the vertical widths is the correct one and therefore we used the (slightly higher) temperature deduced from the horizontal widths to be conservative.

³Even when I let the atoms equilibrate for 30-50 s in the science chamber I cannot measure a consistent temperature. The measured temperature seems to increase in time, and from measurements of the more regular clouds, we know that this apparent temperature increase is not due to technical noise.

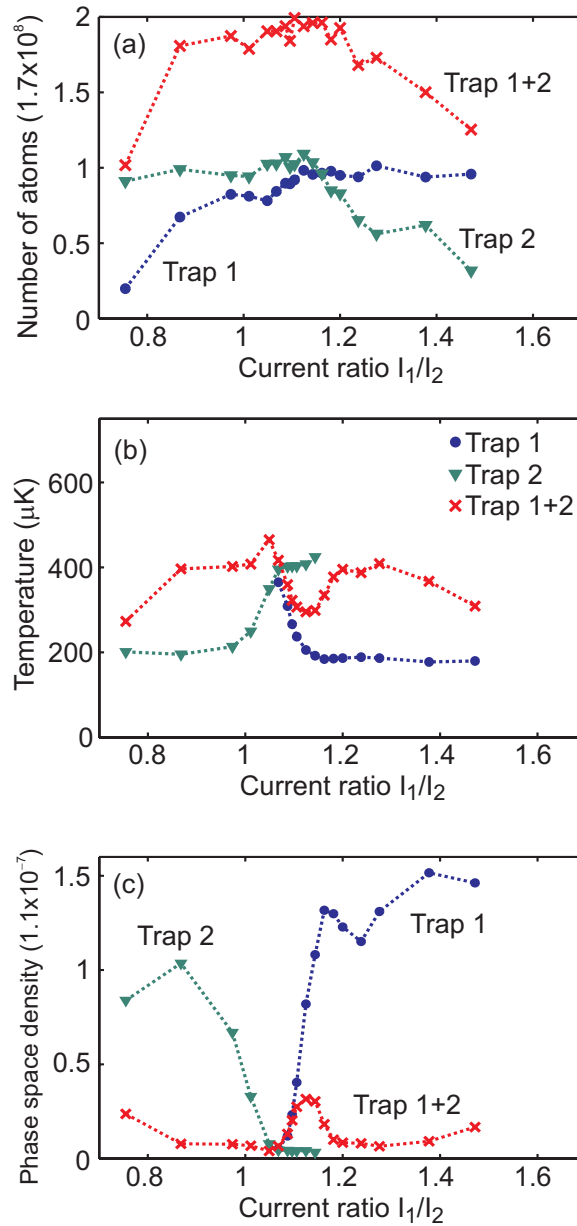


Figure 3.12: Experimental results of varying the ratio I_1/I_2 of the currents in the coils of Trap 1 and Trap 2, respectively (I_2 is kept constant at 265 A while I_1 is varied). (a) shows the number of atoms staying trapped during the process (normalized to the number of atoms in each of the initial clouds which is 1.7×10^8), (b) shows the final temperature and (c) shows the final phase space density (normalized to the value 1.1×10^{-7} which is the phase space density of an initial cloud with 1.7×10^8 atoms and a temperature of $195 \mu\text{K}$). All three plots contain three curves: One curve showing results with atoms in both traps and two curves showing results with atoms in only one or the other of the traps. The dotted lines between the points are drawn to guide the eye. See also the footnote ² on page 61.

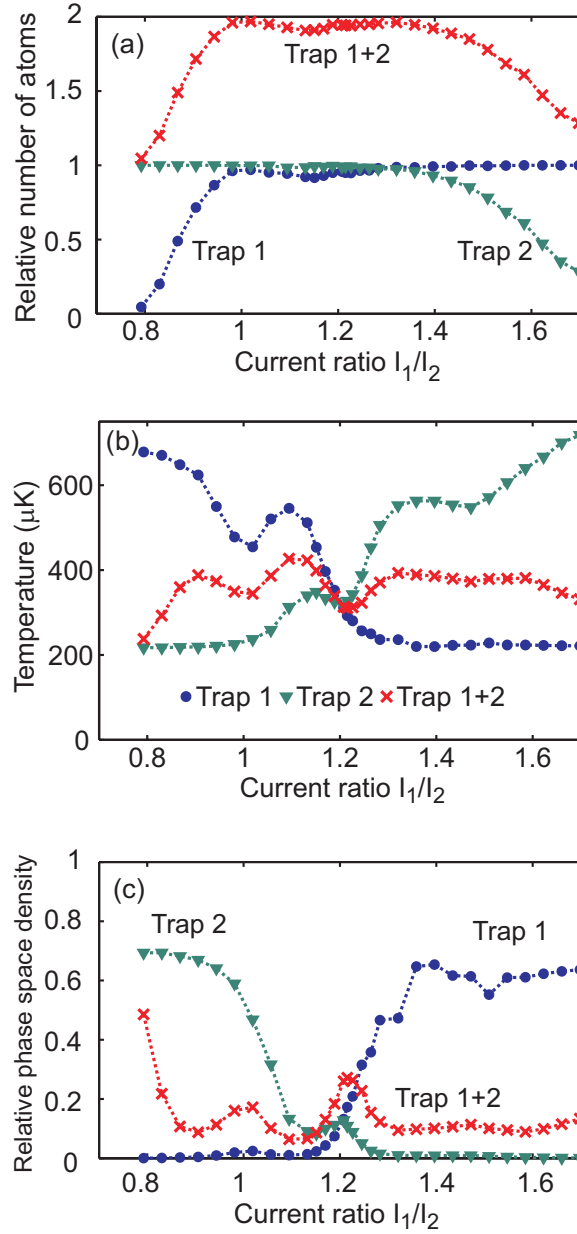


Figure 3.13: Theoretical results of varying the current ratio. The plots show the same quantities as the plot in Fig. 3.12. Atoms which escape the trap potential or hit the chamber wall during the mixing process are removed before calculating the temperatures and phase space densities. The number of atoms and the phase space density are normalized to the (identical) values of each of the initial clouds.

well defined current ratio which at the same time minimizes the temperature and maximizes the number of atoms of the mixed cloud. I will refer to this current ratio as the optimal current ratio. Experimentally it is 1.125 while in the theoretical calculations it is 1.215. We believe that the 8 % difference between these two values can be attributed to uncertainties in the calculation of the magnetic field from the coils.

The qualitative agreement between the measurements and the theoretical simulations is striking and also, bearing in mind that the optimal current ratio is slightly different, even the quantitative agreement is not bad. Similar to the experimental results, the theoretical simulations give a final phase space density of about 27 % of the initial phase space density of a single cloud at the optimal current ratio.

But there are also differences. The simulations result in two local maxima of the final phase space density whereas experimentally only one clear maximum is observed. Also, theoretically at the optimal current ratio, the phase space density of the atoms from each of the two traps is almost equal. Experimentally the phase space density is significantly larger when we have atoms only in Trap 1 than when we have atoms only in Trap 2 at the optimal current ratio. Taking the simplicity of the theoretical model into account one cannot expect perfect quantitative agreement. We recall that the model does not include the dynamics before and after the mixing process and it ignores collisions and interactions.

3.5.2 Dependence on trap depth

To the extent that gravity can be neglected, changing the trap depth only changes the magnitude and not the geometrical shape of the potential. Therefore this parameter is not expected to be very critical as long as the traps are deep enough that the atoms do not escape. This is confirmed by the measurements. First of all there is no measurable change in the optimal current ratio when I change the trap depth. For small trap depths the final temperature has no well defined minimum as I vary the current ratio, but the number of atoms peaks at a current ratio which is independent of trap depth. Therefore it makes sense to vary the trap depth keeping a constant current ratio in order to find out how deep the trap needs to be for the mixing process to work.

The number of atoms remaining trapped after mixing versus the trap depth is shown in Fig. 3.14, where the experimental and theoretical results are compared. They agree very well. For sufficiently deep traps there is essentially no loss of atoms. When the trap gradient becomes smaller than a critical value which is about 60 % of the value used above (which corresponds to a current of 265 A in Trap 2 giving an initial radial field gradient of 53 G/cm and a barrier height of 154 G - see Tab. 3.1) then trap losses start to set in. At a trap depth of 40 % of the value used above only 14 % of

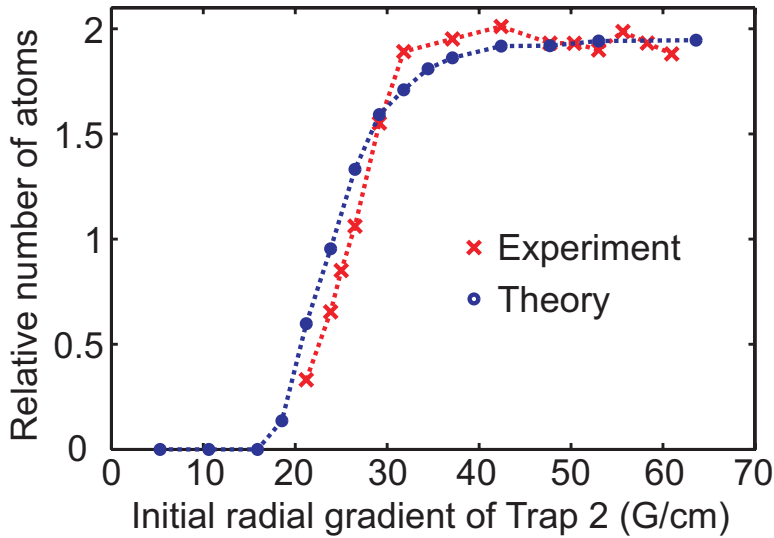


Figure 3.14: The number of atoms staying trapped during the mixing process relative to the initial number of atoms in each trap for different trap gradients. The measurements are normalized to 1.81×10^8 atoms. The current ratio is $I_1/I_2 = 1.125$ for the experimental results and 1.215 for the theoretical results. As long as the initial radial field gradient of Trap 2 is larger than 35 G/cm (corresponding to an initial barrier height of 92 G in Trap 2) the loss of atoms is only about 5 %. When the field gradient becomes smaller than this value a significant loss of atoms sets in. The experimental and theoretical results agree very well.

the atoms are left. I have also measured how the temperature of the mixed cloud depends on the trap depth. In the region with essentially no loss of atoms the temperature variations are less than 10 %. It should be kept in mind that these results are obtained for the $|F = 1, m_F = -1\rangle$ hyperfine state which has a magnetic moment of $\mu_B/2$. Using the $|F = 2, m_F = 2\rangle$ state, which has a magnetic moment of μ_B , the same potential energy can be achieved with a field that is only half as large.

3.5.3 Theoretical dependence on the initial temperature

To check how generally applicable the mixing procedure is, it is also interesting to look at the dependence on the initial temperature of the clouds which are mixed. I have studied this in the theoretical simulations using the radial field gradient 53 G/cm in Trap 2. In all the calculations I have used the current ratio 1.215 which is theoretically optimal at low temperatures (as long as there is essentially no loss of atoms). For higher temperatures the optimal current ratio is less well defined, because there is no clear minimum of the final temperature. This is because there is a significant loss of atoms and the most energetic atoms have the largest probability of escaping. The

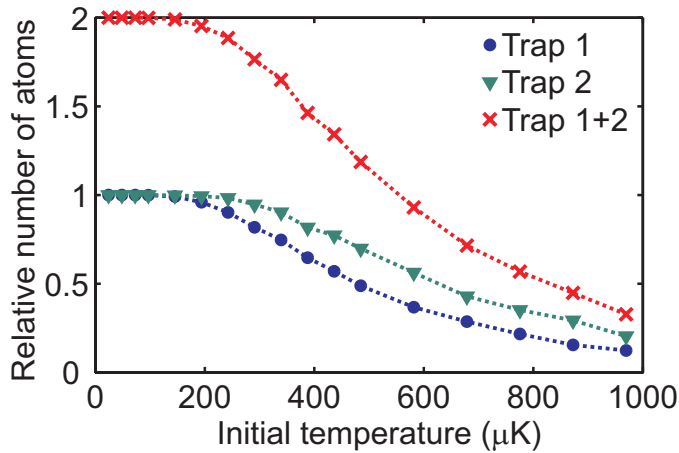


Figure 3.15: Results of simulations showing the fraction of atoms staying trapped during the mixing process for different initial temperatures at (given at $\partial|B|/\partial\rho = 84$ G/cm). For the trap gradient used (53 G/cm in trap 2) there is essentially no loss of atoms until the initial temperature rises above about 200 μK . At a temperature of 1000 μK only 15 % of the atoms stay trapped. The current ratio is 1.215. Each point corresponds to a simulation using 2×2000 atoms initially.

fraction of atoms remaining trapped after the mixing process is plotted in Fig. 3.15 and the final temperature is plotted in Fig. 3.16.

The figures show that up to an initial temperature of 200 μK (at $\partial|B|/\partial\rho = 84$ G/cm) all atoms stay trapped whereas for higher temperatures the loss gradually increases until at 1 mK 85 % of the atoms are lost. On the other hand one does not gain very much from having an even colder cloud initially since the absolute temperature increase is about 100 μK and roughly independent of the initial temperature up to an initial temperature of about 500 μK . For even higher temperatures the final temperature drops below the initial temperature, because the most energetic atoms escape the trapping potential or hit the vacuum chamber wall.

3.6 Mixing different species

Although of limited practical interest, mixing of two Rb clouds is an excellent way to study the process of mixing atomic clouds by merging two quadrupole traps. The perspective is to use the process to mix two different species. We hope that a cold mixture produced in this way can be a good starting point for making a quantum gas mixture. It is our intention to mix ^{87}Rb and ^6Li or ^7Li and do evaporative cooling on Rb to get both species into the quantum regime.

For alkali atoms it is normally preferable to have both species in the

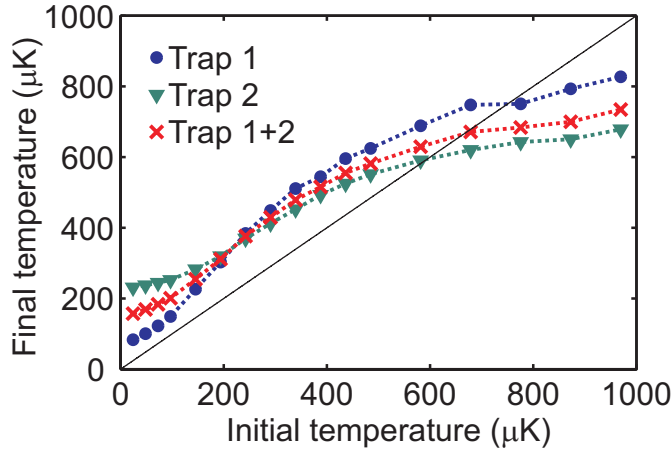


Figure 3.16: Theoretical dependence of the temperature after the mixing process on the initial temperature at a current ratio of 1.215 which is optimal for low temperatures. Up to an initial temperature of about 500 μK the absolute temperature increase is roughly independent of the initial temperature. For very low initial temperatures, the final temperature converges towards 150 μK for a mixture with equal numbers of atoms in the two traps. At this stage the properties of the mixed cloud are completely determined by the mixing process and independent of the initial temperature. Apparently, for the trap gradients used, the process is also feasible for higher temperatures, but then the most energetic atoms escape or hit the vacuum chamber wall. The thin black line shows the initial temperature for comparison.

stretched hyperfine state with $g_F m_F = 1$. Besides having the largest possible magnetic moment, the trapped atoms in such a mixture are least affected by loss due to spin-exchange collisions. Thus, assuming that both species are in a state with $g_F m_F = 1$, the only difference between the two species affecting the dynamics is their initial temperature (which is typically the same within a factor of two or so) and their mass which enters via Newton's 2nd law and via the initial velocity which has the mean value $v = \sqrt{8kT/(\pi m)}$.

Using our theoretical model which simulates the essential features of the Rb-Rb mixing very well, we can make predictions on the outcome of an experiment where two different species are mixed and the results are promising. I have simulated mixing of Rb in Trap 1 with Li, Na, K and Cs in Trap 2. The radial field gradient of Trap 2 was 53 G/cm as above such that the magnetic trapping potential is twice as large as the potential for the $|F = 1, m_F = -1\rangle$ ^{87}Rb atoms used above. I have chosen the initial temperature 250 μK at a radial trap gradient of 42 G/cm except for Li for which 500 μK is more realistic [131].

For current ratios in the range 1-1.45 the loss of atoms is below 5 % except for the Li cloud for which the loss is 8-12 %. Fig. 3.17 shows the

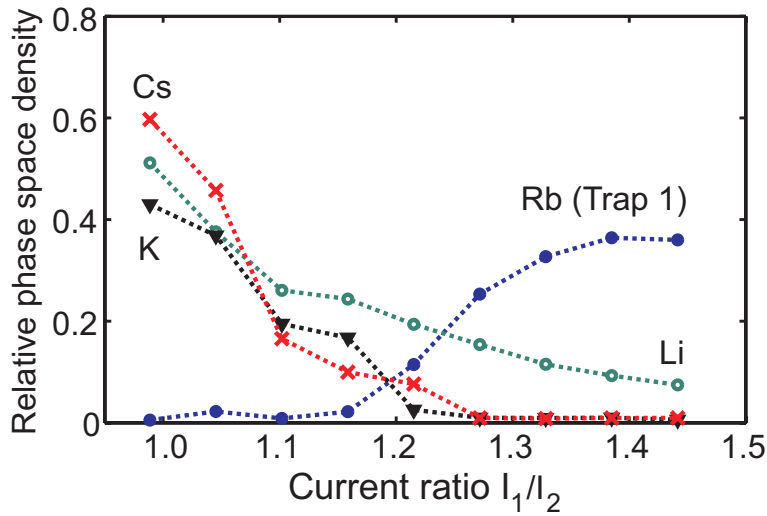


Figure 3.17: Simulation results of mixing of two different species. The plot shows the final phase space density of each of the clouds resulting from mixing of Rb in Trap 1 (\bullet) with respectively Li (\circ), K (\blacktriangledown) and Cs (\times) in Trap 2. The results for Na resembles the results for K very much. The temperature of the initial clouds at a radial field gradient of 42 G/cm is 250 μ K except for Li for which it is 500 μ K. The phase space densities are normalized to the values of the initial clouds. Each point corresponds to a simulation using 2×5000 atoms initially.

final phase space density relative to the initial phase space density of each of the clouds. Just as for Rb-Rb mixing the current ratio can be adjusted to favor one or the other of the two atomic clouds and there is a region of current ratios where the phase space densities of both species are retained at a reasonable level.

Since evaporative cooling is notoriously a very lossy process, if one of the species is to be sympathetically cooled by the other, one typically wants to have many atoms acting as the cooling agent and fewer atoms to be sympathetically cooled (and it does not matter if the temperature of these few atoms is larger in the beginning as long as their contribution to the total energy is small). Therefore one might benefit from choosing a current ratio which minimizes the loss and heating of the cooling agent while keeping the loss and temperature increase of the other species at an acceptable level.

3.7 An alternative mixing scheme

In the group of Simon Cornish at Durham University in England they are studying ultracold mixtures of Rb and Cs. They are currently building up an additional experimental facility for this purpose where they have also

considered to mix Rb and Cs by merging two quadrupole traps. They have proposed an interesting mixing scheme that is different from the one introduced here. I have made several calculations on this alternative scheme. For simplicity I have assumed that the atoms in both traps are ^{87}Rb in the stretched state $|F = 2, m_F = 2\rangle$ (referring to the discussion in Sec. 3.6, I expect it to lead to a minor correction when Rb is exchanged with Cs in one of the traps).

The setup consists of two identical quadrupole traps, Trap 1 and Trap 2, placed symmetrically at each side of a third trap, Trap 3. The coil parameters for the setup are given in Tab. 3.2 and the setup is sketched in Fig. 3.18. When there is no current in the coils of Trap 3 it is possible to have two separate atomic clouds in Trap 1 and 2. The idea is then to carry out the mixing process by ramping down the current in Trap 1 and 2 to zero while ramping up the current in Trap 3 to eventually obtain a mixed cloud trapped in Trap 3 (without moving any of the coils).

Table 3.2: Circular coil pair parameters.

Coil	Trap 1	Trap 2	Trap 3
Position of coil axis, x (cm)	-4.35	4.35	0.
A (cm)	2.85	2.85	4.26
R (cm)	2.95	2.95	5.36
I (A)	12.	12.	24.

If the currents are ramped linearly during 5 s the calculation of the magnetic field gives the potential energy isosurfaces shown in Fig. 3.19. Judging from these isosurfaces, the process should work just as well with this alternative setup as for our setup. But, as we have seen, the atoms are not in thermal equilibrium during the mixing process and it is hard to conclude anything about the heating during the process from the shape of the isosurfaces.

Unfortunately the results of the numerical simulations of particle trajectories are not so promising for this setup. If the currents in Trap 1 and 2 are ramped down linearly to 0 while the current in Trap 3 is ramped up linearly during 5 s, I get the results shown in Fig. 3.20 when the initial current in Trap 2 is varied. As expected, the atoms in Trap 1 are favored when the initial current is higher in Trap 1 than in Trap 2 and vice versa, but at the point where the initial current in Trap 2 equals the initial current in Trap 1 (150 A) the final phase space density of the mixed cloud is only 4 % of the value for each the initial clouds (in contrast to the 27 % in Sec. 3.5.1). Apparently there is no ratio of initial currents that does not lead to a dramatic loss of phase space density for one of the clouds. If the goal is to apply sympathetic, evaporative cooling of a Rb/Cs mixture with Rb as the cooling agent, the best thing one can do is probably to favor the trap with

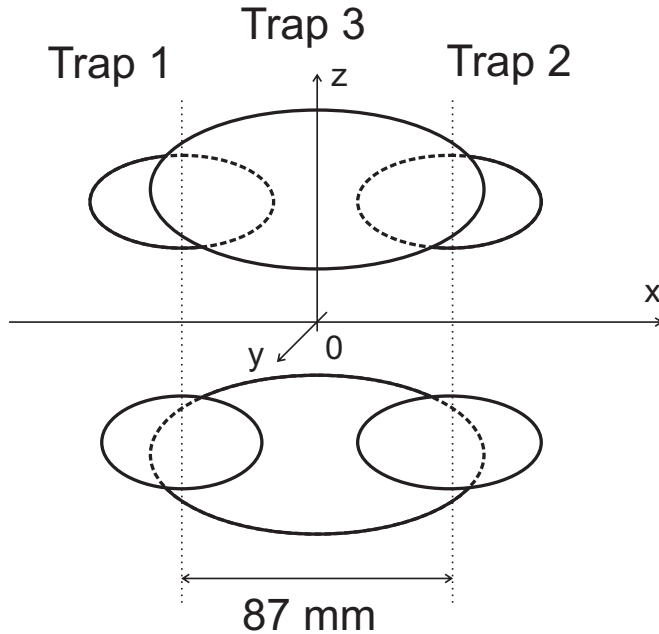


Figure 3.18: Sketch of the alternative mixing setup described in Sec. 3.7.

Rb slightly over the trap with Cs. For instance if one has Cs in Trap 1 and Rb in Trap 2, we can see from Fig. 3.20 that an initial current of 200 A in Trap 2 gives a phase space density fraction of about 17 % for Rb and 2 % for Cs.

The symmetry of the alternative mixing configuration is appealing, but unfortunately it seems like it is also its main flaw. The problem is that the magnetic fields from Trap 1 and 2 interfere destructively in the middle. This means that the field gradients in the mixing region are small such that the atomic cloud expands too much during the process. This expansion eventually leads to heating. So the symmetry is, in fact, undesirable. This is also reflected in the fact that the phase space density in Fig. 3.20 has a *minimum* and not a maximum when the initial currents in Trap 1 and 2 are identical.

It is natural to suspect that the results might be improved if the mixing is carried out faster or slower. However, this does not seem to be the case (see Fig. 3.21). It is interesting to note that it is not advantageous to carry out the mixing process as slow as possible (the relative phase space density decreases as the mixing time is increased above about 3 s). In order to understand this, apparently anti-intuitive, fact it is important to remember that the mixing process is, and has to be, a non-equilibrium process. One does not want the atoms to thermalize in the intermediate stages of the

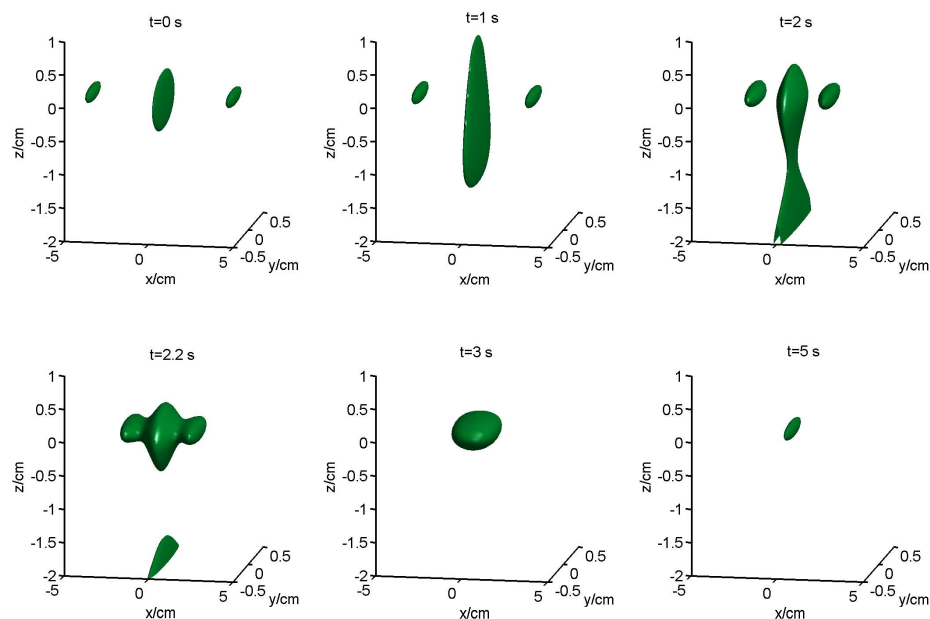


Figure 3.19: Selection of potential energy isosurfaces during the mixing process for the alternative mixing setup. The current in the coils of Trap 1 and 2 a ramped down linearly from 267 A to 0 A while the current in Trap 3 is simultaneously ramped up from 0 A to 324 A in 5 s. These currents correspond to an initial, radial gradient of 125 G/cm in Trap 1 and 2 and a final radial gradient of 125 G/cm in Trap 3. Gravity is included assuming that $g_F m_F = 1$. The surfaces correspond to a potential energy of $k \times 2$ mK for atoms with $g_F m_F = 1$. At a temperature of 400 μ K 65 % of the atoms would stay inside these isosurfaces in thermal equilibrium.

process where the trapping potential is very weakly confining.

I have tried to play around with the values of the initial and final currents, the ramps and the geometrical parameters in the setup, but unfortunately without any significant improvement. I have also tried to add extra radial confinement using Ioffe bars in the mixing direction (4 straight wires in a square configuration with opposite currents in the neighboring wires). It *is* possible to add extra radial confinement with such a configuration provided that the right direction of the current in the Ioffe bars is chosen. However, it does not change the confinement along the mixing direction and I have not been able to achieve less heating with such a configuration.

3.8 Conclusion

In conclusion, I have demonstrated a new method to make mixtures of magnetically trapped, ultracold atoms based on merging of simple magnetic

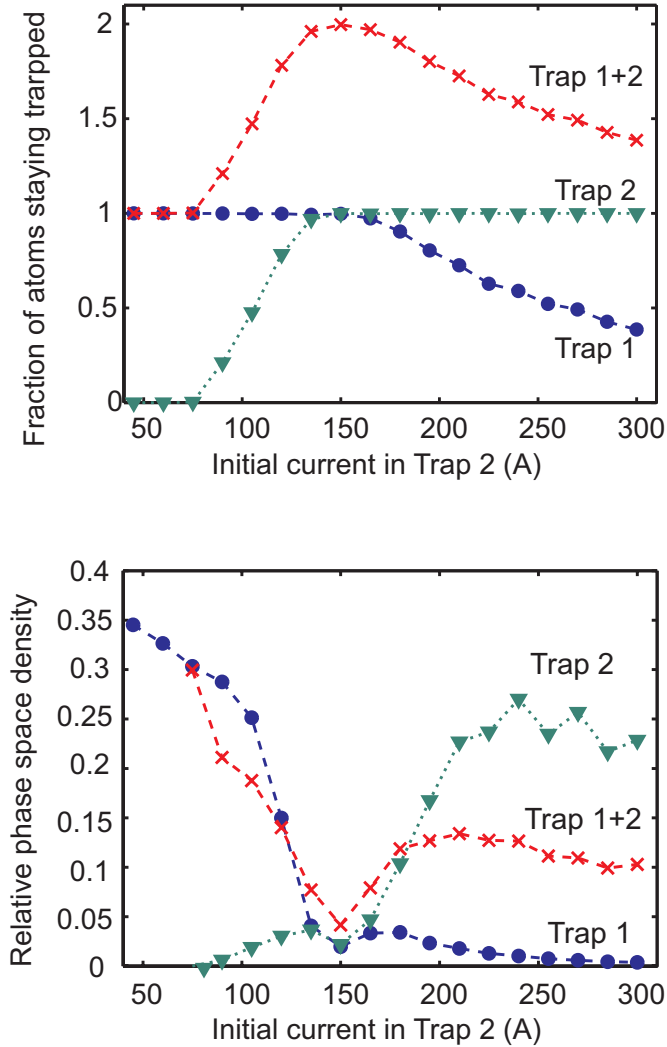


Figure 3.20: Results of numerical simulations of the alternative mixing scheme with linear current ramps. The currents in Trap 1 and 2 are ramped down to 0 A during 5 s and the current in Trap 3 is simultaneously ramped up from 0 A to 190 A. The initial current in Trap 2 is varied while the initial current in Trap 1 is kept at 150 A. The initial temperature of the cloud in Trap 1 is $272 \mu\text{K}$ and the radial field gradient is 70 G/cm . The initial temperature of the cloud in Trap 2 is chosen such that the phase space density is the same as for the cloud in Trap 1. The upper plot shows the number of atoms staying trapped while the lower plot shows the final phase space density relative to the initial phase space density of the atomic cloud in Trap 1. Compare to Fig. 3.13 (a) and (c).

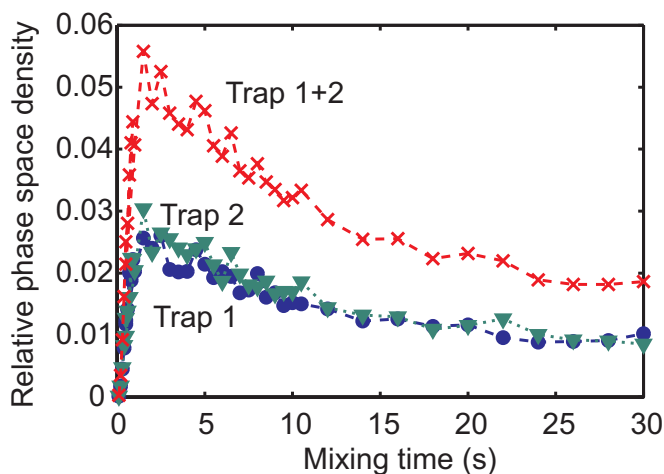


Figure 3.21: Results of varying the mixing speed in the alternative mixing scheme by changing the duration of the linear current ramps. The initial current in Trap 1 and 2 is 150 A, the final current in Trap 3 is 190 A. The other parameters are as in Fig. 3.20.

In the region $0.2 \text{ s} \leq t \leq 20 \text{ s}$ the loss of atoms is less than 5 %.

quadrupole traps mounted on industrial translation stages. This method should be generally applicable provided that the trap gradients and the diameter of the vacuum chamber tube in the mixing region are large enough. However, the investigations of an alternative mixing scheme using a symmetric configuration of three stationary coils show that the exact way of carrying out the process is important.

The experimental results show that two clouds of Rb atoms can be mixed with only about 5 % loss of atoms, and with a final phase space density that is 32 % of the initial phase space density of each cloud. This loss of phase space density is so small that it should be possible to cool the mixed cloud down to quantum degeneracy.

The experimental results are in good agreement with simple classical simulations of the mixing process. Extending these simulations to mixtures of different elements, I get promising results for mixing of different species and I believe that the method could become a useful new way of producing ultracold mixtures of some elements.

Chapter 4

Two interacting atoms in an optical lattice well

Essential parts of Sec. 4.1.2-4.3 have been submitted for publication, see Arxiv reference [3].

In this section we will be concerned with a theoretical model for the application of an s-wave Feshbach resonance to two interacting atoms in an optical lattice well in the harmonic approximation. This will be the basis for the dynamical calculations on the resonant creation of molecules in chapter 5. While the homonuclear case has also been investigated intensively by others [132–138], the nontrivial heteronuclear case had not been treated theoretically when I started my work on it. Lately, however, calculations of the energies of the two lowest states in the heteronuclear case have been presented in [139].

4.1 Two interacting atoms in a harmonic potential

Motivated by the discussion in Sec. 1.3.2 I stick to the model of two interacting atoms in a harmonic potential. Even this problem is much more complicated than one would guess. As long as there is no outer, confining potential the problem of two interacting particles separates trivially into uncoupled center-of-mass (CM) and relative dynamics. But when an outer potential is added the complexity of the problem increases dramatically and it is generally impossible to obtain analytic solutions (just think of the helium atom).

Let us introduce the CM (\mathbf{R}) and relative (\mathbf{r}) coordinates

$$\mathbf{R} = \frac{m_1 \mathbf{r}_1 + m_2 \mathbf{r}_2}{m_1 + m_2} \quad \mathbf{r} = \mathbf{r}_1 - \mathbf{r}_2. \quad (4.1)$$

For a harmonic confining potential and a general interaction $V_{\text{int}}(\mathbf{r})$ depend-

ing on the relative separation $\mathbf{r} \equiv \mathbf{r}_1 - \mathbf{r}_2$ the Hamiltonian is

$$H = -\frac{\hbar^2}{2m_1}\nabla_1^2 - \frac{\hbar^2}{2m_2}\nabla_2^2 + \frac{1}{2}m_1\omega_1^2r_1^2 + \frac{1}{2}m_2\omega_2^2r_2^2 + V_{\text{int}}(\mathbf{r}). \quad (4.2)$$

Since the interaction acts on the relative coordinate, we want to separate the Hamiltonian into a part acting only on the relative coordinate and a part acting only on the CM coordinate. The kinetic energy can always be separated like that, but the sum of the two harmonic potentials cannot in general. See appendix B for a further discussion of this issue.

I will now separately treat the case $\omega_1 = \omega_2$ where the Hamiltonian can easily be separated so the relative and CM motions are uncoupled (referred to as “the separating case” in the following) and the general case where ω_1 and ω_2 might be different (referred to as “the non-separating case” in the following).

4.1.1 The Separating Case

Let us look at the harmonic part of the potential in (4.2):

$$\frac{1}{2}m_1\omega_1^2r_1^2 + \frac{1}{2}m_2\omega_2^2r_2^2. \quad (4.3)$$

It is a great feature of the harmonic potential that this sum of two harmonic potentials separates into harmonic potentials in the relative and CM coordinates provided that $\omega_1 = \omega_2 \equiv \omega$ (which is clearly the case if the two atoms in the lattice well are identical and in the same hyperfine state):

$$V(\mathbf{r}_1, \mathbf{r}_2) = \frac{1}{2}\omega^2 (m_1r_1^2 + m_2r_2^2) \quad (4.4)$$

$$= \frac{1}{2}\omega^2 \frac{1}{M} ((m_1^2 + m_1m_2)r_1^2 + (m_2^2 + m_1m_2)r_2^2) \quad (4.5)$$

$$= \frac{1}{2}\omega^2 \frac{1}{M} ((m_1\mathbf{r}_1 + m_2\mathbf{r}_2)^2 + m_1m_2(\mathbf{r}_1 - \mathbf{r}_2)^2) \quad (4.6)$$

$$= \frac{1}{2}\omega^2 \left(M \left(\frac{m_1\mathbf{r}_1 + m_2\mathbf{r}_2}{M} \right)^2 + \mu (\mathbf{r}_1 - \mathbf{r}_2)^2 \right) \quad (4.7)$$

$$= \frac{1}{2}M\omega^2 R^2 + \frac{1}{2}\mu\omega^2 r^2 \quad (4.8)$$

where $M = m_1 + m_2$ is the total mass and $\mu = m_1m_2/M$ is the reduced mass. So we have a complete separation of the Hamiltonian: $H(\mathbf{r}_1, \mathbf{r}_2) = H_{\text{CM}}(\mathbf{R}) + H_{\text{rel}}(\mathbf{r})$ where

$$H_{\text{CM}}(\mathbf{R}) = -\frac{\hbar^2}{2M}\nabla_{\mathbf{R}}^2 + \frac{1}{2}M\omega^2 R^2 \quad (4.9)$$

$$H_{\text{rel}}(\mathbf{r}) = -\frac{\hbar^2}{2\mu}\nabla_{\mathbf{r}}^2 + \frac{1}{2}\mu\omega^2 r^2 + V_{\text{int}}(\mathbf{r}). \quad (4.10)$$

The CM motion corresponds to the motion of a single particle in a harmonic oscillator. The relative motion corresponds to the motion of a single particle in a harmonic oscillator modified by the interaction.

4.1.2 The Non-separating Case

If $\omega_1 \neq \omega_2$, the harmonic potential does not separate into relative and CM parts (see Appendix B). One may then choose between two different approaches to solve the Schrödinger equation. One possibility is to diagonalize the interaction in a product basis consisting of the harmonic oscillator wave functions in \mathbf{r}_1 and \mathbf{r}_2 . That is problematic for two reasons: First, the effective interaction between two ultracold atoms is quite strong in the vicinity of a Feshbach resonance and second, the pseudopotential which I introduce in section 4.2 and use for the interaction has irregular eigenstates and is therefore not suited for a perturbative treatment in a basis of regular wave functions. Therefore I have chosen the other approach which is to stick to the CM and relative coordinates and diagonalize the coupling between them in a product basis of uncoupled CM and relative motion wave functions.

It is shown in Appendix B that we can write the total Hamiltonian as:

$$H(\mathbf{R}, \mathbf{r}) = H_{\text{cm}}(\mathbf{R}) + H_{\text{rel}}(\mathbf{r}) + C \mathbf{R} \cdot \mathbf{r} \quad (4.11)$$

where, assuming that the interaction $V_{\text{int}}(\mathbf{r})$ is central,

$$H_{\text{cm}}(\mathbf{R}) = \frac{-\hbar^2}{2M} \nabla_{\mathbf{R}}^2 + \underbrace{\frac{1}{2} M \Omega^2 R^2}_{V_{\text{CM}}(R)} \quad (4.12)$$

$$H_{\text{rel}}(\mathbf{r}) = \frac{-\hbar^2}{2\mu} \nabla_{\mathbf{r}}^2 + \underbrace{\frac{1}{2} \mu \omega^2 r^2 + V_{\text{int}}(r)}_{V_{\text{rel}}(r)}. \quad (4.13)$$

If we define the mass ratio $\alpha = m_2/m_1$ and the ratio of the harmonic oscillator depths $\beta = (m_2\omega_2^2)/(m_1\omega_1^2)$, the frequencies Ω and ω and the coupling coefficient C are uniquely determined by the following formulas (see Appendix B):

$$\frac{\Omega}{\omega_1} = \sqrt{\frac{1+\beta}{1+\alpha}} \quad (4.14)$$

$$\frac{\omega}{\omega_1} = \sqrt{\frac{\alpha + \beta/\alpha}{1+\alpha}} \quad (4.15)$$

$$\frac{C}{m_1\omega_1^2} = \frac{\alpha - \beta}{1+\alpha} \quad (4.16)$$

However, for the rest of this section I want to play down the particular form of V_{CM} and V_{rel} in (4.12) and (4.13) to emphasize the fundamental nature

of the problem. The coupling between the CM and the relative dynamics makes the non-separating case an interesting physical system which is remarkably different from the separating case. The coupling also makes the system considerably more difficult to treat, because we need to consider a much larger Hilbert space of wave functions and angular momentum must be taken into account.

Our aim is to diagonalize H in the uncoupled basis of CM and relative motion wave functions that we get when $C = 0$:

$$\psi_{NLMnlm}(\mathbf{R}, \mathbf{r}) = \Phi_{NLM}(\mathbf{R})\varphi_{nlm}(\mathbf{r}) \quad (4.17)$$

where N , respectively n , are the principal quantum numbers and L and M , respectively l and m , are the angular momentum quantum numbers of the CM and relative motion respectively. We introduce the angular momentum operators of the CM and relative dynamics as

$$\mathbf{L} = \mathbf{R} \times \mathbf{P} \quad \mathbf{l} = \mathbf{r} \times \mathbf{p} \quad (4.18)$$

where $\mathbf{P} = -i\hbar\nabla_{\mathbf{R}}$ and $\mathbf{p} = -i\hbar\nabla_{\mathbf{r}}$ are the conjugated momentum operators of the CM and relative coordinates. Furthermore, we introduce the total angular momentum as

$$\mathbf{J} = \mathbf{L} + \mathbf{l} \quad (4.19)$$

Even if we do not make use of it in the following, it is interesting to note that if we define $\mathbf{p}_1 = -i\hbar\nabla_{\mathbf{r}_1}$, $\mathbf{p}_2 = -i\hbar\nabla_{\mathbf{r}_2}$, $\mathbf{l}_1 = \mathbf{r}_1 \times \mathbf{p}_1$, and $\mathbf{l}_2 = \mathbf{r}_2 \times \mathbf{p}_2$ we also have $\mathbf{J} = \mathbf{l}_1 + \mathbf{l}_2$.¹

Since both H_{CM} , H_{rel} and $\mathbf{R} \cdot \mathbf{r}$ are rotationally invariant, we have

¹This follows from the fact that

$$\mathbf{P} = \mathbf{p}_1 + \mathbf{p}_2 \quad \text{and} \quad \mathbf{p} = \mu \left(\frac{\mathbf{p}_1}{m_1} - \frac{\mathbf{p}_2}{m_2} \right) \quad (4.20)$$

as in classical mechanics, so

$$\begin{aligned} & \mathbf{R} \times \mathbf{P} + \mathbf{r} \times \mathbf{p} \\ &= \mu \left(\frac{\mathbf{r}_1}{m_2} + \frac{\mathbf{r}_2}{m_1} \right) \times (\mathbf{p}_1 + \mathbf{p}_2) + (\mathbf{r}_1 - \mathbf{r}_2) \times \mu \left(\frac{\mathbf{p}_1}{m_1} - \frac{\mathbf{p}_2}{m_2} \right) \\ &= \mathbf{r}_1 \times \mathbf{p}_1 + \mathbf{r}_2 \times \mathbf{p}_2 = \mathbf{l}_1 + \mathbf{l}_2 \end{aligned} \quad (4.21)$$

To show (4.20) simply amounts to use

$$\mathbf{r}_1 = \mathbf{R} + \frac{\mu}{m_1}\mathbf{r} \quad \mathbf{r}_2 = \mathbf{R} - \frac{\mu}{m_2}\mathbf{r} \quad (4.22)$$

and apply the chain rule of differentiation to $\nabla_{\mathbf{R}}$ and $\nabla_{\mathbf{r}}$.

$[H, \mathbf{J}] = 0$ (that might also be shown using standard commutator algebra²). Therefore our Hilbert space separates into independent subspaces belonging to different values of J and m_J which makes it natural to switch from the $|NLMnlm\rangle$ basis to the $|Jm_JNLnl\rangle$ basis:

$$\psi_{Nlnl}^{Jm_J} = \sum_{Mm} \langle LMlm|Jm_J\rangle \Phi_{NLM}(\mathbf{R}) \varphi_{nlm}(\mathbf{r}) \quad (4.23)$$

where $\langle LMlm|Jm_J\rangle$ denotes the Clebsch-Gordan coefficients. It should be stressed, however, that $\mathbf{R} \cdot \mathbf{r}$ does *not* commute with \mathbf{L}^2 and \mathbf{I}^2 (see footnote³) so L and l are not good quantum numbers when the coupling term is included into the Hamiltonian. This is in contrast to e.g. the $\mathbf{L} \cdot \mathbf{S}$ (spin-orbit) coupling in the hydrogen atom which commutes with L^2 and S^2 leaving L and S as good quantum numbers.

We want to diagonalize the $\mathbf{R} \cdot \mathbf{r}$ coupling term in the basis (4.23). For this, we need the following matrix elements:

$$\begin{aligned} \langle \psi_{N'L'n'l'}^{Jm_J} | \mathbf{R} \cdot \mathbf{r} | \psi_{Nlnl}^{Jm_J} \rangle &= \sum_{M'm'Mm} \langle L'M'l'm'|Jm_J\rangle \langle LMlm|Jm_J\rangle \\ &\times \langle \Phi_{N'L'M'}(\mathbf{R}) \varphi_{n'l'm'}(\mathbf{r}) | \mathbf{R} \cdot \mathbf{r} | \Phi_{NLM}(\mathbf{R}) \varphi_{nlm}(\mathbf{r}) \rangle \end{aligned} \quad (4.24)$$

where

$$\begin{aligned} &\langle \Phi_{N'L'M'}(\mathbf{R}) \varphi_{n'l'm'}(\mathbf{r}) | \mathbf{R} \cdot \mathbf{r} | \Phi_{NLM}(\mathbf{R}) \varphi_{nlm}(\mathbf{r}) \rangle \\ &= \sum_{i=x,y,z} \int \Phi_{N'L'M'}(\mathbf{R}) R_i \Phi_{NLM}(\mathbf{R}) d^3\mathbf{R} \int \varphi_{n'l'm'}(\mathbf{r}) r_i \varphi_{nlm}(\mathbf{r}) d^3\mathbf{r} \\ &= \langle \Phi_{N'L'M'}(\mathbf{R}) | \mathbf{R} | \Phi_{NLM}(\mathbf{R}) \rangle_{\mathbf{R}} \cdot \langle \varphi_{n'l'm'}(\mathbf{r}) | \mathbf{r} | \varphi_{nlm}(\mathbf{r}) \rangle_{\mathbf{r}} \end{aligned} \quad (4.25)$$

where $\langle \cdot \rangle_{\mathbf{R}}$ and $\langle \cdot \rangle_{\mathbf{r}}$ denote integration with respect to \mathbf{R} and \mathbf{r} .

So the problem boils down to determining dipole matrix elements between wave functions of a spherically symmetric potential and the angular part of the dipole matrix elements does not depend on what the spherically symmetric potential looks like. From e.g. the theory of radiative dipole transitions in the hydrogen atom we know that they are governed by the selection rules $|L' - L| = 1$ and $|M - M'| \leq 1$ (see Appendix C.1) which significantly reduces the task of computing the coupling matrix. We note

²For instance using Cartesian coordinates $\mathbf{R} = (X, Y, Z)$ and $\mathbf{r} = (x, y, z)$ we have $[\mathbf{R} \cdot \mathbf{r}, J_z] = [Xx + Yy + Zz, L_z + l_z] = [Xx + Yy, XP_y - YP_x + xp_y - yp_x] = [Xx, -YP_x - yp_x] + [Yy, XP_y + xp_y] = -Y[X, P_x]x - Xy[x, p_x] + X[Y, P_y]y + Yx[y, p_y] = i\hbar(-Yx - Xy + Xy + Yx) = 0$.

³For instance using Cartesian coordinates $\mathbf{R} = (X, Y, Z)$, $\mathbf{r} = (x, y, z)$ and the constant function $f(\mathbf{R}, \mathbf{r}) = 1$ as a trial function we have $(\mathbf{R} \cdot \mathbf{r})\mathbf{L}^2 f = 0$, but $L^2(\mathbf{R} \cdot \mathbf{r})f = L_x^2(Yy + Zz) + L_y^2(Xx + Zz) + L_z^2(Xx + Yy) = -i\hbar(L_x(Yz - Zy) + L_y(Zx - Xz) + L_z(Xy - Yx)) = -\hbar^2((-Yy - Zz) + (-Zz - Xx) + (-Xx - Yy)) = 2\hbar^2(Xx + Yy + Zz) \neq 0$.

also that radial part of the integrals in (4.25) can be put outside the angular momentum summation in (4.24).

When a BEC is loaded adiabatically into an optical lattice it is normally in a $J = 0$ state. Since states with given J but different m_J are degenerate, we might just look at the $J = 0, m_J = 0$ states. Such a state can only be obtained by coupling CM and relative states with $L = l$ and $M = -m$. Using the Clebsch-Gordan coefficient $\langle LMLm | J = 0, m_J = 0 \rangle = \delta_{M(-m)} (-1)^{L-M} / \sqrt{2L+1}$, where δ_{ij} is the Kronecker delta, we have

$$\psi_{NLnL}^{00}(\mathbf{R}, \mathbf{r}) = \frac{1}{\sqrt{2L+1}} \sum_{M=-L}^L (-1)^{L-M} \Phi_{NLM}(\mathbf{R}) \varphi_{nL(-M)}(\mathbf{r}) \quad (4.26)$$

and (4.24) reduces to

$$\begin{aligned} \langle \psi_{N'L'n'L'}^{00} | \mathbf{R} \cdot \mathbf{r} | \psi_{NLnL}^{00} \rangle &= \frac{(-1)^{L'+L}}{\sqrt{(2L'+1)(2L+1)}} \sum_{M'=-L'}^{L'} \sum_{M=-L}^L (-1)^{-(M+M')} \\ &\times \langle \Phi_{N'L'M'}(\mathbf{R}) \varphi_{n'L'(-M')}(\mathbf{r}) | \mathbf{R} \cdot \mathbf{r} | \Phi_{NLM}(\mathbf{R}) \varphi_{nL(-M)}(\mathbf{r}) \rangle \end{aligned} \quad (4.27)$$

We note again that the above considerations only assume that the potentials in H_{CM} and H_{rel} are spherically symmetric. Only the values of the coupling matrix elements are specific to the given potentials and the theory might be applied to any two degrees of freedom \mathbf{R} and \mathbf{r} which are confined by spherically symmetric potentials and coupled by an $\mathbf{R} \cdot \mathbf{r}$ term. In particular, it can be applied to two different interacting atoms in an optical lattice well no matter what specific interaction is used, as long as it is central.

In a real isotropic 3D optical lattice the spherical symmetry is broken to some extent, because the lattice potential is not spherical. That means that J and m_J are only approximately good quantum numbers, but I will not go into that here.

4.2 The Interaction Potential

Until now, the only thing I have assumed about the interaction is that it is central: $V_{\text{int}}(\mathbf{r}) = V_{\text{int}}(r)$. At sufficiently low temperatures two atoms only interact through s-wave scattering since the centrifugal barrier for higher partial waves becomes much larger than the thermal energies. Furthermore, the interaction depends to a large extent only on a single parameter, namely the phase shift of the potential in the low energy limit or, equivalently, the s-wave scattering length which can be found experimentally and contains all the relevant information about the potential [5].

To the extent that this is true, the interaction can be modeled by the following pseudopotential (first introduced by Huang in [140, 141] and also

described in e.g. [132, 134–136, 142]):

$$V_{\text{int}}(r) = \frac{2\pi\hbar^2 a_{\text{sc}}}{\mu} \delta^{(3)}(\mathbf{r}) \frac{\partial}{\partial r} r \quad (4.28)$$

where the action of the operator $(\partial/\partial r)r$ on a wave function ψ is to be understood as $(\partial/\partial r)(r\psi)$.

This pseudo-potential captures the essential physics in the vicinity of a Feshbach resonance surprisingly well and since it is merely a boundary condition at the origin it is much easier to deal with than the actual interatomic potential (which also, in many cases, is not even known well enough to predict the value of the scattering length, cf. the discussion in Sec. 1.4.3). It has been used several times to account for ultracold atom interactions ([132–137, 139, 142] just to mention a few references). Nevertheless, the origin of the pseudopotential is well worth a discussion, both in order to understand its advantages and shortcomings and because it seems to be a rather weird construction when you look at it.

The prefix “pseudo” is used because it should not be thought of as a true potential resembling the actual interatomic interaction. Rather it should be regarded as an operator which accounts for the phase shift of the interatomic potential and thus gives a good approximation to the spectrum and the wave functions when it is put into the Schrödinger equation in place of a potential. In particular, as we will see in Sec. 4.3.2, the pseudopotential interaction in a harmonic trap gives rise to a negative energy bound state in the repulsive case ($a_{\text{sc}} > 0$), but not in the attractive case ($a_{\text{sc}} < 0$) which is in agreement with Feshbach resonance experiments and theory.

The real interaction potential (which could for instance be approximated by a Lennard-Jones kind of potential) accommodates several bound states, no matter what the sign of the scattering length is, but here we are only concerned with the very loosely bound state which can be accessed in Feshbach resonance experiments and it is exactly this bound state which the pseudopotential accounts for.

The easiest way to justify the form of the pseudopotential in (4.28) is to consider two particles which are subject to a finite ranged interaction but which are otherwise free (I am essentially following [134]). Outside the interaction range the wave function obeys the Helmholtz equation

$$-\nabla^2\psi = k^2\psi, \quad k = \frac{\sqrt{2\mu E}}{\hbar} \quad (4.29)$$

S-wave solutions to this equation are linear combinations of zeroth order spherical Bessel and spherical Neumann functions [73, 75]:

$$\psi(\mathbf{r}) = A(j_0(kr) + Bn_0(kr)) = A\left(\frac{\sin(kr)}{kr} - B\frac{\cos(kr)}{kr}\right) = D\frac{\sin(kr + \delta_0)}{kr} \quad (4.30)$$

where A , B and D are complex constants and the real constant δ_0 is the s-wave phase shift of the interaction potential known from scattering theory. If we make a low energy expansion

$$\psi(\mathbf{r}) = A \left(1 - \frac{B}{kr} \right) + \mathcal{O}(kr) \quad (4.31)$$

we can read off the scattering length as $a = B/k$ (see Sec. 1.4.1) and we also have, $\tan \delta_0 = -B = -ka$. The goal is to construct a pseudopotential which is as simple as possible while still accounting for the phase shift of the true interaction potential - that is, a potential which reproduces the wave function (4.30) outside the range of the interaction.

We might simply use a pseudopotential $V_{\text{int}}(r)$ which gives the wave function (4.30) as a solution to the Schrödinger equation for *all* r . Suppose that we set $V_{\text{int}}(r) = 0$. Then the wave function could be written in the form (4.30) for all r , but we would be forced to set $B = 0$, because the spherical Neumann function $n_0(r)$ is irregular at $r = 0$ inconsistent with $a \neq 0$. The problem is not a normalization problem. The source of the irregularity is that the kinetic energy operator creates a singularity when it acts on the $1/r$ function:

$$\nabla^2 \frac{1}{r} = -4\pi \delta^{(3)}(\mathbf{r}) \quad (4.32)$$

But this singularity is removed if we use

$$V_{\text{int}}(r) = \frac{2\pi\hbar^2(B/k)}{\mu} \delta^{(3)}(\mathbf{r}) \frac{\partial}{\partial r} r \quad (4.33)$$

instead. If we let the Hamilton operator with the pseudopotential (4.33) act on the wave function (4.30) we get

$$\begin{aligned} H\psi &= \frac{-\hbar^2}{2\mu} \nabla^2 \psi + \frac{2\pi\hbar^2(B/k)}{\mu} \delta^{(3)}(\mathbf{r}) \frac{\partial}{\partial r} (r\psi) \\ &= \frac{\hbar^2}{2\mu} \left(k^2 \psi - 4\pi A(B/k) \delta^{(3)}(\mathbf{r}) \right) + \frac{2\pi\hbar^2(B/k)}{\mu} \delta^{(3)}(\mathbf{r}) \underbrace{\frac{\partial}{\partial r} (r\psi) \Big|_{r=0}}_{=A} \\ &= \underbrace{\frac{\hbar^2 k^2}{2\mu}}_{=E} \psi \end{aligned} \quad (4.34)$$

so the wave function (4.30) is a solution to the Schrödinger equation with the pseudopotential (4.33) all the way to $r = 0$. Remembering that $B/k = a$ we get the pseudopotential (4.28). A similar analysis can be carried out for higher partial waves. Accounts of this can be found in [140, 141, 143], but it

is beyond the scope of this thesis since I will focus on the case when s-wave scattering is dominant.

If the particles are trapped in a harmonic potential (in addition to the interaction) we might still express the wave function outside the interaction range as a sum of a regular and an irregular wave functions which are given in terms of confluent hypergeometric functions (see [133] for explicit functional forms). For small r , the wave function will still be of the form

$$\psi(\mathbf{r}) \simeq A(E_n) \left(1 + \frac{B(E_n)}{r} \right) + \mathcal{O}(r^1) \quad (4.35)$$

with constants A and B depending on the discrete energy E_n . The irregularity at $r = 0$ can still be removed by a pseudopotential similar to (4.33), but since the constants now depend on the (at this point unknown) discrete energy, there will be correction terms to the pseudopotential. A thorough analysis for a hard-sphere interaction has been carried out by Block and Holthaus in [134].

In perturbative many-body applications the regularization factor $(\partial/\partial r)r$ is often omitted from the pseudopotential because it is redundant in a Hilbert space of wave functions which are finite and have a finite derivative at the origin since

$$\left. \frac{\partial}{\partial r}(r\psi(\mathbf{r})) \right|_{\mathbf{r}=\mathbf{0}} = \left(\psi(\mathbf{r}) + r \frac{\partial \psi(\mathbf{r})}{\partial r} \right) \Big|_{\mathbf{r}=\mathbf{0}} = \psi(\mathbf{0}), \text{ if } |\psi(\mathbf{0})|, \left| \frac{\partial \psi(\mathbf{r})}{\partial r} \right|_{\mathbf{r}=\mathbf{0}} < \infty \quad (4.36)$$

But what we need here is an exact diagonalization of the Hamiltonian in order to account for the molecular, negative energy bound state and for that we need to keep the irregular wave functions in our Hilbert space.

One might guess that the validity of the pseudopotential approximation is connected to the validity of the inequality $a_{sc}/a_{ho} \ll 1$ where a_{ho} is the length scale of the harmonic confining potential. That would be the case for a hard-sphere interaction [134]. But it turns out that for realistic interatomic potentials containing a long range van der Waals ($V(r) = -C_6/r^6$) attraction, it is rather the ratio β_6/a_{ho} , where $\beta_6 = (2\mu C_6/\hbar^2)^{1/4}$ is a characteristic length scale of the van der Waals attraction, that is important, see [135, 137]. This is fortunate since close to a Feshbach resonance, where the scattering length diverges, the ratio a_{sc}/a_{ho} easily gets larger than 1 for two atoms in an optical lattice well. Values of C_6 for both homonuclear and heteronuclear alkali metal atom pairs can be found in [144]. For Rb-Rb $C_6 = 4691 a_0$ which gives $\beta_6 = 164 a_0$ for ^{85}Rb and $\beta_6 = 165 a_0$ for ^{87}Rb . In the case of an optical lattice well with a trapping frequency of $\omega = 2\pi \times 30$ kHz we have $a_{ho} = 1.7 \times 10^3 a_0$ so $\beta_6/a_{ho} = 0.1$ for two Rb atoms. According to [135], deviations of about 4 % from the exact spectra must be expected

at this ratio when we use the pseudopotential approximation. For Rb/Li [144] gives $C_6 = 2545 a_0$ so $\beta_6 = 85 a_0$ for $^{87}\text{Rb}/^6\text{Li}$, so also in this system we expect the pseudopotential approximation to be reasonably good.

Accounts for calculations of spectra in models with more accurate potentials can be found in [135, 136, 138]. Also, pseudopotential models with an energy dependent scattering length $a(E) = -\tan(\delta_0(k))/k$, can be used to improve the accuracy [135, 137]. Here, however, I will stick to the analytically attractive pseudopotential approximation using the zero energy limit of the scattering length. While the exact spectra and matrix elements might be slightly different due to the limitations of this approximation, the pseudopotential captures the essential physics quite well and it gives good quantitative agreement in most cases. Also, the dynamical equations derived in chapter 5 assume no specific form of the interaction and are therefore generally valid.

4.3 The spectrum and the wave functions

In this section we obtain solutions to the Schrödinger equation of the relative motion with the Hamiltonian (4.10) and the pseudopotential (4.28). I will first state the solution in the case of no interaction $V_{\text{int}}(r) = 0$ and no coupling to the CM motion ($C = 0$) in section 4.3.1. After that I will treat the separating case where there is an interaction but where C is still zero in section 4.3.2 and at last I treat the general non-separating case in section 4.3.3.

4.3.1 The isotropic harmonic oscillator without interactions

Since the isotropic harmonic oscillator is separable in Cartesian coordinates, we know that the wave functions are products of a polynomial and a Gaussian and the energies are of the form $E = \hbar\omega(n' + 3/2)$ where n' is an integer. But since the interaction potential is spherically symmetric we want to use spherical coordinates instead. Solving the three-dimensional isotropic harmonic oscillator in spherical coordinates leads to the spectrum

$$E = \hbar\omega \left(2n + l + \frac{3}{2} \right) \quad (4.37)$$

where $n = 0, 1, 2, \dots$ is the number of nodes in the radial wave function and $l = 0, 1, 2, \dots$ is the angular momentum quantum number. Notice that states with the same value of $2n + l$ are degenerate. The wave functions can be written in terms of generalized Laguerre polynomials L_n^α (the wave function is e.g. given in [145]⁴ and the normalization is found in Appendix

⁴In [145] the solution is written in terms of the confluent hypergeometric function ${}_1F_1(-n, l + 3/2, r^2)$ which is proportional to $L_n^{l+1/2}(r^2)$ when n is a non-negative integer ([146] formula 13.6.9).

C.3, see also [77] Ch. XII for a discussion of the solution):

$$\psi_{nlm}(\mathbf{r}) = \sqrt{\frac{2n!}{\Gamma(n+l+3/2)}} L_n^{l+1/2}(r^2) r^l e^{-r^2/2} Y_{lm}(\theta, \phi) \quad (4.38)$$

where m is the angular momentum projection, Y_{lm} are the spherical harmonics and Γ is the gamma function. The unit of length is $\sqrt{\hbar/(\mu\omega)}$.

4.3.2 The Separating Case

In the case $l > 0$ the pseudopotential (4.28) does not alter the solutions since it only acts on s-wave functions [132]. The solution to the $l = 0$ problem was obtained in [132] and in [133] by another approach. The one-dimensional case has also been solved even earlier in [147] by a brute force “look up the solution” method and I will use a similar approach to readily obtain the solutions.

In the region $r > 0$ the radial Schrödinger equation with the Hamiltonian (4.10) is just the Schrödinger equation for the isotropic harmonic oscillator. Expressed in units of the harmonic oscillator length scale

$$a_{\text{ho}} = \sqrt{\frac{\hbar}{\mu\omega}} \quad (4.39)$$

and energy scale $E = \hbar\omega\epsilon$, it reads

$$-\frac{1}{2} \frac{\partial^2 u}{\partial r^2} + \frac{1}{2} r^2 u = \epsilon u \quad (4.40)$$

or

$$\frac{\partial^2 u}{\partial(\sqrt{2}r)^2} - \left(\frac{1}{4} (\sqrt{2}r)^2 - \epsilon \right) u = 0 \quad (4.41)$$

where $u(r) = r\psi(r)$ is the reduced wave function. Solutions to this equation are called parabolic cylinder functions. According to [146] formulas 19.3.7 and 19.3.8 there exists two linearly independent solutions $D_{\epsilon-1/2}(\sqrt{2}r)$ and $V(-\epsilon, \sqrt{2}r)$ with the following asymptotic behaviour for large r ([146] 19.8.1 and 19.8.2):

$$D_{\epsilon-1/2}(\sqrt{2}r) \simeq e^{-r^2/2} (\sqrt{2}r)^{\epsilon-1/2}, \quad V(-\epsilon, \sqrt{2}r) \simeq \sqrt{\frac{2}{\pi}} e^{r^2/2} (\sqrt{2}r)^{-\epsilon-1/2}. \quad (4.42)$$

Clearly the V function cannot be normalized and must be discarded so all solutions must be of the form $D_{\epsilon-1/2}(\sqrt{2}r)$. This function satisfies (see [146]

formulas 19.3.5 and 19.3.7)

$$D_{\epsilon-1/2}(0) = \frac{\sqrt{\pi}}{2^{-\epsilon/2+1/4}\Gamma(-\epsilon/2+3/4)} \quad (4.43)$$

$$D'_{\epsilon-1/2}(0) = \frac{-\sqrt{\pi}}{2^{-\epsilon/2-1/4}\Gamma(-\epsilon/2+1/4)}. \quad (4.44)$$

Normally we would only accept the regular solutions with $u(0) = 0$. That is only possible if the Γ function in (4.43) is infinite, that is the argument has to be a non-positive integer, or $\epsilon = 2n + 3/2$ where $n = 0, 1, 2, \dots$ and we get the unperturbed harmonic oscillator solutions in this case. In section 4.2, we saw that the idea of the pseudopotential is to account for the phase shift of the true interatomic potential by using irregular solutions to the unperturbed Schrödinger equation. The effect of the pseudopotential (4.28) is to impose the following boundary condition on the wave function [133]:

$$\frac{u'(0)}{u(0)} = \frac{-a_{\text{ho}}}{a_{\text{sc}}} \quad (\text{harm. osc. units}) \quad (4.45)$$

so the desired solution is $D_{\epsilon-1/2}(\sqrt{2}r)$ where the discrete energy spectrum ϵ is given as the solutions to the following transcendental equation:

$$\begin{aligned} \frac{\partial D_{\epsilon-1/2}(\sqrt{2}r)/\partial r|_{r=0}}{D_{\epsilon-1/2}(0)} &= \frac{\sqrt{2}D'_{\epsilon-1/2}(0)}{D_{\epsilon-1/2}(0)} \\ &= \frac{-2\Gamma(-\epsilon/2+3/4)}{\Gamma(-\epsilon/2+1/4)} = \frac{-a_{\text{ho}}}{a_{\text{sc}}} \quad (\text{harmonic osc. units}) \end{aligned} \quad (4.46)$$

where we have used (4.43)-(4.44). The spectrum is plotted in Fig. 4.1.

It is convenient to introduce the generalized harmonic oscillator quantum number, ν , defined by

$$\boxed{\epsilon = 2\nu + \frac{3}{2}} \quad (4.47)$$

such that $\nu = n$ in the case $a_{\text{sc}} = 0$. In terms of ν , the quantization condition (4.46) becomes

$$\boxed{\frac{2\Gamma(-\nu)}{\Gamma(-\nu-1/2)} = \frac{a_{\text{ho}}}{a_{\text{sc}}} \quad (\text{harmonic osc. units})} \quad (4.48)$$

and $u(r) = D_{2\nu+1}(\sqrt{2}r)$.

The wave function might also be rewritten in terms of the confluent hypergeometric U function ([146] 13.6.36 and 13.1.29)

$$rU\left(-\nu, \frac{3}{2}, r^2\right) e^{-r^2/2} = U\left(-\nu - \frac{1}{2}, \frac{1}{2}, r^2\right) e^{-r^2/2} = 2^{-\nu-1/2} D_{2\nu+1}(\sqrt{2}r). \quad (4.49)$$

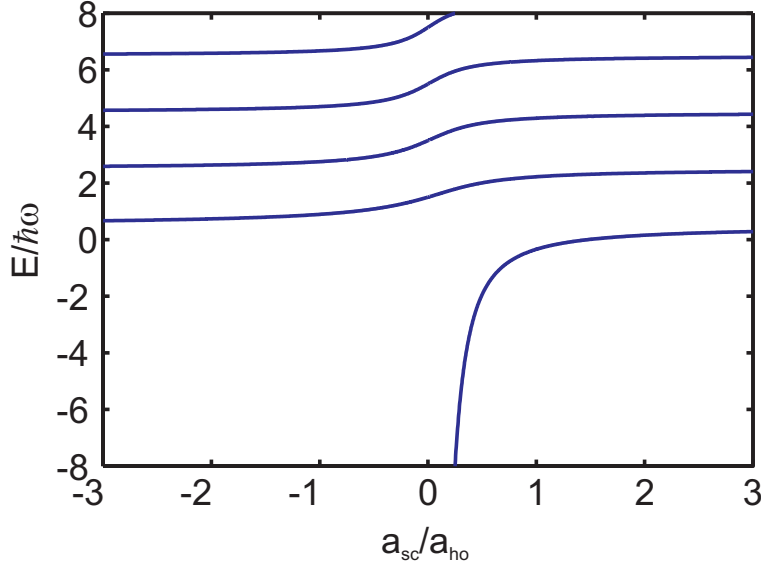


Figure 4.1: s-wave spectrum of the relative motion dynamics for two particles in an external harmonic oscillator interacting via the s-wave pseudopotential in the separating case. Notice that for $a_{sc} > 0$, the spectrum contains a bound state whose binding energy diverges when $a_{sc} \rightarrow 0_+$. In the non-interacting case ($a_{sc} = 0$) we recover the unperturbed harmonic oscillator energies $E = \hbar\omega(2n + 3/2)$, $n = 0, 1, 2, \dots$

If $\nu = n$ is a non-negative integer $U(-n, l + 3/2, x) \propto L_n^{l+1/2}(x)$ according to [146] 13.6.27 so in this case we recover the unperturbed harmonic oscillator states (4.38) as postulated above. The U function is implemented in Mathematica and in Matlab 7.0.4 it can be calculated as a special case of the generalized hypergeometric function.

Returning to the original wave function $\psi_\nu(\mathbf{r})$, we have

$$\psi_\nu(\mathbf{r}) = \frac{u_\nu(r)}{r} Y_{00} = N_\nu U\left(-\nu, \frac{3}{2}, r^2\right) e^{-r^2/2} Y_{00} \quad (4.50)$$

$$= \frac{N_\nu}{r} U\left(-\nu - \frac{1}{2}, \frac{1}{2}, r^2\right) e^{-r^2/2} Y_{00} \quad (4.51)$$

$$= \frac{N_\nu}{r} 2^{-\nu-1/2} D_{2\nu+1}(\sqrt{2}r) Y_{00} \quad (4.52)$$

where N_ν is a normalization constant ($1/N_\nu^2$ is given in Appendix C formula C.17). Notice that the Gaussian part of the wave function is absorbed into the parabolic cylinder function but not into the confluent hypergeometric function. The wave function generally diverges as $1/r$ for small r since $u(0)$ is generally finite according to (4.43). Some wave functions are shown in

Fig. 4.2.

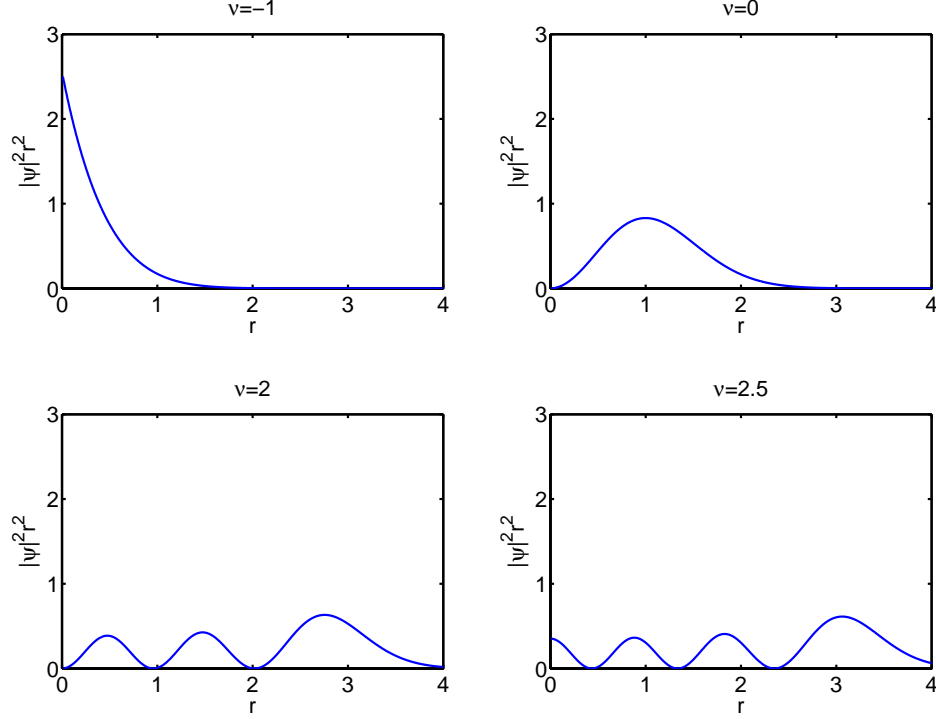


Figure 4.2: Radial probability densities for the pseudopotential wave functions. As ν decreases, the wave functions get more and more tightly bound (larger probability close to $r = 0$). States with $\nu < 0$ are true bound states whereas states with $\nu > 0$ are only bound due to the harmonic confinement. Except when ν is a non-negative integer, the probability density is nonzero at the origin because the wave function diverges as $1/r$.

The parameter which is used to tune the scattering length in experiments is the magnitude of the magnetic field B . Near a Feshbach resonance the scattering length is given by (1.26):

$$a_{\text{sc}} = a_{\text{bg}} \left(1 - \frac{\Delta}{B - B_0} \right) = a_{\text{bg}} \left(1 - \left(\frac{B - B_0}{\Delta} \right)^{-1} \right) \quad (4.53)$$

so if everything is expressed in terms of the dimensionless magnetic field $(B - B_0)/\Delta$, the only tunable parameters in the pseudopotential model are the harmonic oscillator frequency ω and the background scattering length a_{bg} (notice, however, that Δ might be negative).

In Fig. 4.3 the pseudopotential spectrum is plotted for two Rb atoms in a $\omega = 2\pi \times 30$ kHz lattice well in the case $a_{\text{bg}} = -443 a_0$ (as for the

156 G resonance in ^{85}Rb) and the case $a_{\text{bg}} = 100.5 a_0$ (as for the 1007 G resonance in ^{87}Rb). The molecular bound state exists on the $a_{\text{sc}} > 0$ side of the resonance, that is for $(B - B_0)/\Delta > 0$ in the case $a_{\text{bg}} < 0$ and for $(B - B_0)/\Delta < 0$ in the case $a_{\text{bg}} > 0$.

Notice that the cases $a_{\text{bg}} < 0$ and $a_{\text{bg}} > 0$ behave qualitatively different in the pseudopotential model because $a_{\text{sc}} \rightarrow 0$ when $(B - B_0)/\Delta \rightarrow 1$ meaning that the binding energy of the molecular state diverges according to the universal expression (1.19). On the other hand a_{sc} remains finite as $(B - B_0)/\Delta \rightarrow -1$. This is one of the shortcomings of the pseudopotential model. The physical molecular binding energy will, of course, approach a finite value as the magnetic field is moved away from the resonance on the positive scattering length side.

4.3.3 The Non-separating Case

The recipe to solve the pseudopotential model in the non-separating case was given in section 4.1.2. Our Hamiltonian is (4.11) with

$$V_{\text{CM}}(R) = \frac{1}{2}M\Omega^2 R^2 \quad (4.54)$$

$$V_{\text{rel}}(r) = \frac{1}{2}\mu\omega^2 r^2 + \frac{2\pi\hbar^2 a_{\text{sc}}}{\mu} \delta^{(3)}(\mathbf{r}) \frac{\partial}{\partial r} r. \quad (4.55)$$

Our uncoupled basis consists of the product wave functions

$$\psi_{NLM\nu lm} = \Phi_{NLM}(R)\varphi_{\nu lm}(r) \quad (4.56)$$

where Φ_{NLM} are the unperturbed Harmonic oscillator wave functions (4.38) with $\sqrt{\hbar/(M\Omega)}$ as the unit of length and $\varphi_{\nu lm}(r)$ are the wave functions of the harmonic oscillator modified by the pseudopotential with $\sqrt{\hbar/(\mu\omega)}$ as the unit of length. For $l \neq 0$, the latter states are just normal harmonic oscillator states with $\nu = n$ being a non-negative integer, whereas for $l = 0$ they are the parabolic cylinder wave functions (4.52) with ν given by (4.48). Since the total angular momentum J is conserved, we can benefit from a basis change from the $|NLM\nu lm\rangle$ basis to the $|Jm_JNL\nu l\rangle$ basis as stated in formula (4.23).

In a given Jm_J subspace the matrix representation of the Hamiltonian (4.11) in the $|NL\nu l\rangle$ basis is the sum of diagonal contributions from $H_{\text{CM}}(R)$ and $H_{\text{rel}}(r)$ and an off-diagonal contribution from the coupling term $C\mathbf{R} \cdot \mathbf{r}$

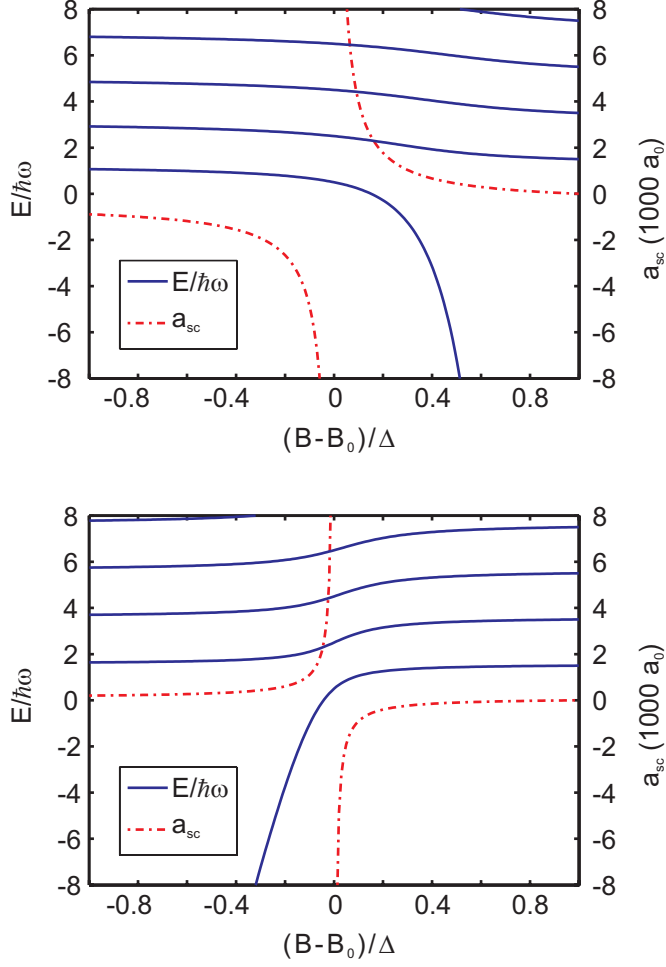


Figure 4.3: The s-wave spectrum in the pseudopotential model as a function of the magnetic field B in an $\omega = 2\pi \times 30$ kHz lattice well. The upper figure shows the case of two ^{85}Rb atoms with $a_{\text{bg}} = -443 a_0$ and the lower figure shows the case of two ^{87}Rb atoms with $a_{\text{bg}} = 100.5 a_0$. The scattering length, $a_{\text{sc}}(B)$, is also shown.

(see 4.37, 4.24 and 4.25):

$$\begin{aligned}
 H_{pq} &= \hbar\Omega(2N_p + L_p + 3/2)\delta_{pq} + \hbar\omega(2\nu_p + l_p + 3/2)\delta_{pq} \\
 &+ C \sum_{M_p m_p M_q m_q} \langle L_p M_p l_p m_p | J m_j \rangle \langle L_q M_q l_q m_q | J m_j \rangle \\
 &\times \langle \Phi_{N_p L_p M_p}(\mathbf{R}) | \mathbf{R} | \Phi_{N_q L_q M_q}(\mathbf{R}) \rangle_{\mathbf{R}} \cdot \langle \varphi_{\nu_p l_p m_p}(\mathbf{r}) | \varphi_{\nu_q l_q m_q}(\mathbf{r}) \rangle_{\mathbf{r}}
 \end{aligned} \tag{4.57}$$

where p and q are state indices.

The spectrum and the wave functions can then be found by diagonalizing this Hamiltonian matrix in Matlab. The dipole matrix elements in (4.57) can all be calculated analytically, but it requires some labor and it is therefore left for Appendix C. Here I will merely summarize the results:

The dipole integral separates into a radial factor and an angular factor. If we write the wave functions in the form $\psi'(r, \Omega) = R'(r)Y_{l'm'}(\Omega)$ and $\psi(r, \Omega) = R(r)Y_{lm}(\Omega)$ we have

$$\langle \psi' | \mathbf{r} | \psi \rangle = \int_0^\infty R'(r)^* r R(r) r^2 dr \int Y_{l'm'}(\Omega)^* \hat{\mathbf{r}} Y_{lm}(\Omega) d\Omega \quad (4.58)$$

where $\hat{\mathbf{r}}$ is the unit vector \mathbf{r}/r and (Ω) is used as short for (θ, ϕ) . We have the selection rules $|l' - l| = 1$ and $|m' - m| \leq 1$ and explicit formulas for the angular integral are given in Appendix C.1. The radial integrals are more tricky, but miraculously enough they can all be calculated analytically.

The radial dipole integral for the harmonic oscillator wave functions is given by the following simple formula, see (C.35):

$$\int_0^\infty R_{N'(L+1)}(r) r R_{NL}(r) r^2 dr = \sqrt{N+L+3/2} \delta_{N',N} - \sqrt{N} \delta_{N',N-1}. \quad (4.59)$$

Notice that we have strict selection rules on the N quantum numbers: If L increases by 1, N has to remain unchanged or to decrease by 1.

The parabolic cylinder wave functions have $l = 0$ so they couple only to $l = 1$ harmonic oscillator states. The radial dipole integral is derived in Appendix C.4. Denoting the radial parts of the wave functions by R_ν and R_n respectively we have the following formula (see C.43):

$$\begin{aligned} & \int_0^\infty R_\nu(r) r R_n(r) r^2 dr \\ &= N_\nu \sqrt{\frac{2n!}{\Gamma(n+5/2)}} \frac{\sqrt{\pi}}{16} \sum_{k=0}^n 2^{-2k} (-1)^k \binom{n+\alpha}{n-k} \frac{1}{k!} \frac{\Gamma(2k+4)}{\Gamma(k+2-\nu)}. \end{aligned} \quad (4.60)$$

Here, according to (C.17)

$$N_\nu = \sqrt{\frac{2\Gamma(-\nu-1/2)\Gamma(-\nu)}{\pi[\psi(-\nu) - \psi(-\nu-1/2)]}} \quad (4.61)$$

where ψ is the digamma function (C.18). Notice that the sum is a finite sum of a small number of terms so from a computational point of view the expression is not as ugly as it looks.

I consider ^{87}Rb and ^6Li as a specific example with a rather large mass ratio. If we take $\beta = (m_{\text{Li}}\omega_{\text{Li}}^2)/(m_{\text{Rb}}\omega_{\text{Rb}}^2) = 0.4$ (corresponding to a lattice wavelength of $\lambda = 1124$ nm, see Fig. 1.2), we have $\Omega = 1.14 \omega_{\text{Rb}}$, $\omega = 2.34 \omega_{\text{Rb}}$, and $C = -0.877 \mu\omega^2$ from (4.14)-(4.16). Taking the harmonic oscillator length scale as an estimate of the magnitude of the dipole matrix elements, we can get the following order of magnitude estimate of the energy shift of the lowest energy states caused by the coupling:

$$\frac{|\Delta E|}{\hbar\omega} \sim \frac{|C|}{\hbar\omega} \sqrt{\frac{\hbar}{M\Omega}} \sqrt{\frac{\hbar}{\mu\omega}} = \frac{|C|}{\mu\omega^2 \sqrt{(M/\mu)(\Omega/\omega)}} = 0.3 \quad (4.62)$$

so the coupling is expected to be significant but the product basis is still a good starting point. When I diagonalize the full Hamiltonian I get the $J = 0$ spectrum shown in Fig. 4.4.

An eigenfunction Ψ of the complete Hamiltonian can be written in terms of the uncoupled product wave functions

$$\Psi = \sum_{NLn} c_{NLn} \psi_{NL\nu L}^{00} \quad (4.63)$$

where (see 4.26)

$$\psi_{NL\nu L}^{00} = \frac{1}{\sqrt{2L+1}} \sum_{M=-L}^L (-1)^{L-M} \Phi_{NLM}(\mathbf{R}) \varphi_{\nu L(-M)}(\mathbf{r}) \quad (4.64)$$

and $n = 0, 1, 2, \dots$ has been used to index the radial part of the relative wave functions with increasing ν . The coefficients c_{NLn} are given by the eigenvectors of the Hamiltonian matrix. Some values of $|c_{NLn}|^2$ are given for $a_{\text{sc}} = 0$, respectively $a_{\text{sc}}/a_{\text{ho}} = 0.36$, in Tab. 4.1 and 4.2 to give an impression of the extent to which the product states mix. For a given eigenstate Ψ , I refer to the product state $|NLn\rangle$ with the largest value of $|c_{NLn}|^2$ in the expansion (4.63) as the ‘‘largest content’’ of Ψ , the product state with $|c_{NLn}|^2$ second largest as the ‘‘second largest content’’ and so on. For instance it can be read off from Tab. 4.1 that the state with an energy of $3.64 \hbar\omega$ at $a_{\text{sc}} = 0$ contains 63.2 % $|010\rangle$, 13.6 % $|100\rangle$, and 23.1 % other product states.

4.4 Conclusion

In conclusion, I have solved the model of two atoms in a harmonic potential interacting via a zero-range pseudopotential which accommodates a molecular state.

If the harmonic oscillator frequencies are equal for the two atoms, the center-of-mass and relative dynamics separate exactly and the spectrum

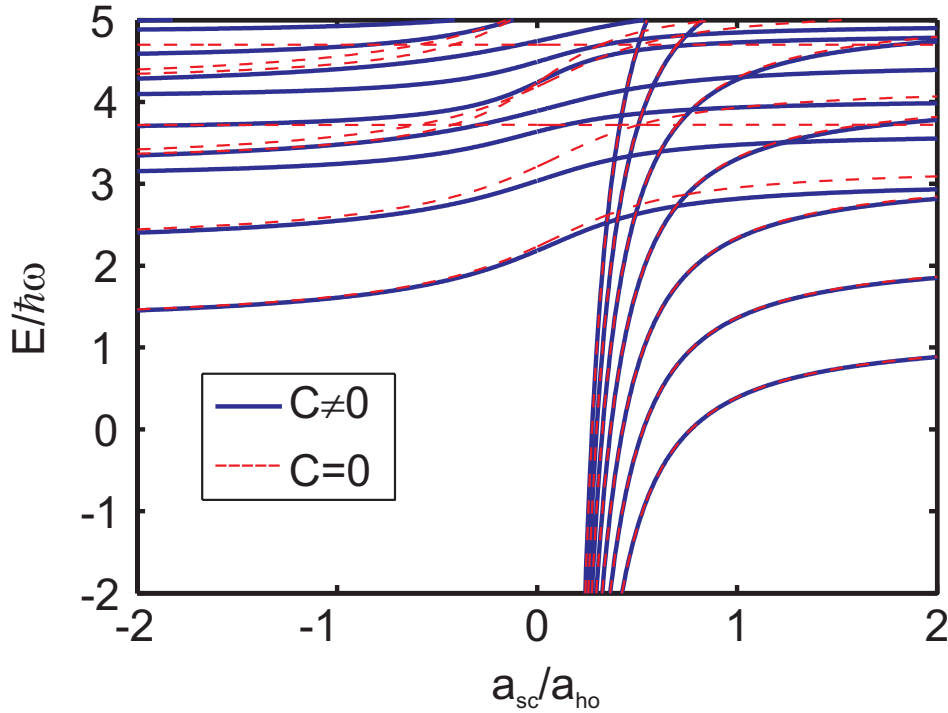


Figure 4.4: $J = 0$ spectrum of a Rb and a Li atom in a harmonic well in the pseudopotential approximation. The energy scale $\hbar\omega$ of the relative motion harmonic oscillator is chosen as the unit of energy. $\beta = (m_{\text{Li}}\omega_{\text{Li}}^2)/(m_{\text{Rb}}\omega_{\text{Rb}}^2) = 0.4$. The spectrum of the full Hamiltonian including the coupling between CM and relative dynamics is shown as the connected, blue lines. The spectrum that I get before including the coupling term is shown as red, dashed lines. I have included states up to $N = 6$, $n = 6$ and $L = l = 12$ which gives a total of 637 product basis states. Notice that there are 7 molecular states on the $a_{\text{sc}} > 0$ side, one for each N quantum number.

and the wave functions are given analytically. Generally this is not the case, but the spectrum can then be found by diagonalizing an analytically given Hamiltonian matrix in the basis consisting of products of center-of-mass and relative wave functions. The coupling between the two degrees of freedom causes a shift of the energy levels and it also means that the angular momentum belonging to the center-of-mass, respectively the relative, dynamics is no longer a good quantum number. The total angular momentum is still conserved, though.

Although the analytical expressions that I have derived for the radial parts of the coupling matrix elements are only valid in the pseudopotential approximation, the rest of the theory can be applied to any spherically symmetric interaction.

Energy	Largest content		Second largest content		Other
	$ NLn\rangle$	$ c_{NLn} ^2$ (%)	$ NLn\rangle$	$ c_{NLn} ^2$ (%)	$\sum c_{NLn} ^2$ (%)
2.18	$ 000\rangle$	96.2	$ 010\rangle$	3.5	0.3
3.04	$ 100\rangle$	79.1	$ 010\rangle$	11.2	9.8
3.64	$ 010\rangle$	63.2	$ 100\rangle$	13.6	23.1
3.89	$ 200\rangle$	64.0	$ 110\rangle$	16.7	19.3
4.24	$ 001\rangle$	80.8	$ 010\rangle$	12.6	6.6
4.49	$ 110\rangle$	33.5	$ 200\rangle$	22.8	43.7
4.74	$ 300\rangle$	51.1	$ 210\rangle$	18.3	30.6

Table 4.1: Product basis content at $a_{sc} = 0$ of the eigenstates of the full Hamiltonian for ^{87}Rb and ^6Li in a harmonic potential with $\beta = (m_{\text{Li}}\omega_{L_i}^2)/(m_{\text{Rb}}\omega_{R_b}^2) = 0.4$.

Energy	Largest content		Second largest content		Other
	$ NLn\rangle$	$ c_{NLn} ^2$ (%)	$ NLn\rangle$	$ c_{NLn} ^2$ (%)	$\sum c_{NLn} ^2$ (%)
-3.09	$ 000\rangle$	99.997	$ 010\rangle$	0.0013	0.0013
-2.12	$ 100\rangle$	99.994	$ 110\rangle$	0.002	0.004
-1.14	$ 200\rangle$	99.990	$ 210\rangle$	0.003	0.007
-0.16	$ 300\rangle$	99.985	$ 310\rangle$	0.004	0.011
0.81	$ 400\rangle$	99.981	$ 410\rangle$	0.005	0.014
1.79	$ 500\rangle$	99.977	$ 410\rangle$	0.006	0.017
2.53	$ 001\rangle$	91.0	$ 010\rangle$	8.0	1.0
2.76	$ 600\rangle$	99.973	$ 510\rangle$	0.008	0.020
3.29	$ 101\rangle$	58.7	$ 010\rangle$	22.0	19.3
3.81	$ 010\rangle$	58.9	$ 101\rangle$	21.7	19.4
4.11	$ 201\rangle$	43.8	$ 110\rangle$	18.8	37.4
4.57	$ 002\rangle$	64.0	$ 011\rangle$	17.1	18.9
4.71	$ 110\rangle$	26.4	$ 201\rangle$	16.9	56.7
4.93	$ 301\rangle$	30.6	$ 201\rangle$	17.2	52.2

Table 4.2: Product basis content at $a_{sc} = 0.36 a_{ho}$ of the eigenstates of the full Hamiltonian for ^{87}Rb and ^6Li in a harmonic potential with $\beta = (m_{\text{Li}}\omega_{L_i}^2)/(m_{\text{Rb}}\omega_{R_b}^2) = 0.4$. The molecular states are almost pure product states with $n = 0$, $L = 0$ and a well defined CM excitation, N , whereas for all other states the CM and the relative dynamics are entangled.

Chapter 5

Resonant Dynamics near a Feshbach resonance

Some of the results in Sec. 5.1-5.3 are published in [2].

Some of the results in Sec. 5.1-5.2 and in Sec. 5.4-5.5 have been submitted for publication, see Arxiv reference [3].

In the preceding chapter we have studied the spectrum of two harmonically confined and interacting atoms and I have shown how the time-independent Schrödinger equation can be solved in the pseudopotential approximation, even in the heteronuclear case. It is now time to allow the interaction $V_{\text{int}}(r)$ to be time-dependent and employ the time-dependent Schrödinger equation to obtain dynamical equations for the system (Sec. 5.1). As a specific application I will discuss resonant transitions by oscillating magnetic fields. The idea that was proposed and used by Thompson et al. [91] and Greiner et al. [148] is to apply small sinusoidal oscillations of the magnetic field around a fixed value B' close to a Feshbach resonance:

$$B(t) = B' + b \sin(\omega_B t). \quad (5.1)$$

If $\hbar\omega_B$ matches the energy difference between two stationary states, it is possible to transfer population from one state to another (for instance to the molecular state) or to create well controlled quantum mechanical superposition states (Sec. 5.2-5.4). In the heteronuclear case it is particularly interesting to see if one can get 100 % conversion efficiency for molecule production in principle (Sec. 5.4) and to actively use the coupling between the center-of-mass (CM) and relative dynamics to transfer the atoms into states where the relative motion has a nonzero mean angular momentum (Sec. 5.5).

From the point of view of molecule production, the modulation technique can be seen as an alternative to the traditional way of sweeping across

the resonance, see Fig. 5.1. It offers the opportunity to associate atoms into molecules without crossing the Feshbach resonance which, especially in the case of an atomic cloud in an optical or magnetic trap, is an attractive possibility due to the high inelastic collision rate at the center of the Feshbach resonance. If the technique is applied to two atoms in an optical lattice well, it can be used to make transitions between, and superposition states of, numerous different quantum states (including but not limited to the molecular state).

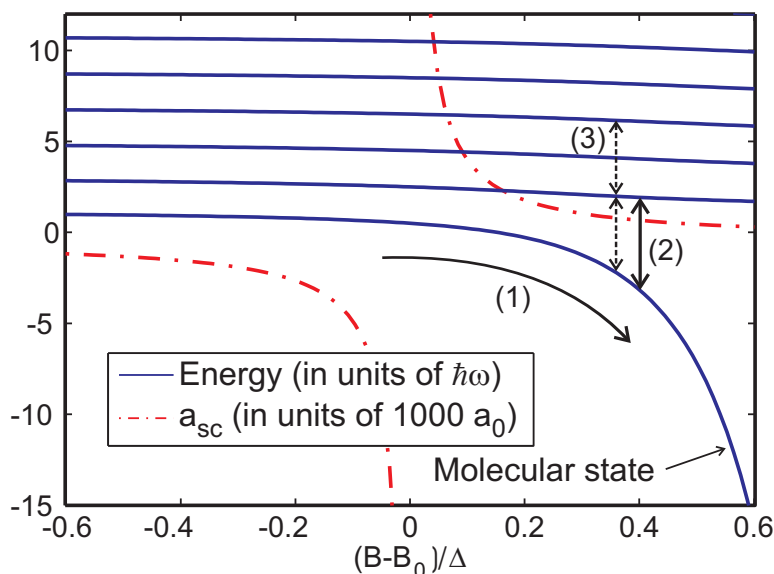


Figure 5.1: The s-wave spectrum in the pseudopotential model around the $B_0 = 155$ G Feshbach resonance in ^{85}Rb in a harmonic oscillator trap with $\omega = 2\pi \times 30$ kHz. The variation of the scattering length a_{sc} as a function of B is shown as a dot-dashed line. The typical adiabatic production of molecules by a magnetic field sweep across the resonance is indicated by the arrow (1). Arrow (2) illustrates the production of molecules by resonant association as analyzed here, while the dotted arrows (3) show an accidental three-level resonance (discussed in Sec. 5.2.2).

The modulation technique has also been used to produce and make spectroscopy on ultracold heteronuclear ^{87}Rb - ^{85}Rb molecules [149], to probe the excitation spectrum of a Fermi gas in the BEC-BCS crossover regime [148], and to infer the lifetime of short-lived Feshbach molecules by looking at the width of the resonance feature [150]. It differs in principle from the traditional RF spectroscopy used in e.g. [108, 151, 152] in that the atoms are not transferred to other hyperfine levels, and in that it is the tunable interatomic interaction that drives the transition.

5.1 Dynamical equations

The Hamiltonian is explicitly time dependent through the scattering length which is a function of the time-dependent magnetic field $B(t)$. I shall label the eigenstates at a given time by $|\Psi_q(t)\rangle$ and their energies E_q . They will form a complete set at any given time. We expand the actual wave function $|\Psi(t)\rangle$ on these states:

$$|\Psi(t)\rangle = \sum_q c_q(t) |\Psi_q(t)\rangle \quad (5.2)$$

Inserting into the time-dependent Schrödinger equation, $i\hbar \partial\Psi(t)/\partial t = H(t)\Psi(t)$, we get

$$i\hbar \sum_q \frac{dc_q(t)}{dt} |\Psi_q(t)\rangle + i\hbar \sum_q c_q(t) \left. \frac{\partial |\Psi_q(t')\rangle}{\partial t'} \right|_{t'=t} = H(t) \sum_q c_q(t) |\Psi_q(t)\rangle. \quad (5.3)$$

Projecting onto the state $\langle \Psi_p(t) |$ and using orthonormality we get

$$i\hbar \frac{dc_p(t)}{dt} + i\hbar \sum_q c_q(t) \left\langle \Psi_p(t) \left| \frac{\partial \Psi_q(t')}{\partial t'} \right. \right\rangle_{t'=t} = E_p(t) c_p(t). \quad (5.4)$$

So even if the eigenstates are orthogonal at any instant, transitions can happen because an eigenstate can couple to the time derivative of the other eigenstates. The time derivative can be put outside the inner product (because time differentiation and space integration are interchangeable) so

$$\left\langle \Psi_p(t) \left| \frac{\partial \Psi_q(t')}{\partial t'} \right. \right\rangle_{t'=t} = \frac{\partial}{\partial t'} \langle \Psi_p(t) | \Psi_q(t') \rangle \Big|_{t'=t}. \quad (5.5)$$

This equation shows that if we know the matrix elements $\langle \Psi_p(t) | \Psi_q(t') \rangle$ we also know the overlap between Ψ_p and the time derivative of Ψ_q . We put it into (5.4) to get the following set of differential equations

$$\boxed{i\hbar \frac{dc_p(t)}{dt} = E_p(t) c_p(t) - i\hbar \sum_q \frac{\partial}{\partial t'} \langle \Psi_p(t) | \Psi_q(t') \rangle \Big|_{t'=t} c_q(t).} \quad (5.6)$$

For a finite number of states this set of equations can be solved directly using Matlab's standard differential equation solver. Also, the sum in the second term on the right hand side becomes a product of a matrix and the column vector c_q .

Regarding the heteronuclear case, we note that if the time-varying interaction is spherically symmetric (such that it only enters in the radial part

of the relative Schrödinger equation) we cannot have transitions between states with different J and m_J , because unless $J = J'$ and $m_J = m'_J$

$$\langle \Psi_p^{Jm_J}(t) | \Psi_q^{J'm'_J}(t') \rangle \quad (5.7)$$

is zero at all times, because the angular parts of the wave functions are time-independent and orthogonal. Therefore,

$$\frac{\partial}{\partial t'} \langle \Psi_p^{Jm_J}(t) | \Psi_q^{J'm'_J}(t') \rangle \Big|_{t'=t} \propto \delta_{JJ'} \delta_{m_J m'_J} \quad (5.8)$$

and we can stick to a specific Jm_J subspace (normally $J = 0$, $m_J = 0$) as in the stationary case. A variation of the magnetic field near an s-wave Feshbach resonance is an example of such a spherically symmetric time dependence whereas e.g. an optical Raman transition does not necessarily conserve J and m_J . From now on I will assume a spherically symmetric time dependence and stick to a specific Jm_J subspace.

In the non-separating case it would be inconvenient to do numerical calculations of the time evolution in the eigenbasis since we would have to diagonalize the Hamiltonian (4.57) in every time step. Instead I use the product basis (4.23):

$$\psi_{N L n l}^{J m_J} = \sum_{M m} \langle L M l m | J m_J \rangle \Phi_{N L M}(\mathbf{R}) \varphi_{n l m}(\mathbf{r}). \quad (5.9)$$

In this basis the above calculations remain valid except that H is no longer diagonal so (5.6) changes to

$$\boxed{i\hbar \frac{dc_p(t)}{dt} = \sum_q H_{pq}(t) c_q(t) - i\hbar \sum_q \frac{\partial}{\partial t'} \langle \psi_p(t) | \psi_q(t') \rangle \Big|_{t'=t} c_q(t).} \quad (5.10)$$

where H_{pq} is given in (4.57). The explicit expression for the time derivative of $\langle \psi_p(t) | \psi_q(t') \rangle$ in the basis (5.9) is

$$\begin{aligned} \frac{\partial}{\partial t'} \langle \psi_p(t) | \psi_q(t') \rangle \Big|_{t'=t} &= \sum_{M_p m_p M_q m_q} \langle L_p M_p l_p m_p | J m_J \rangle \langle L_q M_q l_q m_q | J m_J \rangle \\ &\times \langle \Phi_{N_p L_p M_p} | \Phi_{N_q L_q M_q} \rangle_{\mathbf{R}} \frac{\partial}{\partial t'} \langle \varphi_{n_p l_p m_p}(t) | \varphi_{n_q l_q m_q}(t') \rangle_{\mathbf{r}} \Big|_{t'=t} \end{aligned} \quad (5.11)$$

where we have exploited that only the relative wave function φ is time dependent. The CM states are orthonormal:

$$\langle \Phi_{N_p L_p M_p} | \Phi_{N_q L_q M_q} \rangle_{\mathbf{R}} = \delta_{N_p N_q} \delta_{L_p L_q} \delta_{M_p M_q}. \quad (5.12)$$

In the s-wave pseudopotential model only relative states φ_{nlm} with $l = 0$ feel the pseudopotential [132] so only those states are time dependent. Therefore, if $l_q \neq 0$ we immediately get

$$\left. \frac{\partial}{\partial t'} \langle \varphi_{n_p l_p m_p}(t) | \varphi_{n_q l_q m_q}(t') \rangle_{\mathbf{r}} \right|_{t'=t} = 0. \quad (5.13)$$

If $l_p \neq 0$ and $l_q = 0$ we have $\langle \varphi_{n_p l_p m_p}(t) | \varphi_{n_q l_q m_q}(t') \rangle = 0$ at all times, because the time-independent angular parts of the wave functions are orthogonal. So the time derivative in (5.11) is nonzero only when $l_p = l_q = 0$.

Since $\langle L_p M_p 00 | J m_J \rangle = \delta_{L_p J} \delta_{M_p m_J}$ we have, in summary

$$\begin{aligned} & \left. \frac{\partial}{\partial t'} \langle \psi_p(t) | \psi_q(t') \rangle \right|_{t'=t} \\ &= \delta_{N_p N_q} \delta_{L_p J} \delta_{L_q J} \delta_{M_p M_J} \delta_{M_q M_J} \delta_{l_p 0} \delta_{l_q 0} \left. \frac{\partial}{\partial t'} \langle \varphi_{n_p 00}(t) | \varphi_{n_q 00}(t') \rangle_{\mathbf{r}} \right|_{t'=t}. \end{aligned}$$

(5.14)

One of the great advantages of the pseudopotential model is that the matrix element $\langle \varphi_{\nu 00} | \varphi_{\nu' 00} \rangle$ can be calculated analytically. We can rewrite the time derivative using the chain rule:

$$\left. \frac{\partial}{\partial t'} \langle \varphi_{n_p 00}(t) | \varphi_{n_q 00}(t') \rangle_{\mathbf{r}} \right|_{t'=t} = \frac{dB}{dt} \frac{da_{\text{sc}}}{dB} \left(\frac{da_{\text{sc}}}{d\nu} \right)^{-1} \left. \frac{\partial}{\partial \nu'} \langle \varphi_{\nu_p 00} | \varphi_{\nu' 00} \rangle_{\mathbf{r}} \right|_{\nu'=\nu_q} \quad (5.15)$$

where da_{sc}/dB is given by (4.53):

$$\frac{da_{\text{sc}}}{dB} = \frac{-\Delta}{(B - B_0)^2} a_{\text{bg}} \quad (5.16)$$

and $da_{\text{sc}}/d\nu$ is given from (4.48):

$$\begin{aligned} \frac{da_{\text{sc}}}{d\nu} &= \frac{d}{d\nu} \frac{\Gamma(-\nu - 1/2)}{2\Gamma(-\nu)} = \frac{\Gamma(-\nu - 1/2)}{2\Gamma(-\nu)} [\psi(-\nu) - \psi(-\nu - 1/2)] \\ &= \frac{a_{\text{sc}}}{[f(\nu)]^2} = \frac{a_{\text{bg}}}{[f(\nu)]^2} \frac{B - B_0 - \Delta}{B - B_0} \end{aligned} \quad (5.17)$$

where

$$f(\nu) = \frac{1}{\sqrt{\psi(-\nu) - \psi(-\nu - \frac{1}{2})}} \quad (5.18)$$

and ψ is the digamma function (C.18). The overlap $\langle \varphi_{\nu 00} | \varphi_{\nu' 00} \rangle$ can be calculated by a trick involving a Wronskian [133], but the integral can also be looked up, see Appendix C.2. The result is (C.21-C.22):

$$\langle \varphi_{\nu 00} | \varphi_{\nu' 00} \rangle = \frac{f(\nu')f(\nu)}{\nu - \nu'} \times \frac{\Gamma(-\nu')\Gamma(-\nu - \frac{1}{2}) - \Gamma(-\nu)\Gamma(-\nu' - \frac{1}{2})}{\sqrt{\Gamma(-\nu' - \frac{1}{2})\Gamma(-\nu')}} \sqrt{\Gamma(-\nu - \frac{1}{2})\Gamma(-\nu)}. \quad (5.19)$$

5.2 Small amplitude modulations

If we take the sinusoidal magnetic field dependence (5.1) in (5.6) we get the following equation for the eigenstate coefficients

$$i\hbar \frac{dc_p(t)}{dt} = E_p(t)c_p(t) - i\hbar \cos(\omega_B t) \sum_q \Omega_{pq}(B(t)) c_q(t). \quad (5.20)$$

where the Rabi frequencies Ω_{pq} are generally given by

$$\Omega_{pq}(B) = b\omega_B \left. \frac{\partial}{\partial B'} \langle \Psi_p(B) | \Psi_q(B') \rangle \right|_{B'=B}. \quad (5.21)$$

One could apply the rotating wave approximation to get rid of the $\cos(\omega_B t)$ factor for small modulations, but in the numerical calculations I have chosen to stick to the exact formulas.

Eq (5.20) is very similar to the dynamical equations for an atom in an external laser field in the dipole approximation. The difference is that the eigenenergies E_p and the Rabi frequencies Ω_{pq} are time-dependent. But for sufficiently small modulation amplitudes $b \ll \Delta$, the time dependence of E_p and Ω_{pq} can be neglected and we expect the modulation to be equivalent to radiative coupling of atomic energy levels. Especially, if $\hbar\omega_B$ is close to the energy difference between two eigenstates p and q , and we have all the population in the states p initially, we can expect to see Rabi oscillations between the two states with an oscillation amplitude that is given solely by the detuning (see e.g. Eq. (1.12) in [112])¹:

$$|c_q(t)|^2 = \left(\frac{\Omega_{pq}}{\Omega'_{pq}} \right)^2 \sin^2 \left(\frac{\Omega'_{pq} t}{2} \right) = \left(\frac{\Omega_{pq}}{\Omega'_{pq}} \right)^2 (1 - \cos(\Omega'_{pq} t)) \quad (5.22)$$

$$|c_p(t)|^2 = 1 - |c_q(t)|^2 \quad (5.23)$$

where

$$\Omega'_{pq} = \sqrt{\Omega_{pq}^2 + (\omega_B - (E_p - E_q)/\hbar)^2}. \quad (5.24)$$

¹This assumes that $\omega_B \gg |\omega_B - (E_p - E_q)/\hbar|$ such that the rotating wave approximation can be applied.

In particular, if $\hbar\omega_B = |E_p - E_q|$, we expect to see full contrast oscillations.

In the separating case where the relative dynamics is uncoupled from the CM dynamics we have the following explicit formula in the s-wave pseudopotential approximation (see 5.15-5.17)

$$\Omega_{pq} = \frac{(-b/\Delta)\omega_B}{\left(\frac{B-B_0}{\Delta}\right)\left(\frac{B-B_0}{\Delta} - 1\right)} f(\nu_q)^2 \left. \frac{\partial}{\partial \nu'} \langle \varphi_{\nu_p 00} | \varphi_{\nu' 00} \rangle_{\mathbf{r}} \right|_{\nu'=\nu_q} \quad (5.25)$$

where $f(\nu)$ is given in (5.18) and the ν' -differentiation can be done numerically from (5.19). We note that $\Omega_{pp} = 0$ and $\Omega_{qp} = -\Omega_{pq}$.

The Rabi frequencies are proportional to the modulation amplitude (b/Δ). The rest of the expression (5.25) is plotted for an $\omega = 2\pi \times 30$ kHz lattice well and $\omega_B = |E_p - E_q|/\hbar$ in Fig. 5.2 for the case $a_{\text{bg}} = -443 a_0$ (as we have for the 156 G resonance in ^{85}Rb) and in Fig. 5.3 for the case $a_{\text{bg}} = 100.5 a_0$ (as we have for the 1007 G resonance in ^{87}Rb). Notice that since the Rabi frequencies are proportional to ω_B there is a significantly stronger resonant coupling to the lowest (molecular) state than among the atomic states on the molecular side of the resonance. Notice that the two

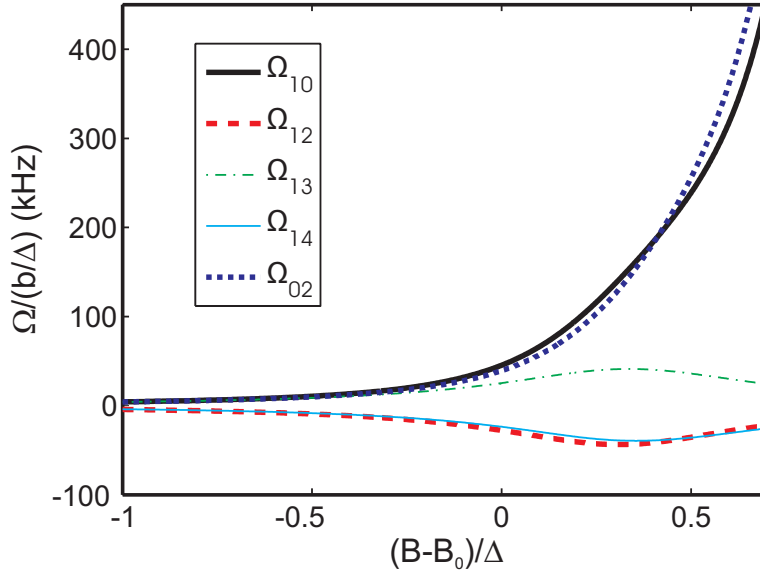


Figure 5.2: Amplitude normalized Rabi frequencies on resonance for ^{85}Rb at the 156 G Feshbach resonance. The harmonic oscillator frequency is $2\pi \times 30$ kHz. The parameters are as in Fig. 5.1. The states are labelled 0, 1, 2, ... with increasing energy. E.g., Ω_{10} is the coupling between the two states with lowest energy.

plots are qualitatively different. The difference can be partly attributed to the different behaviour of the molecular binding energy when B approaches $B_0 - \Delta$ (positive scattering length side in ^{87}Rb) compared to when B approaches $B_0 + \Delta$ (positive scattering length side in ^{85}Rb) - see the discussion

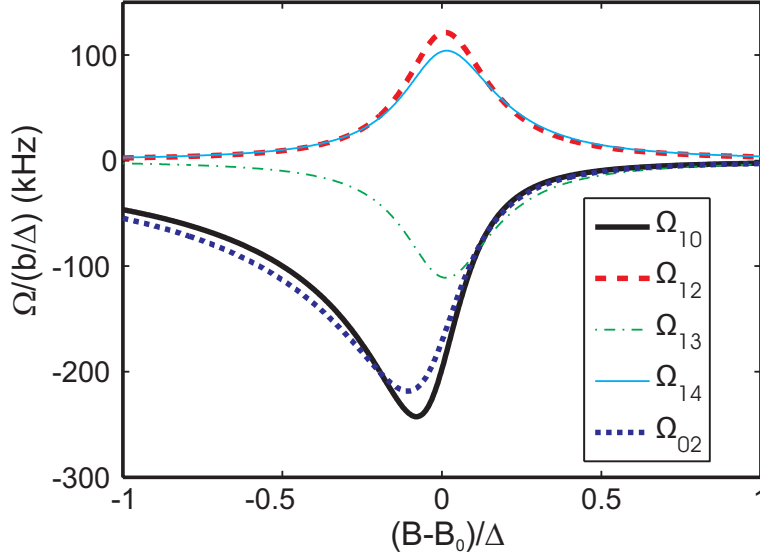


Figure 5.3: Amplitude normalized Rabi frequencies in ^{87}Rb at the 1007 G Feshbach resonance (cf. Fig. 5.2). Here the positive scattering length (molecular) side is to the left of the resonance, because $a_{\text{bg}} = 100.5 a_0 > 0$. The harmonic oscillator frequency is $\omega = 2\pi \times 30$ kHz.

at the end of Sec. 4.3.2. In the latter case, the binding energy and thus the resonant frequency ω_B^{res} entering (5.25) diverges for coupling to the molecular state.

Using Eqs. (5.20) and (5.25) I have calculated the dynamics of the resonant association of two ^{85}Rb atoms in an $\omega = 2\pi \times 30$ kHz lattice well. Referring to the 156 G resonance I use $B' = B_0 + 0.4\Delta = 159.33$ G, and $b = 0.01$ and I start out in the lowest atomic state (on the 2nd lowest, blue curve in the upper part of Fig. 4.3). The expected resonant frequency is

$$\omega_B^{\text{res}} = (E_1(B') - E_0(B'))/\hbar = 5.079 \omega = 2\pi \times 152.4 \text{ kHz}. \quad (5.26)$$

Although the calculation is done with 10 basis states, the dynamics in Fig. 5.4 shows full two-level Rabi-oscillations as one would expect. A fit of the molecular state population to a $\sin^2(\Omega/2 \times t)$ function shows that the Rabi frequency is $\Omega = 2\pi \times 1.84$ kHz which exactly matches the value of the Rabi frequency predicted from (5.25) and displayed in Fig. 5.2. Choosing the oscillation time such that $\Omega t = \pi$ (a π -pulse) one can transform the atomic pair into a molecule with unit probability and by varying the interaction time, a wide range of well-controlled superposition states of the molecular and atomic component can also be prepared.

In the experiment [91] where ^{85}Rb molecules were produced by the modulation technique, Rabi oscillations were also observed, but since those ex-

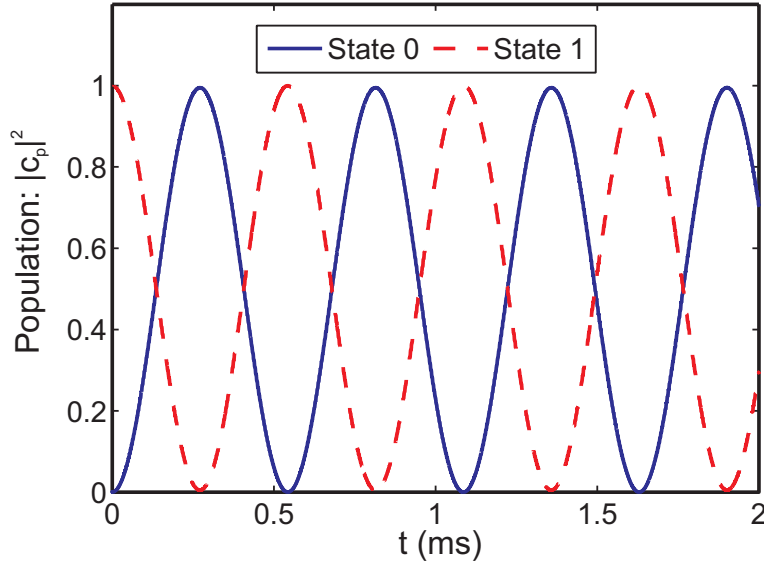


Figure 5.4: Dynamics of the resonant process at $B' = B_0 + 0.4\Delta$ for $\omega = 2\pi \times 30$ kHz and $a_{\text{bg}} = -443 a_0$. The field is modulated at an angular frequency $\omega_B = 2\pi \times 152.4$ kHz, with the amplitude $b = 0.01\Delta$. The frequency of the Rabi oscillations is $\Omega = 2\pi \times 1.84$ kHz in perfect agreement with (5.25) and Fig. 5.2.

periments were performed with a thermal cloud of atoms in a magnetic trap, the Rabi oscillations had a poor contrast and damped out on a timescale of a few ms. Eventually the molecule conversion saturated at a value of about 30 % of the initial number of atoms. A theoretical treatment of the two-atom dynamics for a thermal ensemble of atoms has recently been made by Hanna et al. [153] where the damping is explained by decoherence due to the thermal energy spread, whereas a full understanding of the saturation probably calls for a many-body treatment (which to my knowledge has not been carried out yet).

The fact that we see full contrast Rabi oscillations shows that the modulation technique offers a great opportunity to make efficient state transfers and controlled superposition states of atom pairs in lattice sites. Varying the modulation frequency, amplitude and phase there are more degrees of freedom to play with than a simple sweep across the resonance, or a jump close to the resonance, can offer. In connection with quantum information applications, modulation sequences, or possibly composite modulation sequences with built-in robustness against frequency and amplitude errors known from NMR technology, could also be a versatile tool to manipulate quantum states in a controlled way.

It should be mentioned that the first low contrast Rabi oscillations between an atomic and a molecular state were seen experimentally already

in 2002 [154] and atom-molecule oscillations have also been observed using photoassociation in an optical lattice in the Mott insulating state [155]. Very recently, high contrast Rabi oscillations between atomic and molecular states of ^{87}Rb atom pairs in optical lattice wells in the Mott insulating state have been reported using a fast jump close to a Feshbach resonance [156]. Also, high contrast coherent oscillations between ultracold molecular states with different angular momenta have been produced [157].

5.2.1 Adiabatic passages

Application of a π -pulse in the above scheme relies on the resonance and Rabi frequencies being exactly known and identical for all lattice sites. A more robust scheme for making a full transfer from one state to another is to make an adiabatic passage, that is to sweep the frequency slowly across the resonance frequency, ω_B^{res} . A linear frequency sweep from ω_{initial} to ω_{final} of duration Δt is generated using the following magnetic field oscillation²:

$$B(t) = B' + b \sin \left(\int_0^t \omega(t') dt' \right) \quad (5.27)$$

$$= B' + b \sin \left[\left(\omega_{\text{initial}} + \frac{1}{2}(\omega_{\text{final}} - \omega_{\text{initial}}) \frac{t}{\Delta t} \right) t \right] \quad (5.28)$$

Using a constant amplitude linear frequency sweep from 10% below to 10% above ω_B^{res} of 5 ms duration (9.2 Rabi periods), I get the dynamics shown in Fig. 5.5. After just a few Rabi oscillation periods the molecular state population settles near 100 %. In addition to correcting for inhomogeneity effects, a frequency sweep will also introduce some robustness against technical noise in the magnetic field value, as long as this noise is present only on longer timescales than that given by the sweeping time. This is especially relevant with respect to application to more narrow Feshbach resonances like in ^{87}Rb .

5.2.2 Three-level resonances

At certain magnetic fields three levels are coupled in a ladder configuration, because $\hbar\omega_B^{\text{res}}$ matches not only the energy distance to the molecular state, but also the distance to a higher lying atomic state (see Fig. 5.1). This leads to a more complicated three-level dynamics, but since the coupling to the higher lying atomic state is significantly smaller than the coupling to the molecular state (see Fig. 5.2), the higher lying atomic level becomes only sparsely populated. This is fortunate from the point of view of molecular formation. In the present case of $\omega = 2\pi \times 30$ kHz and $a_{\text{bg}} = -443 a_0$, the

²It is tempting to write the sine function as $\sin(\omega(t)t)$, but this oscillation does not have an instantaneous frequency of $\omega(t)$ (it misses the factor of 1/2 in 5.28).

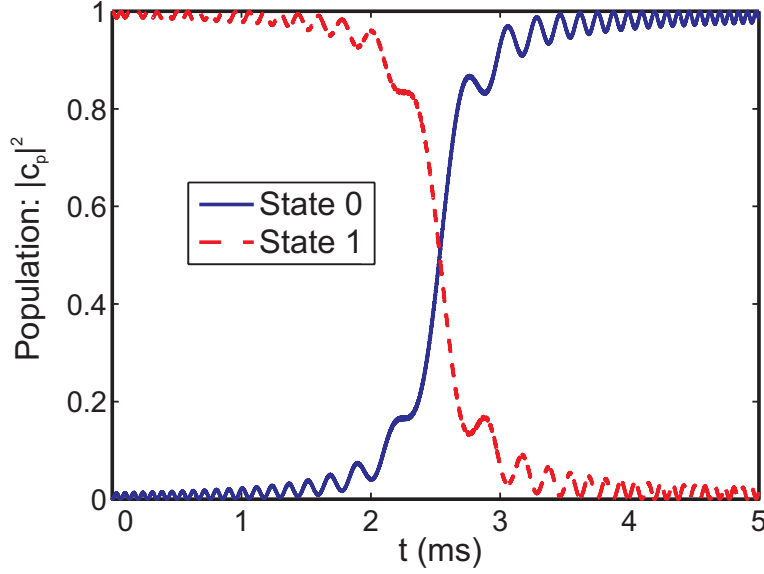


Figure 5.5: 5 ms linear frequency sweep from 10% below to 10% above the resonance frequency $\omega_B^{\text{res}} = 2\pi \times 152.4$ kHz at an applied field $B' = B_0 + 0.4\Delta$ for $\omega = 2\pi \times 30$ kHz and $a_{\text{bg}} = -443 a_0$. The modulation has the constant amplitude $b = 0.01\Delta$. There are 10 basis states included in the calculation.

lowest B-field on the molecular side of the resonance, where such a three-level resonance occurs, is $B' = B_0 + 0.3582\Delta$ shown with the dashed arrows in Fig. 5.1 ($\omega_B^{\text{res}} = 2\pi \times 125.1$ kHz). Simulation of the dynamics in this case shows oscillations with a peak population of 6 % in the excited atomic state (see Fig. 5.6). All remaining population is distributed between the molecular and the lowest atomic state. At the next three-level resonance at $B' = B_0 + 0.4385\Delta$ the peak population of the higher lying atomic state becomes only 4 %.

5.3 Large amplitude modulations

One might also consider the possibility of using larger oscillation amplitudes. This makes the association quicker, can be used to keep the magnitude of the harmonic modulation well above the technical noise level and gives also some robustness against a noisy value of B' . Our simulations show that if the coupling strength is not much smaller than Δ , the resonance frequency is significantly shifted and the oscillations are distorted, but there is still a remarkably resonant behaviour with a high molecular peak population. For instance with $B' = B_0 + 0.4\Delta$ and $b = 0.2\Delta$, I must use a value of ω_B which is 55 % larger than that in Fig. 5.4 to get maximum population oscillations, and I then get a molecular peak population of around 90 % (Fig. 5.7). I

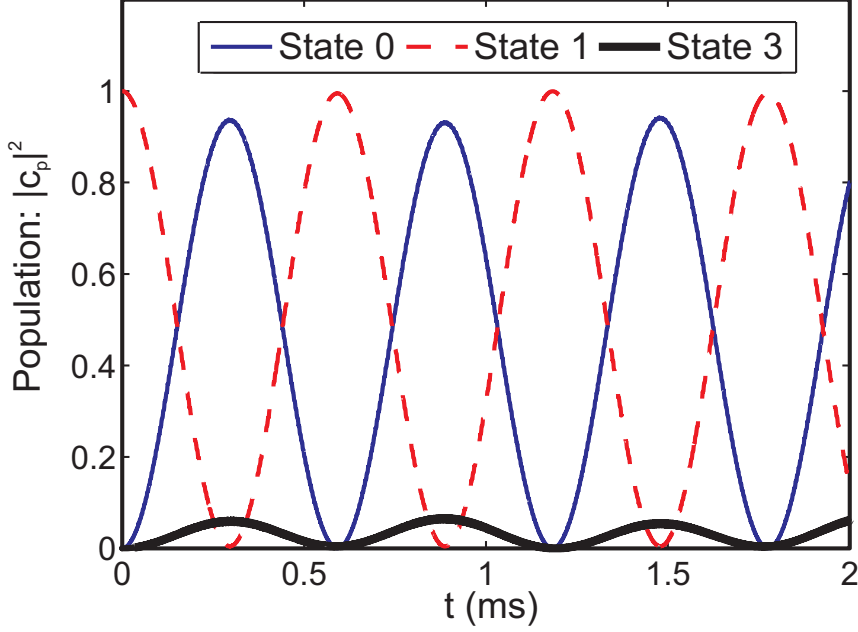


Figure 5.6: Dynamics of the resonant process at the 3-level resonance at $B' = B_0 + 0.3582\Delta$ driven by a modulation with frequency $\omega_B = 2\pi \times 125.1$ kHz and amplitude $b = 0.01\Delta$. All other parameters are as in Fig. 5.4.

attribute the frequency shift to the strongly increasing slope of the molecular level curve (Fig. 5.1) as the B-field is modulated to larger values, farther away from B_0 .

I have tried to apply frequency sweeps to the case of large modulation amplitudes, but unfortunately I have not succeeded in producing state transfers with any considerable efficiency in that case.

5.3.1 Association spectra

In order to investigate the resonant dynamics in the large amplitude case further, I have calculated the dynamics of molecule creation for different values of ω_B and recorded the peak norm of the molecular state. For a small amplitude $b = 0.01\Delta$ I get the spectrum shown in Fig. 5.8. There is a well-defined resonance at the expected resonance frequency $\omega_B = 2\pi \times 152$ kHz. A Lorentzian fit ($y = A\Delta^2/((f - f_0)^2 + \Delta^2)$) of the peak in the region $100 \text{ kHz} \leq \omega_B/2\pi \leq 204 \text{ kHz}$ gives a molecular peak amplitude of $A = 1.000(3)$ at $\omega_B = 2\pi f_0 = 2\pi \times 152.5(1)$ kHz and a HWHM (half width at half maximum) of $\Delta = 1.854(7)$ kHz which equals the Rabi frequency, Ω , in agreement with 5.22.

The spectra for larger modulation amplitudes, $b = 0.1\Delta$ and $b = 0.2\Delta$,

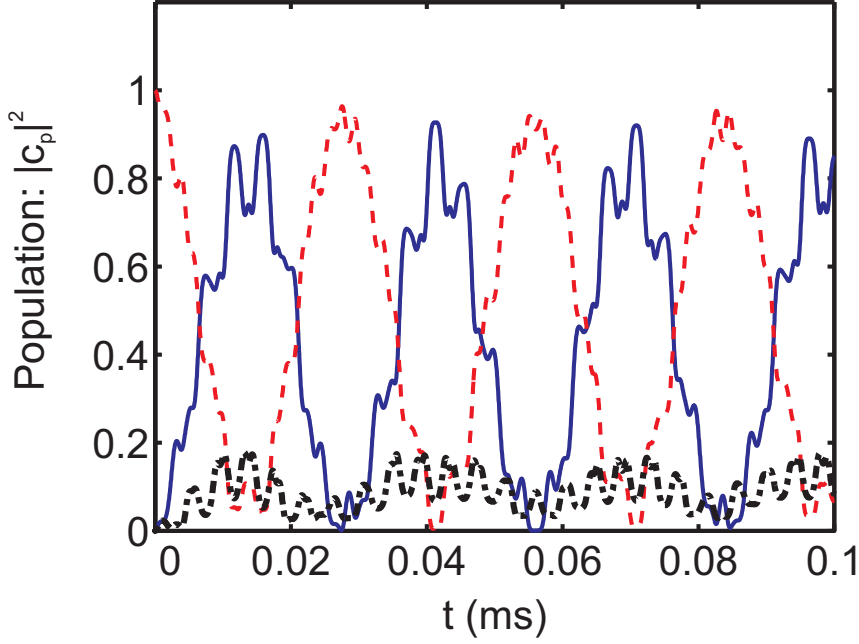


Figure 5.7: Dynamics of the molecular association process with a very high oscillation amplitude: $b = 0.2\Delta$. $B' = B_0 + 0.4\Delta$. The resonance frequency has shifted 55 % compared to the value in Fig. 5.4 so $\omega_B = 2\pi \times 236.3$ kHz. The frequency of the population oscillation is 36 kHz and the Rabi frequency predicted from (5.25) is 37 kHz. There are 20 basis states included in the calculation.

are shown in Figs. 5.9-5.10. We clearly see two interesting and qualitatively new phenomena:

- The resonance frequency ω_B^{res} is no longer $(E_1(B') - E_0(B'))/\hbar$ but is shifted towards a larger value as already noted above.
- There are several fractional harmonics visible (resonances at frequencies of the form $\omega_B = \omega_B^{\text{res}}/\mathcal{N}$, $\mathcal{N} = 1, 2, 3, \dots$).

The shift of the resonance frequency is a nonlinear function of the modulation amplitude b (see Fig. 5.11).

The fractional harmonics are somewhat similar to multi-photon transitions in atoms, but the mechanism is not quite the same and calls for further investigations. Such fractional harmonics have also been observed in optical traps at JILA for a Feshbach resonance in ^{40}K [158] and for a heteronuclear Feshbach resonance in a $^{87}\text{Rb}/^{85}\text{Rb}$ mixture [159].

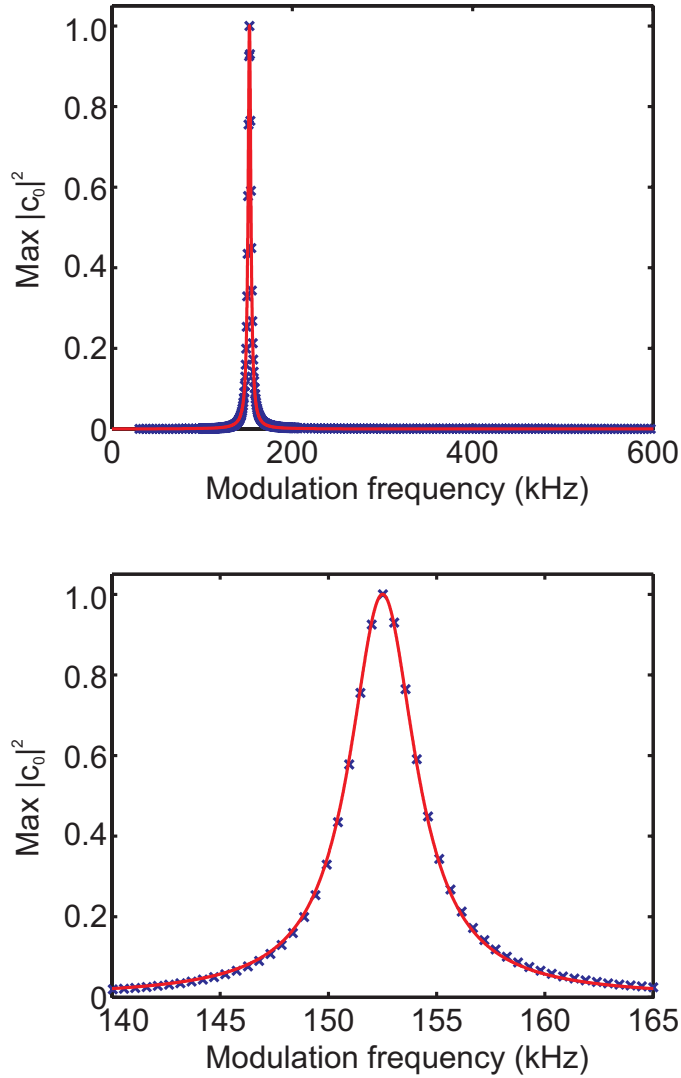
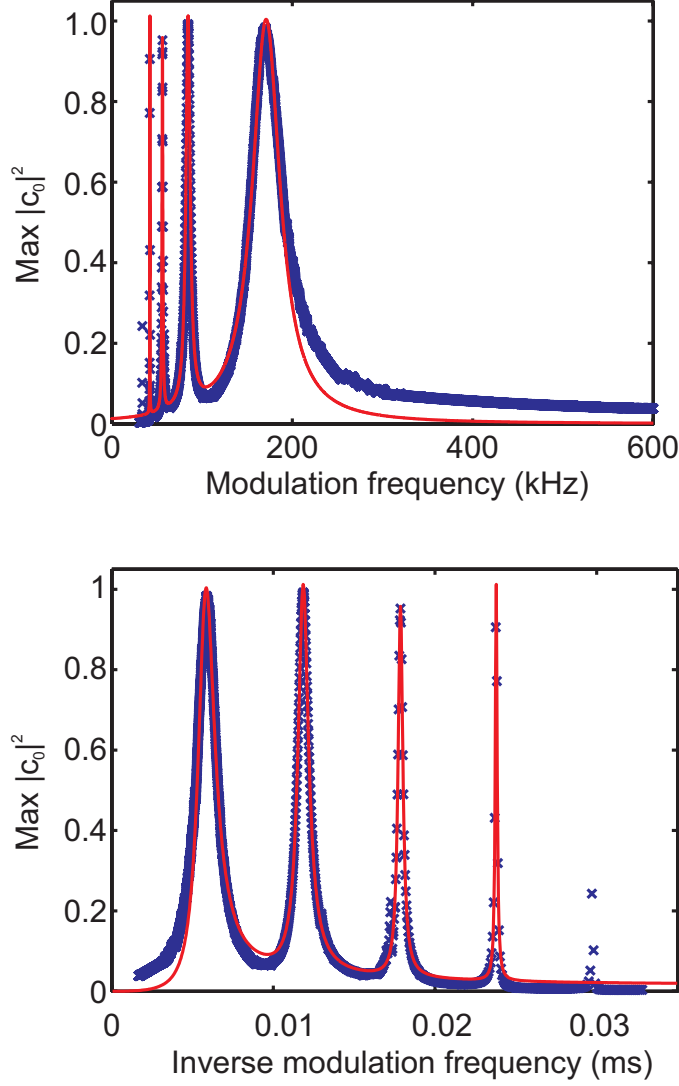
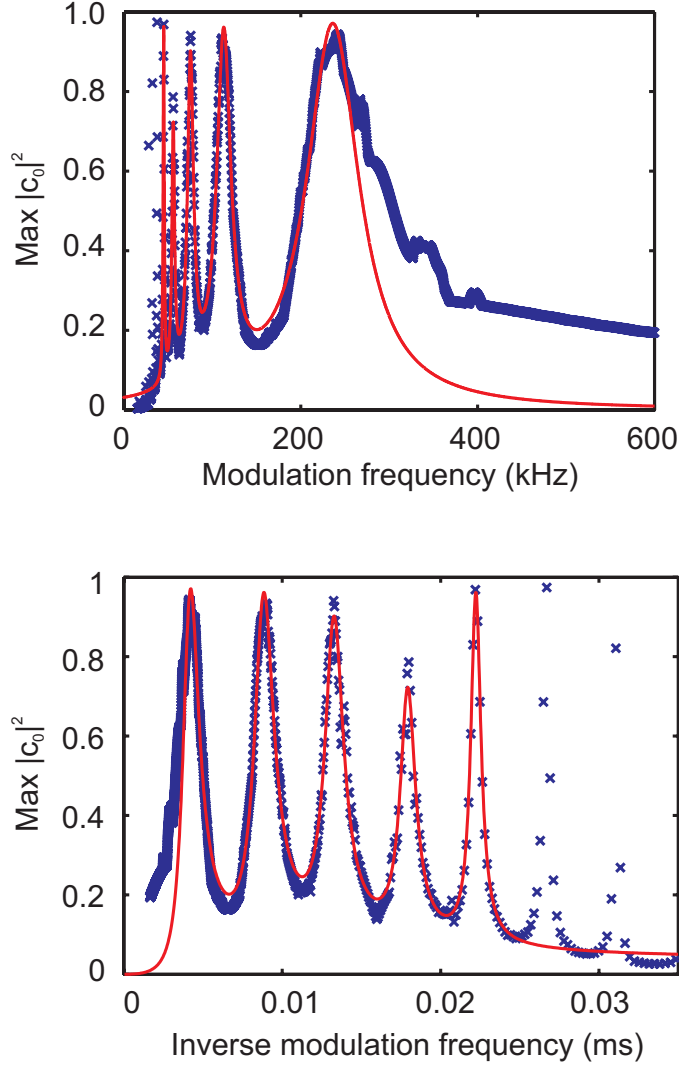


Figure 5.8: Association spectrum for a modulation amplitude of $b = 0.01\Delta$. For each modulation frequency, $f = \omega_B/2\pi$, the dynamics for molecular association has been calculated (cf. Fig. 5.4) during a time that equals 5 Rabi periods calculated from (5.25). The maximum value of the norm of the molecular state during this time evolution is shown in the plot. The connected, red line is a Lorentzian fit to the peak giving a molecular peak amplitude of $A = 1.000(3)$, a center frequency of $\omega_B = 2\pi f_0 = 2\pi \times 152.5(1)$ kHz and a HWHM (half width at half maximum) of $\Delta = 1.854(7)$ kHz. The lower figure is a close-up around the peak. The harmonic oscillator frequency is $\omega = 2\pi \times 30$ kHz, $a_{\text{bg}} = -443 a_0$ and $B' = B_0 + 0.4\Delta$. There are 10 basis states included in each calculation.



\mathcal{N}	A	f_0 (kHz)	Δ (kHz)
1	1.003(3)	171.03(5)	18.65(8)
2	0.967(6)	84.41(2)	2.8(2)
3	0.923(13)	55.99(2)	0.556(11)
4	0.99(3)	42.051(3)	0.124(5)

Figure 5.9: Association spectrum as a function of the modulation frequency $f = \omega_B/2\pi$ (upper figure) and the inverse modulation frequency $1/f$ (lower figure) for a modulation amplitude of $b = 0.1\Delta$. The other parameters are as in Fig. 5.8. The red line is a 4-peak Lorentzian fit ($R^2 = 0.994$) to the harmonics with $\mathcal{N} = 1, 2, 3, 4$ over the region $40 \text{ kHz} \leq \omega_B/2\pi \leq 190 \text{ kHz}$: $y = \sum_{\mathcal{N}=1}^4 A_{\mathcal{N}} \Delta_{\mathcal{N}}^2 / ((f - f_{0\mathcal{N}})^2 + \Delta_{\mathcal{N}}^2)$. The table lists the best-fit parameters. We note that the width of the main peak ($\mathcal{N} = 1$) is very close to the Rabi frequency $\Omega = 18.4 \text{ kHz}$ predicted from (5.25).



\mathcal{N}	A	f_0 (kHz)	Δ (kHz)
1	0.965(6)	236.3(4)	36.0(5)
2	0.876(12)	112.93(13)	9.7(2)
3	0.796(18)	75.30(9)	4.09(14)
4	0.62(3)	55.78(8)	1.83(11)
5	0.88(4)	45.00(4)	0.79(5)

Figure 5.10: Association spectrum as a function of the modulation frequency $f = \omega_B/2\pi$ (upper figure) and the inverse modulation frequency $1/f$ (lower figure) for a modulation amplitude of $b = 0.2\Delta$. The other parameters are as in Fig. 5.8. The red line is a 5-peak Lorentzian fit ($R^2 = 0.96$) to the harmonics with $\mathcal{N} = 1, 2, \dots, 5$ over the region $35 \text{ kHz} \leq \omega_B/2\pi \leq 260 \text{ kHz}$: $y = \sum_{\mathcal{N}=1}^5 A_{\mathcal{N}} \Delta_{\mathcal{N}}^2 / ((f - f_{0\mathcal{N}})^2 + \Delta_{\mathcal{N}}^2)$. The table lists the best-fit parameters. The asymmetry of the main harmonic is due to the nonlinear dependence of the scattering length on the magnetic field.

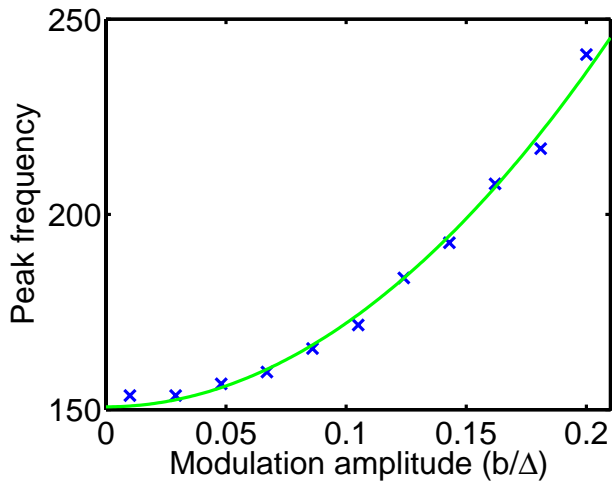


Figure 5.11: Plot of the resonance frequency (first harmonic) as a function of the modulation amplitude b showing the nonlinear dependence of the frequency shift. For each modulation amplitude, the figure shows the peak frequency of the association spectrum (cf. Figs. 5.8-5.10). The green, solid line is a quadratic fit to the points: $y = (2143(b/\Delta)^2 + 150.7)$ kHz. For each modulation amplitude, an association spectrum with 200 points in the region $(E_1 - E_0)/\hbar/1.1 \leq \omega_B \leq 1.7(E_1 - E_0)/\hbar$ has been calculated. The harmonic oscillator frequency is $\omega = 2\pi \times 30$ kHz and $a_{\text{bg}} = -443 a_0$. There are 10 basis states included in each calculation.

5.4 Associating heteronuclear molecules

According to Sec. 5.2, a small amplitude harmonic oscillation of the magnetic field at a frequency such that $\hbar\omega$ is resonant with the energy difference between two eigenstates will inevitably lead to full contrast Rabi oscillations as long as there is a finite coupling between the two states. Such a finite coupling arises whenever the product basis expansion of the two eigenstates at the given magnetic field B' contains basis functions of the form

$$\Phi_{NJM_J}(\mathbf{R})\varphi_{\nu 00}(\mathbf{r}) \quad \text{respectively} \quad \Phi_{NJM_J}(\mathbf{R})\varphi_{\nu' 00}(\mathbf{r}) \quad (5.29)$$

where $\nu' \neq \nu$ (see 5.14).

This means e.g. that efficient association of heteronuclear molecules should be possible. We can illustrate it in principle using the $^{87}\text{Rb}/^6\text{Li}$ system treated above. The scattering length at zero magnetic field was measured by C. Silber et al. [56] to be $20(+9/-6) a_0$. A Feshbach resonance with this background scattering length gives rise to the $J = 0$ spectrum shown in Fig. 5.12. If I oscillate the magnetic field resonantly around $B = B_0 - 0.05\Delta$ (corresponding to $a_{sc}/a_{ho} = 0.36$), I can produce full contrast Rabi oscillations between the lowest non-molecular state and the molecular ground state (illustrated with the lower, red arrow in the spectrum). The dynamics is shown in Fig. 5.13. In practice one might want to use an adiabatic passage to make a robust full transfer as illustrated in Sec. 5.2.1.

5.5 Creating nonzero angular momentum states

Another interesting fact is that the coupling of the CM and relative motion makes it possible to populate states with nonzero CM and nonzero relative angular momentum by oscillating the magnetic field close to a Feshbach resonance. It is intriguing that in this way a purely central interatomic interaction can be used to put angular momentum into the relative motion at the cost of exciting the CM motion as well.

For example the upper, green arrow in Fig. 5.12 illustrates a transfer from the non-molecular atomic ground state to a state with 59 % content of $L = l = 1$ (see Tab. 4.2). If the magnetic field is oscillated resonantly, Rabi oscillations between these two states can be produced (Fig. 5.14) and again a π -pulse or an adiabatic passage could in principle be used to make a full transfer. States with nonvanishing relative angular momentum may lead to interesting momentum distributions of the individual species when the atoms are released from the lattice. Nontrivial momentum distributions for higher partial waves have been observed for dissociated molecules released from an optical dipole trap [160, 161] as well as from an optical lattice [157].

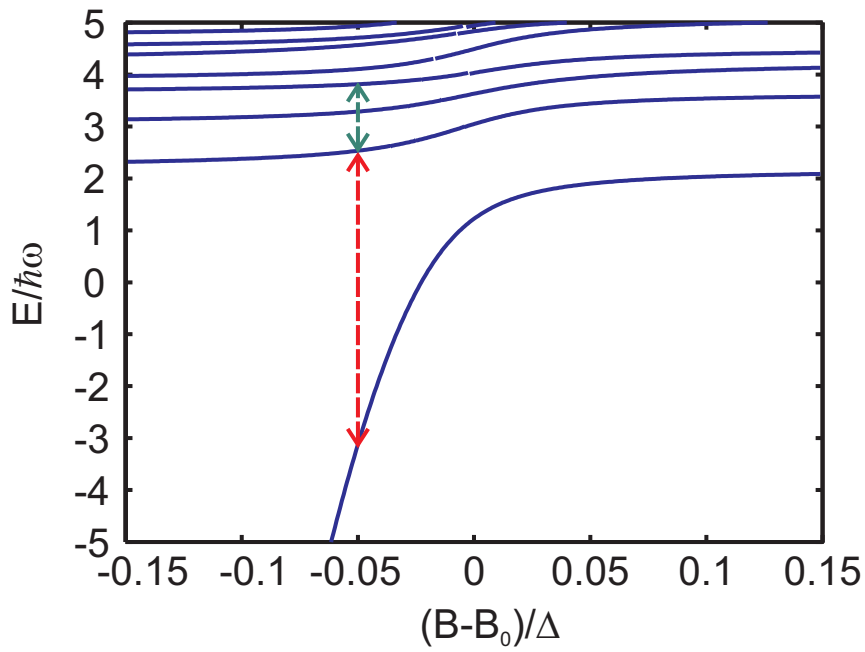


Figure 5.12: Spectrum for ^{87}Rb - ^6Li in an optical lattice well with $\omega_{\text{Rb}} = 2\pi \times 200$ kHz and $\beta = m_{\text{Li}}\omega_{\text{Li}}^2/(m_{\text{Rb}}\omega_{\text{Rb}}^2) = 0.4$ in the vicinity of a Feshbach resonance with $a_{\text{bg}} = 20 a_0$. Molecular states that have a CM excitation ($N > 0$) are not shown. Association of a heteronuclear molecule is indicated with the lower, red arrow while transfer to a state with angular momentum excitation is illustrated with the upper, green arrow.

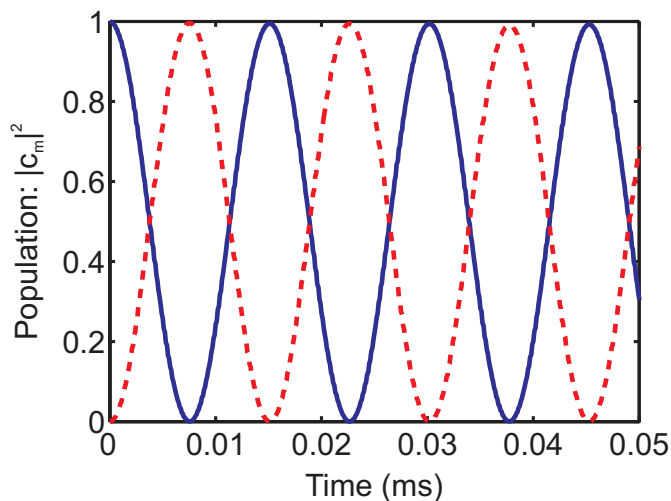


Figure 5.13: Resonant association of heteronuclear molecules by an oscillating magnetic field. The time dependent magnetic field is $B(t) = B_0 - 0.05\Delta + 0.005\Delta \sin(\omega_B t)$ where $\omega_B = 2\pi \times 2660$ kHz. The connected, blue line shows the population of the atomic ground state whereas the population of the molecular ground state is shown with the red, dashed line. $\omega_{Rb} = 2\pi \times 200$ kHz, $\beta = m_{Li}\omega_{Li}^2/(m_{Rb}\omega_{Rb}^2) = 0.4$. I have included states up to $N = 3$, $n = 3$ and $L = l = 6$.

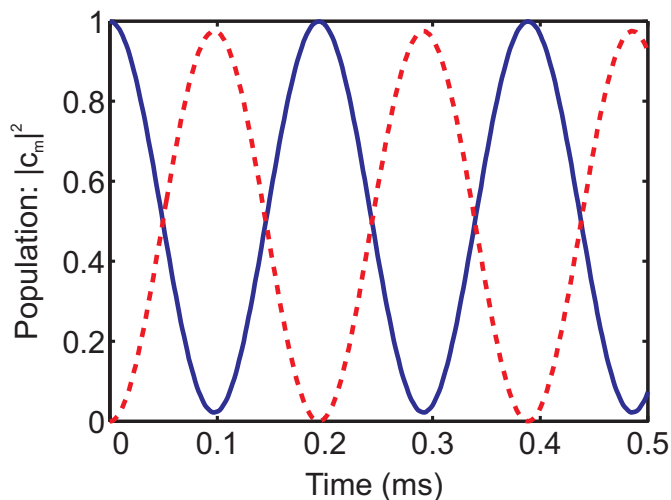


Figure 5.14: Rabi oscillations between the atomic ground state and a state with 59 % content of $L = l = 1$. The time dependent magnetic field is $B(t) = B_0 - 0.05\Delta + 0.005\Delta \sin(\omega_B t)$ where $\omega_B = 2\pi \times 601$ kHz. The blue line shows the population of the atomic ground state whereas the population of the excited angular momentum state is shown with the red, dashed line. The other parameters are as in Fig. 5.13.

5.6 Conclusion

I have used the theoretical model introduced in Ch. 4 to model the dynamics of two atoms in a deep optical lattice well in the vicinity of a Feshbach resonance. I have shown that a small oscillation of the magnetic field at a frequency that is resonant with the energy difference between two energy levels will always lead to full contrast Rabi oscillations. This has been used to demonstrate association of homonuclear as well as heteronuclear molecules with 100 % efficiency and to transfer the two atoms into a state with nonvanishing relative and center-of-mass angular momentum.

If the magnetic field is modulated with an amplitude that is a significant fraction of the width of the Feshbach resonance, nontrivial phenomena arise: The Rabi oscillations are distorted, but there is still a clearly resonant behaviour at a frequency which is shifted compared to the small-amplitude resonance. Furthermore, “multi-quanta” transitions arise at modulation frequencies of the form $\omega_B^{\text{res}}/\mathcal{N}$ where ω_B^{res} is the shifted resonance frequency. These “multi-quanta” transitions could be an interesting target for further investigations.

Chapter 6

Conclusion and Outlook

I think that one of the virtues of ultracold atomic physics is that it combines knowledge from many different branches of physics. It has given me the opportunity to use and extend my knowledge of several physics disciplines from both an experimental and theoretical point of view, especially optics, atomic physics, statistical physics and electromagnetism. Also, I have studied two very different kinds of systems: A gas of ultracold atoms in a time-dependent trapping potential behaving completely classically (but very complicated in other ways) to a system that contains only two particles and that is very quantum mechanical.

In Ch. 3 I have investigated a new way of producing mixtures of ultracold atomic gases which should be seen as an alternative to the two-species magneto-optical trap. A very close interplay between experiment and theory was absolutely necessary in order to understand and optimize the process. When I began to study the process, it was not even clear whether it was at all possible to do the mixing without throwing away most of the atoms. Fortunately it turned out that it was possible to carry out the process in such a way that there is almost no loss of atoms. The heating in the process is not larger than what would probably be acceptable for most applications. However, the study also revealed that certain experimental parameters have to be chosen with great care.

The dynamics of the atoms in the potential of the two merging quadrupole traps is also interesting itself, but quite complex since it is a non-equilibrium process. It would be interesting to apply a similar mixing process to even colder gases, maybe even BECs. This would, however, introduce several new challenges: Experimentally it would be necessary to use traps with a nonzero field minimum to avoid Majorana spin flips and theoretically it would e.g. be necessary to take collisions into account.

In the theoretical chapters I have provided a general scheme for dealing

with two harmonically confined and interacting atoms. The theory presented might serve as a basis for further investigations of confined, heteronuclear systems, possibly with more realistic interatomic potentials. Coherent processes driven by an oscillating magnetic field in the vicinity of a Feshbach resonance were also studied intensively. Whereas oscillations with small amplitudes lead to simple two-level dynamics, oscillations with large amplitudes exhibit a much more rich behaviour, and it would be interesting to understand this behaviour in larger detail.

It would be great to see an experimental demonstration of the dynamics. Also, it should be possible to create states with angular excitations of the relative and center-of-mass motion experimentally although it is not trivial how exactly such states would show up in a time-of-flight image.

During my time as a PhD student I was often surprised by the extremely rapid development within the field of ultracold atomic physics and the astonishing results reported from different groups all the time (such as the creation of the first molecular BECs and the creation of very long-lived Feshbach molecules in optical lattices). Since the creation of the first BECs of atomic gases the quantum mechanical wave function, which used to be a very abstract quantity, has become something which you can almost take an image of. This means that ultracold atoms offer outstanding opportunities to get a much better understanding of several quantum mechanical phenomena. Especially atoms with tunable interactions in optical lattices are promising candidates for quantum simulators and maybe even quantum computers. There is probably no doubt that many new milestones, equally astonishing to the ones obtained so far, will be reached.

Chapter 7

Acknowledgements

Eight years have passed since I began my physics study at the Department of Physics and Astronomy at the University of Aarhus. It has been a long journey even though it feels like a very short time. Especially it has been an on-going pleasure take part in the building up of a whole new experimental activity and, of course, it has also been quite challenging. During my time as a PhD student, our laboratory has evolved from an empty room to a state of the art quantum gas laboratory. This would never had taken place without the initiative of my supervisor Michael Budde and I am grateful to him because he gave me the possibility to get involved into the project and because he guided me through many essential experimental procedures, especially in the initial phases of the project.

I am just as grateful to my second supervisor Klaus Mølmer who introduced me to the world of theory on ultracold atoms. Klaus has been a very inspiring source throughout my PhD study. He is really good at sharing his large experience and enthusiasm and he has always taken the time to talk with me even though he is very busy. One cannot help being influenced by his great commitment to physics and I have often left his office with a feeling that almost everything was possible.

I have also collaborated and become good friends with Henrik Kjaer Andersen. He joined the group as a bachelor student in 1999 and he continued as a PhD student in 2000. Henrik is very skilled as a computer programmer and he has also put a lot of effort into dealing with various technical problems in the laboratory which is part of the reason why it works so well today. The very complex yet still easy-to-use experimental control system he has built has been essential for the experiments I have done on mixing of ultracold atomic clouds in magnetic traps. I also want to thank him for valuable comments on and proof reading of most of this manuscript. Sune Mai also joined the group as a master student in 2006 and is now a PhD student. Sune is a very bright student and I am sure that he will make important contributions to the work in the quantum gas group.

From July to December 2006 I visited JILA at the University of Colorado to join one of the two K-Rb experiments in the group of Debbie Jin. I wish to thank all the people at JILA for making it such a nice place to work. My visit was very educational and I got quite a bit of experience in experimental troubleshooting. Especially I want to thank Debbie for giving me the opportunity to work in her group as well as Michele Olsen and Tylor Cumby whom I collaborated with on a daily basis. Also, I had some interesting discussions with Scott Papp who worked on the ^{85}Rb experiment in the group of Carl Wieman.

I have also collaborated with Simon Cornish's group at the university of Durham in England which I fortunately also had the chance to visit this spring. It was interesting to get the opportunity to perform calculations on their setup and it has also given me additional insight into the mixing process. I also thank both Simon, Patrick, Margaret and Ajay for their hospitality.

Throughout most of my undergraduate studies and part of my graduate studies I have had the pleasure to work together with Nikolaj Thomas Zinner who also began his physics study in 1999. Even if we are very different in many ways, the collaboration was very fruitful and I am sure that it has contributed significantly to make me the physicist I now am. I want to thank Nikolaj for several years of good cooperation and I wish him the best in his future career.

I also owe a lot to the many excellent lecturers at the physics and mathematics departments who have contributed substantially to my education in various ways: Ejvind Bonderup, Hans Fogedby, Aksel Jensen, Lars Bojer Madsen, and Axel Svane to mention but a few. I also wish to acknowledge help from Jens Lykke Sørensen, Nicolai Nygaard, and Uffe Vestergaard Poulsen who are bright assistant research professors at the department and I want to thank everyone in our neighboring laboratory, the ion trap group of Michael Drewsen, as well as all the theoreticians on the 6th floor, for being good colleagues.

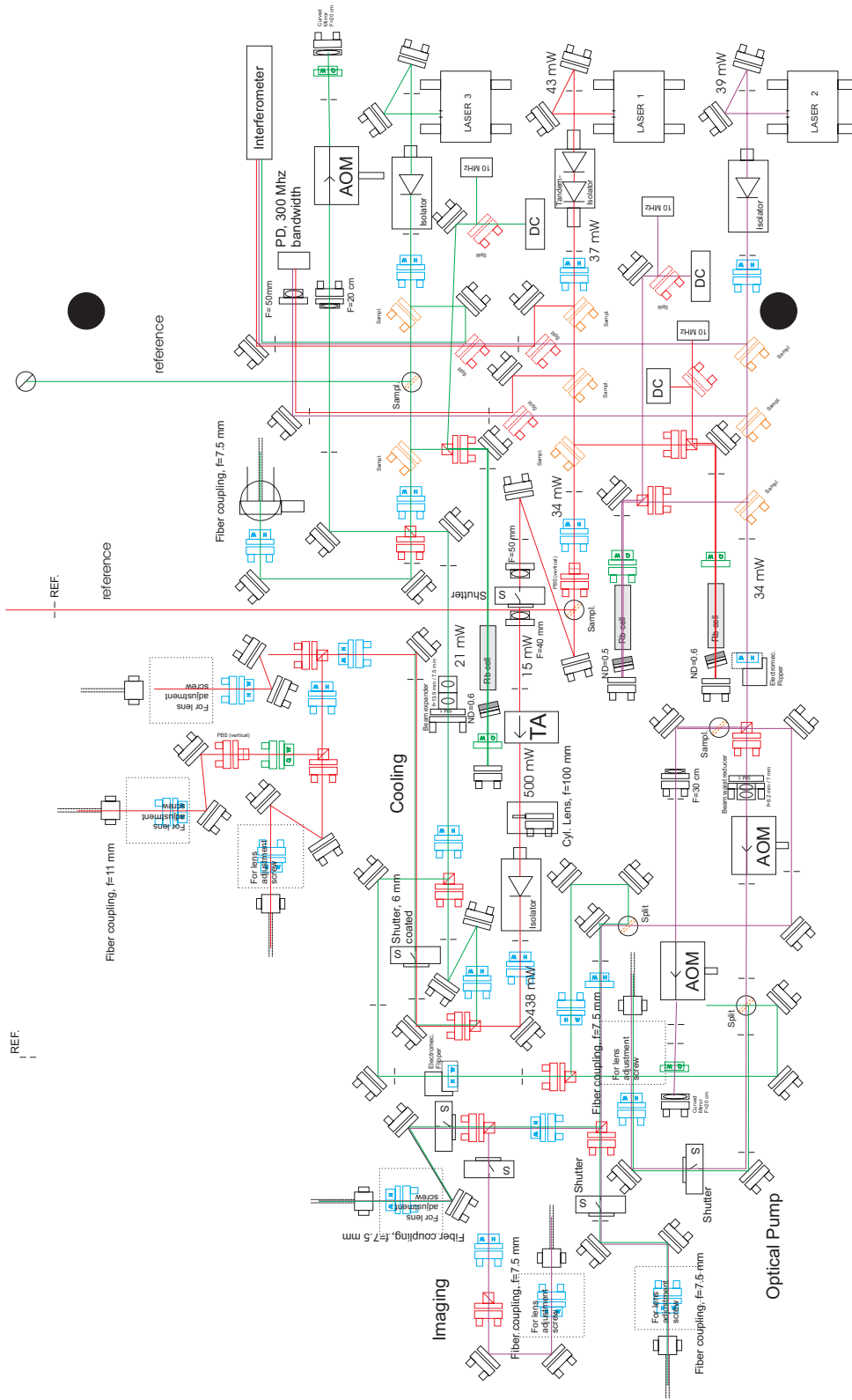
Finally, I do not want to underrate the importance of the work performed by technicians in the local workshops. In particular, Torben Hyltoft, Frank Mikkelsen, Erik Søndergaard, and Jens Vestergaard have been very helpful and it would have taken much more time to get the experiment up running without their help. I also want to thank our secretary Grete Flarup for always being helpful.

Of course, my deepest thank goes to my parents and my little sister for supporting me all the way through and for standing that I have often been quite busy.

Jesper

Appendix A

Appendix: Optical table
setup



Appendix B

Appendix: Two interacting particles in an external harmonic oscillator

Consider two interacting particles in an external harmonic oscillator. The general form of the potential energy is

$$V(\mathbf{r}_1, \mathbf{r}_2) = \frac{1}{2}m_1\omega_1^2r_1^2 + \frac{1}{2}m_2\omega_2^2r_2^2 + V_{\text{int}}(\mathbf{r}_1 - \mathbf{r}_2) \quad (\text{B.1})$$

In the case of noninteracting particles ($V_{\text{int}} = 0$) the Hamiltonian for this potential is just two separate harmonic oscillators in \mathbf{r}_1 and \mathbf{r}_2 . However, the interacting case $V_{\text{int}} \neq 0$ is much more complicated since the interaction potential acts on the relative coordinate $\mathbf{r} \equiv \mathbf{r}_1 - \mathbf{r}_2$.

To see the problem, let us say that we have found a coordinate $\mathbf{R}' = \mathbf{r}_1 + \gamma\mathbf{r}_2$ such that the potential separates:

$$V(\mathbf{r}, \mathbf{R}') = Ar^2 + BR'^2 + V_{\text{int}}(r) \quad (\text{B.2})$$

where A and B are constants. Let us then look at one of the Cartesian components of the kinetic part of the Hamiltonian - for instance the x component:

$$\frac{-\hbar^2}{2} \left(\frac{1}{m_1} \frac{\partial^2}{\partial x_1^2} + \frac{1}{m_2} \frac{\partial^2}{\partial x_2^2} \right) \quad (\text{B.3})$$

We want to rewrite this Hamiltonian as

$$\frac{-\hbar^2}{2} \left(\frac{1}{m} \frac{\partial^2}{\partial r_x^2} + \frac{1}{M'} \frac{\partial^2}{\partial R'_x{}^2} \right) \quad (\text{B.4})$$

where m and M' are two unknown mass constants. According to the chain rule, for the expressions (B.3) and (B.4) to be equal, we must have

$$\frac{1}{m_1} = \frac{1}{m} \left(\frac{\partial r_{1x}}{\partial r_x} \right)^2 + \frac{1}{M'} \left(\frac{\partial r_{1x}}{\partial R'_x} \right)^2 \quad (\text{B.5})$$

$$\frac{1}{m_2} = \frac{1}{m} \left(\frac{\partial r_{2x}}{\partial r_x} \right)^2 + \frac{1}{M'} \left(\frac{\partial r_{2x}}{\partial R'_x} \right)^2 \quad (\text{B.6})$$

$$0 = \frac{1}{m} \frac{\partial r_{1x}}{\partial r_x} \frac{\partial r_{2x}}{\partial r_x} + \frac{1}{M'} \frac{\partial r_{1x}}{\partial R'_x} \frac{\partial r_{2x}}{\partial R'_x} \quad (\text{B.7})$$

Since we have the transformation

$$\mathbf{r}_1 = \frac{\mathbf{R}' + \gamma \mathbf{r}}{1 + \gamma} \quad \mathbf{r}_2 = \frac{\mathbf{R}' - \mathbf{r}}{1 + \gamma} \quad (\text{B.8})$$

equation (B.7) reads

$$0 = \frac{-1}{m} \frac{\gamma}{(1 + \gamma)^2} + \frac{1}{M'} \frac{1}{(1 + \gamma)^2} \Rightarrow m = \gamma M' \quad (\text{B.9})$$

and equation (B.6) then gives

$$\frac{1}{m_2} = \frac{1}{\gamma M'} \frac{1}{(1 + \gamma)^2} + \frac{1}{M'} \frac{1}{(1 + \gamma)^2} \Rightarrow M' = \frac{m_2}{\gamma(1 + \gamma)} \quad (\text{B.10})$$

and from (B.5) we have, finally

$$\frac{1}{m_1} = \frac{1 + \gamma}{m_2} \left(\frac{\gamma}{1 + \gamma} \right)^2 + \frac{\gamma(1 + \gamma)}{m_2} \left(\frac{1}{1 + \gamma} \right)^2 \Rightarrow \gamma = \frac{m_2}{m_1}. \quad (\text{B.11})$$

So \mathbf{R}' has to be proportional to the center-of-mass (CM) coordinate. But since the relative and CM coordinates do not separate the potential part of the Hamiltonian in the general case (Eq. B.2 cannot be fulfilled), the problem cannot be separated through this linear coordinate transformation.

What we can do, however, is to introduce CM coordinate

$$\mathbf{R} = \frac{m_1 \mathbf{r}_1 + m_2 \mathbf{r}_2}{m_1 + m_2} \quad (\text{B.12})$$

and the total and reduced masses

$$M = m_1 + m_2 \quad \mu = \frac{m_1 m_2}{M} \quad (\text{B.13})$$

and rewrite the potential as

$$V(\mathbf{R}, \mathbf{r}) = \frac{1}{2} M \Omega^2 R^2 + \frac{1}{2} \mu \omega^2 r^2 + C \mathbf{R} \cdot \mathbf{r} + V_{\text{int}}(r) \quad (\text{B.14})$$

where, as we will show in the following,

$$\boxed{\frac{\Omega}{\omega_1} = \sqrt{\frac{1+\beta}{1+\alpha}}} \quad (\text{B.15})$$

$$\boxed{\frac{\omega}{\omega_1} = \sqrt{\frac{\alpha+\beta/\alpha}{1+\alpha}}} \quad (\text{B.16})$$

$$\boxed{\frac{C}{m_1\omega_1^2} = \frac{\alpha-\beta}{1+\alpha}} \quad (\text{B.17})$$

and we have introduced the the mass ratio $\alpha = m_2/m_1$ and the ratio between the depths of the two oscillators $\beta = m_2\omega_2^2/(m_1\omega_1^2)$. Notice that in the case $\omega_2 = \omega_1$ (that is, $\alpha = \beta$) we have $\Omega = \omega = \omega_1 = \omega_2$ and $C = 0$ so the CM and relative motion separate exactly. In the general case the two motions are coupled.

To show the above result we must solve the following equation for Ω , ω and C (the equation must be valid for all \mathbf{r}_1 and \mathbf{r}_2):

$$\frac{1}{2}m_1\omega_1^2r_1^2 + \frac{1}{2}m_2\omega_2^2r_2^2 = \frac{1}{2}M\Omega^2R^2 + \frac{1}{2}\mu\omega^2r^2 + C\mathbf{R} \cdot \mathbf{r} \quad (\text{B.18})$$

Dividing through by $(1/2)m_1\omega_1^2$ and introducing the dimensionless angular frequencies $\tilde{\Omega} \equiv \Omega/\omega_1$ and $\tilde{\omega} \equiv \omega/\omega_1$ we get

$$\begin{aligned} r_1^2 + \beta r_2^2 &= (\alpha+1)\tilde{\Omega}^2R^2 + \frac{\alpha}{\alpha+1}\tilde{\omega}^2r^2 + \frac{2C}{m_1\omega_1^2}\mathbf{R} \cdot \mathbf{r} \\ &= (\alpha+1)\tilde{\Omega}^2\left(\frac{\mathbf{r}_1 + \alpha\mathbf{r}_2}{\alpha+1}\right)^2 + \frac{\alpha}{\alpha+1}\tilde{\omega}^2(\mathbf{r}_1 - \mathbf{r}_2)^2 \\ &\quad + \frac{2C}{m_1\omega_1^2}\left(\frac{\mathbf{r}_1 + \alpha\mathbf{r}_2}{\alpha+1}\right) \cdot (\mathbf{r}_1 - \mathbf{r}_2) \\ &= \tilde{\Omega}^2\left(\frac{r_1^2 + \alpha^2r_2^2 + 2\alpha\mathbf{r}_1 \cdot \mathbf{r}_2}{\alpha+1}\right) + \frac{\alpha}{\alpha+1}\tilde{\omega}^2(r_1^2 + r_2^2 - 2\mathbf{r}_1 \cdot \mathbf{r}_2) \\ &\quad + \frac{2C}{m_1\omega_1^2}\frac{1}{\alpha+1}(r_1^2 - \alpha r_2^2 + (\alpha-1)(\mathbf{r}_1 \cdot \mathbf{r}_2)) \end{aligned} \quad (\text{B.19})$$

Gathering the coefficients of r_1^2 , r_2^2 and $\mathbf{r}_1 \cdot \mathbf{r}_2$ we get the following three

equations in the three unknowns $\tilde{\Omega}$, $\tilde{\omega}$ and C :

$$1 = \frac{1}{\alpha + 1} \tilde{\Omega}^2 + \frac{\alpha}{\alpha + 1} \tilde{\omega}^2 + \frac{2C}{m_1 \omega_1^2} \frac{1}{\alpha + 1} \quad (\text{B.20})$$

$$\beta = \frac{\alpha^2}{\alpha + 1} \tilde{\Omega}^2 + \frac{\alpha}{\alpha + 1} \tilde{\omega}^2 - \frac{2C}{m_1 \omega_1^2} \frac{\alpha}{\alpha + 1} \quad (\text{B.21})$$

$$\frac{2\alpha}{\alpha + 1} \tilde{\Omega}^2 - \frac{2\alpha}{\alpha + 1} \tilde{\omega}^2 + \frac{2C}{m_1 \omega_1^2} \frac{\alpha - 1}{\alpha + 1} = 0 \quad (\text{B.22})$$

which can be simplified to

$$\alpha + 1 = \tilde{\Omega}^2 + \alpha \tilde{\omega}^2 + \frac{2C}{m_1 \omega_1^2} \quad (\text{B.23})$$

$$\frac{\beta}{\alpha} (\alpha + 1) = \alpha \tilde{\Omega}^2 + \tilde{\omega}^2 - \frac{2C}{m_1 \omega_1^2} \quad (\text{B.24})$$

$$\frac{C}{m_1 \omega_1^2} = \frac{\alpha}{\alpha - 1} (\tilde{\omega}^2 - \tilde{\Omega}^2). \quad (\text{B.25})$$

Adding (B.23) and (B.24) gives

$$(\alpha + 1)(1 + \beta/\alpha) = (1 + \alpha) \tilde{\Omega}^2 + (\alpha + 1) \tilde{\omega}^2 \quad (\text{B.26})$$

or

$$\tilde{\omega}^2 = (1 + \beta/\alpha) - \tilde{\Omega}^2. \quad (\text{B.27})$$

Substituting (B.25) into (B.23) and using (B.27) now gives

$$\begin{aligned} \alpha + 1 &= \tilde{\Omega}^2 + \alpha \tilde{\omega}^2 + \frac{2\alpha}{\alpha - 1} (\tilde{\omega}^2 - \tilde{\Omega}^2) \\ &= \tilde{\Omega}^2 + (\alpha + \beta) - \alpha \tilde{\Omega}^2 + 2 \frac{\alpha + \beta}{\alpha - 1} - \frac{4\alpha}{\alpha - 1} \tilde{\Omega}^2 \\ &= \tilde{\Omega}^2 \left(1 - \alpha + \frac{4\alpha}{1 - \alpha} \right) + \left(\alpha + \beta - 2 \frac{\alpha + \beta}{1 - \alpha} \right) \end{aligned} \quad (\text{B.28})$$

leading to

$$\begin{aligned} \tilde{\Omega}^2 \frac{(1 + \alpha)^2}{1 - \alpha} &= 1 - \beta + 2 \frac{\alpha + \beta}{1 - \alpha} = \frac{1 - \alpha - \beta + \alpha\beta + 2\alpha + 2\beta}{1 - \alpha} \\ &= \frac{\alpha + 1 + \alpha\beta + \beta}{1 - \alpha} = \frac{(\alpha + 1)(\beta + 1)}{1 - \alpha} \end{aligned} \quad (\text{B.29})$$

so we finally arrive at

$$\tilde{\Omega}^2 = \frac{1 + \beta}{1 + \alpha} \quad (\text{B.30})$$

It is now easy to get $\tilde{\omega}$ from (B.27):

$$\tilde{\omega}^2 = 1 + \beta/\alpha - \frac{1 + \beta}{1 + \alpha} = \frac{\alpha + \beta + 1 + \beta/\alpha - 1 - \beta}{1 + \alpha} = \frac{\alpha + \beta/\alpha}{1 + \alpha} \quad (\text{B.31})$$

and C is given by (B.25).

Appendix C

Appendix: Calculation of matrix elements

This appendix summarizes how the matrix elements used in the Feshbach molecule problem can be calculated. There are two classes of wave functions in play: One is the wave functions for an isotropic 3-dimensional harmonic oscillator (see 4.38):

$$\Phi_{nlm}(\mathbf{r}) = R_{nl}(r)Y_{lm}(\theta, \phi) = N_{nl}L_n^{l+1/2}(r^2) r^l e^{-r^2/2} Y_{lm}(\theta, \phi) \quad (\text{C.1})$$

where L is a generalized Laguerre polynomial, $n = 0, 1, 2, \dots$ is the number of nodes in the radial wave function, l and m are the angular momentum quantum numbers, and N_{nl} is a normalization constant.

The other class is the parabolic cylinder wave functions which are the s-wave solutions to the problem of a particle in a harmonic oscillator modified by a regularized s-wave δ -function potential at the origin (see 4.52):

$$\varphi_\nu(\mathbf{r}) = R_\nu(r)Y_{00} = \frac{N_\nu}{r} 2^{-\nu-1/2} D_{2\nu+1}(z) Y_{00}, \quad z = \sqrt{2}r \quad (\text{C.2})$$

where D is the parabolic cylinder function and N_ν is a normalization constant.

We need the following three kinds of matrix elements

$$\langle \varphi_{\nu'} | \varphi_\nu \rangle \quad (\text{C.3})$$

$$\langle \Phi_{n'l'm'} | \mathbf{r} | \Phi_{nlm} \rangle \text{ and the normalization } \langle \Phi_{nlm} | \Phi_{nlm} \rangle \quad (\text{C.4})$$

$$\langle \Phi_{n1m} | \mathbf{r} | \varphi_\nu \rangle \quad (\text{C.5})$$

where (C.4) and (C.5) are only relevant in the case where the two atoms have different harmonic oscillator frequencies such that the relative and center-of-mass motions are coupled.

All the matrix elements separate into a radial factor and an angular factor. For the wave functions $\psi'(r, \Omega) = R'(r)Y_{l'm'}(\Omega)$ and $\psi(r, \Omega) = R(r)Y_{lm}(\Omega)$, the dipole matrix element becomes

$$\langle \psi' | \mathbf{r} | \psi \rangle = \int_0^\infty R'(r)^* r R(r) r^2 dr \int Y_{l'm'}(\Omega)^* \hat{\mathbf{r}} Y_{lm}(\Omega) d\Omega \quad (\text{C.6})$$

where $\hat{\mathbf{r}}$ is the unit vector \mathbf{r}/r and (Ω) is used as short for (θ, ϕ) .

C.1 The angular integral

The angular integral in (C.6) is the same as the angular integral for dipole transitions in any other spherically symmetric potential, e.g. radiative dipole transitions in the hydrogen atom which are treated in many atomic physics books, e.g. [162]. The problem is most easily dealt with by using the spherical components of $\hat{\mathbf{r}}$ ([162] 4.110-4.111):

$$\hat{\mathbf{r}}_0 = \hat{\mathbf{r}}_z = \sqrt{\frac{4\pi}{3}} Y_{10}(\Omega) \quad (\text{C.7})$$

$$\hat{\mathbf{r}}_{\pm 1} = \mp \frac{1}{\sqrt{2}} (\hat{\mathbf{r}}_x \pm i \hat{\mathbf{r}}_y) = \sqrt{\frac{4\pi}{3}} Y_{1\pm 1}(\Omega) \quad (\text{C.8})$$

so

$$\int Y_{l'm'}(\Omega)^* \hat{\mathbf{r}}_q Y_{lm}(\Omega) d\Omega = \sqrt{\frac{4\pi}{3}} \int Y_{l'm'}^*(\Omega) Y_{1q}(\Omega) Y_{lm}(\Omega) d\Omega \quad (\text{C.9})$$

By looking at the ϕ -components of this integral, one sees that we have the selection rule $m' = m + q$. Furthermore it follows from the Wigner-Eckart theorem and parity considerations that we also have the selection rule $|l' - l| = 1$. Explicit formulas for the integral are given in [162] (solution to problem 4.6 in A 13):

$$\sqrt{\frac{4\pi}{3}} \int Y_{l'm}(\Omega)^* \hat{\mathbf{r}}_0 Y_{lm}(\Omega) d\Omega = \begin{cases} \sqrt{\frac{(l+1)^2 - m^2}{(2l+1)(2l+3)}} & l' = l + 1 \\ \sqrt{\frac{l^2 - m^2}{(2l-1)(2l+1)}} & l' = l - 1 \end{cases} \quad (\text{C.10})$$

$$\sqrt{\frac{4\pi}{3}} \int Y_{l'(m\pm 1)}(\Omega)^* \hat{\mathbf{r}}_{\pm 1} Y_{lm}(\Omega) d\Omega = \begin{cases} \sqrt{\frac{(l\pm m+1)(l\pm m+2)}{2(2l+1)(2l+3)}} & l' = l + 1 \\ -\sqrt{\frac{(l\mp m)(l\mp m-1)}{2(2l-1)(2l+1)}} & l' = l - 1 \end{cases} \quad (\text{C.11})$$

To calculate the scalar product $\langle \psi'(\mathbf{R}) | \mathbf{R} | \psi(\mathbf{R}) \rangle \cdot \langle \varphi'(\mathbf{r}) | \mathbf{r} | \varphi(\mathbf{r}) \rangle$ we use

$$\mathbf{R} \cdot \mathbf{r} = \sum_{i=x,y,z} R_i r_i = \sum_{q=-1}^1 R_q^* r_q \quad (\text{C.12})$$

so

$$\begin{aligned} & \langle \psi'(\mathbf{R}) | \mathbf{R} | \psi(\mathbf{R}) \rangle \cdot \langle \varphi'(\mathbf{r}) | \mathbf{r} | \varphi(\mathbf{r}) \rangle \\ &= \sum_{q=-1}^1 \langle \psi'(\mathbf{R}) | R \hat{R}_q^* | \psi(\mathbf{R}) \rangle \langle \varphi'(\mathbf{r}) | r \hat{r}_q | \varphi(\mathbf{r}) \rangle \end{aligned} \quad (\text{C.13})$$

$$= \sum_{q=-1}^1 \langle \psi(\mathbf{R}) | R \hat{R}_q | \psi'(\mathbf{R}) \rangle^* \langle \varphi'(\mathbf{r}) | r \hat{r}_q | \varphi(\mathbf{r}) \rangle. \quad (\text{C.14})$$

C.2 The overlap of two parabolic cylinder wave functions

The normalization constant of the parabolic cylinder wave functions (C.2) is given by

$$\frac{1}{N_\nu^2} = \int_0^\infty R_\nu(r)^2 r^2 dr = 2^{-2\nu-1} \int_0^\infty [D_{2\nu+1}(z)]^2 \frac{dz}{\sqrt{2}} \quad (\text{C.15})$$

$$= 2^{-2\nu-3} \sqrt{\pi} \frac{\psi(-\nu) - \psi(-\nu - 1/2)}{\Gamma(-2\nu - 1)} \quad (\text{C.16})$$

$$= \frac{\pi}{2} \frac{\psi(-\nu) - \psi(-\nu - 1/2)}{\Gamma(-\nu - 1/2)\Gamma(-\nu)} \quad (\text{C.17})$$

where [163] 7.711 has been used to solve the integral and the duplication formula for gamma functions [146] 6.1.18 has been used in the last equality. ψ is the digamma function:

$$\psi(x) = \frac{d}{dx} \ln \Gamma(x) = \frac{\Gamma'(x)}{\Gamma(x)}. \quad (\text{C.18})$$

Matlab has a built-in procedure to calculate the digamma function of positive arguments. For negative arguments the following reflection formula ([146] 6.3.7) can be used:

$$\psi(1-x) = \psi(x) + \pi \cot \pi x \quad (\text{C.19})$$

In the case $\nu' \neq \nu$ the overlap integral (C.3) is

$$\begin{aligned} \langle \varphi_{\nu'} | \varphi_\nu \rangle &= N_{\nu'} N_\nu 2^{-\nu' - \nu - 1} \int_0^\infty D_{2\nu'+1}(z) D_{2\nu+1}(z) \frac{dz}{\sqrt{2}} \\ &= N_{\nu'} N_\nu \frac{\pi}{2(\nu' - \nu)} \left[\frac{1}{\Gamma(-\nu')\Gamma(-\nu - 1/2)} - \frac{1}{\Gamma(-\nu)\Gamma(-\nu' - 1/2)} \right]. \end{aligned} \quad (\text{C.20})$$

Here again [163] 7.711 has been used to solve the integral. Putting in the values of the normalization constants from (C.17) we arrive at the following expression which I use in the numerical computations

$$\langle \varphi_{\nu'} | \varphi_{\nu} \rangle = \frac{f(\nu')f(\nu)}{\nu - \nu'} \times \frac{\Gamma(-\nu')\Gamma(-\nu - \frac{1}{2}) - \Gamma(-\nu)\Gamma(-\nu' - \frac{1}{2})}{\sqrt{\Gamma(-\nu' - \frac{1}{2})\Gamma(-\nu')} \sqrt{\Gamma(-\nu - \frac{1}{2})\Gamma(-\nu)}} \quad (\text{C.21})$$

where

$$f(\nu) = \frac{1}{\sqrt{\psi(-\nu) - \psi(-\nu - \frac{1}{2})}}. \quad (\text{C.22})$$

C.3 The radial integral for harmonic oscillator wave functions

The normalization constant of the harmonic oscillator wave functions is given by

$$\frac{1}{N_{nl}^2} = \int_0^{\infty} \left[L_n^{l+1/2}(r^2) \right]^2 r^{2l+2} e^{-r^2} dr \quad (\text{C.23})$$

$$= \frac{1}{2} \int_0^{\infty} \left[L_n^{l+1/2}(u) \right]^2 u^{l+1/2} e^{-u} du \quad (\text{C.24})$$

$$= \frac{\Gamma(n + l + 3/2)}{2n!} \quad (\text{C.25})$$

where the orthogonality relation for the generalized Laguerre polynomials has been used in the last step ([146] 22.2.12, [163] 7.414.3):

$$\int_0^{\infty} e^{-x} x^{\alpha} L_n^{\alpha}(x) L_m^{\alpha}(x) dx = \begin{cases} \frac{\Gamma(\alpha+n+1)}{n!}, & m = n, \text{Re } \alpha > 0 \\ 0, & m \neq n, \text{Re } \alpha > -1 \end{cases} \quad (\text{C.26})$$

The radial part of the dipole matrix element in (C.4) has the form

$$\int_0^{\infty} L_{n'}^{l'+1/2}(r^2) L_n^{l+1/2}(r^2) r^{l'+l+3} e^{-r^2} dr \quad (\text{C.27})$$

$$= \frac{1}{2} \int_0^{\infty} L_{n'}^{l'+1/2}(u) L_n^{l+1/2}(u) u^{(l'+l+2)/2} e^{-u} du \quad (\text{C.28})$$

This is just an integral of a polynomial times an exponential function and can always be integrated term by term. However, since the angular integral has the selection rule $|\Delta l| = 1$ (see section C.1) we can, without

loss of generality, assume that $l' = l + 1$ and employ the following simple recursion relation for the generalized Laguerre polynomials ([146] 22.7.30):

$$L_n^{\alpha-1}(u) = L_n^\alpha(u) - L_{n-1}^\alpha(u) \quad (\text{C.29})$$

to obtain

$$\frac{1}{2} \int_0^\infty L_{n'}^{l'+1/2}(u) L_n^{l+1/2}(u) u^{(l'+l+2)/2} e^{-u} du \quad (\text{C.30})$$

$$= \frac{1}{2} \int_0^\infty L_{n'}^{l+3/2}(u) L_n^{l+1/2}(u) u^{(2l+3)/2} e^{-u} du \quad (\text{C.31})$$

$$= \frac{1}{2} \int_0^\infty L_{n'}^{l+3/2}(u) \left(L_n^{l+3/2}(u) - L_{n-1}^{l+3/2}(u) \right) u^{(2l+3)/2} e^{-u} du \quad (\text{C.32})$$

$$= \frac{1}{2} \frac{\Gamma(n' + l + 5/2)}{(n')!} (\delta_{n',n} - \delta_{n',n-1}) \quad (\text{C.33})$$

where δ is the Kronecker delta. The orthogonality relation (C.26) has been used to get the last equality. So we have the selection rule $n' = n$ or $n' = n - 1$ where we recall that n' is the principal quantum number for the state with highest l . Putting in the normalization (C.25) we finally obtain

$$\int_0^\infty R_{n',l+1}(r) r R_{n,l}(r) r^2 dr = \sqrt{\frac{\Gamma(n' + l + 5/2)}{\Gamma(n + l + 3/2)} \frac{n!}{(n')!}} (\delta_{n',n} - \delta_{n',n-1}) \quad (\text{C.34})$$

$$= \sqrt{n + l + 3/2} \delta_{n',n} - \sqrt{n} \delta_{n',n-1} \quad (\text{C.35})$$

where the identity $\Gamma(x + 1) = x \Gamma(x)$ has been used.

C.4 Matrix element with parabolic cylinder and harm. osc. functions

For the matrix element (C.5) the radial integral is

$$\begin{aligned} & \int_0^\infty R_\nu(r) R_{n_1}(r) r^3 dr \\ &= \int_0^\infty \left[\frac{N_\nu}{r} 2^{-\nu-1/2} D_{2\nu+1}(z) \right] \left[N_{n_1} L_n^{3/2}(r^2) r e^{-r^2/2} \right] r^3 dr, \quad z^2 = 2r^2 \\ &= N_\nu N_{n_1} 2^{-\nu-1/2} \int_0^\infty D_{2\nu+1}(z) L_n^{3/2}(r^2) r^3 e^{-r^2/2} dr, \quad z^2 = 2r^2 \\ &= N_\nu N_{n_1} 2^{-\nu-1/2} \int_0^\infty D_{2\nu+1}(z) L_n^{3/2}(z^2/2) \frac{z^3}{2^{3/2}} e^{-z^2/4} \frac{dz}{\sqrt{2}}. \end{aligned} \quad (\text{C.36})$$

The generalized Laguerre polynomials are given by ([146] 22.3.9)

$$L_n^\alpha(u) = \sum_{k=0}^n a_k u^k, \quad a_k = (-1)^k \binom{n+\alpha}{n-k} \frac{1}{k!} \quad (\text{C.37})$$

so we can integrate the expression term by term

$$\int_0^\infty R_\nu(r) R_{n1}(r) r^3 dr \quad (\text{C.38})$$

$$= N_\nu N_{n1} 2^{-\nu-5/2} \sum_{k=0}^n a_k \int_0^\infty D_{2\nu+1}(z) \left(\frac{1}{2}z^2\right)^k z^3 e^{-z^2/4} dz \quad (\text{C.39})$$

$$= N_\nu N_{n1} \sum_{k=0}^n 2^{-\nu-5/2-k} a_k \int_0^\infty D_{2\nu+1}(z) z^{2k+3} e^{-z^2/4} dz. \quad (\text{C.40})$$

Even this integral can be calculated thanks to [163] 7.722 which states

$$\int_0^\infty e^{-x^2/4} x^{\mu-1} D_{-\tilde{\nu}}(x) dx = \frac{\sqrt{\pi} 2^{-\mu/2-\tilde{\nu}/2} \Gamma(\mu)}{\Gamma(\mu/2 + \tilde{\nu}/2 + 1/2)}, \quad \mu > 0 \quad (\text{C.41})$$

or with $\tilde{\nu} = -(2\nu + 1)$

$$\int_0^\infty e^{-x^2/4} x^{\mu-1} D_{2\nu+1}(x) dx = \frac{\sqrt{\pi} 2^{-\mu/2+\nu+1/2} \Gamma(\mu)}{\Gamma(\mu/2 - \nu)}, \quad \mu > 0 \quad (\text{C.42})$$

so we arrive at

$$\begin{aligned} & \int_0^\infty R_\nu(r) R_{n1}(r) r^3 dr \\ &= N_\nu N_{n1} \sum_{k=0}^n 2^{-\nu-5/2-k} a_k \sqrt{\pi} 2^{-k+\nu-3/2} \frac{\Gamma(2k+4)}{\Gamma(k+2-\nu)} \\ &= N_\nu N_{n1} \frac{\sqrt{\pi}}{16} \sum_{k=0}^n 2^{-2k} a_k \frac{\Gamma(2k+4)}{\Gamma(k+2-\nu)} \\ &= N_\nu N_{n1} \frac{\sqrt{\pi}}{16} \sum_{k=0}^n 2^{-2k} (-1)^k \binom{n+\alpha}{n-k} \frac{1}{k!} \frac{\Gamma(2k+4)}{\Gamma(k+2-\nu)} \end{aligned} \quad (\text{C.43})$$

where we have put in the value of the coefficient a_k in the last step.

Appendix D

List of abbreviations

1D	one-dimensional
2D	two-dimensional
3D	three-dimensional
AOM	acousto-optical modulator
Arxiv	http://www.arxiv.org/abs/
BCKGRD	image of background light
BEC	Bose-Einstein condensate
CCD	charge-coupled device
Ch.	chapter
CM	center-of-mass
CMOT	compressed magneto-optical trap
Eq.	equation
Fig.	figure
Figs.	figures
FWHM	full width at half maximum
HW	half-wave plate
HWHM	half width at half maximum
MOT	magneto-optical trap
PBS	polarizing beam-splitter cube
PD	photo detector
Phys. Rev.	Physical Review
Phys. Rev. Lett.	Physical Review Letters
QP	quadrupole
QUIC	quadrupole-Ioffe configuration
QW	quarter-wave plate
RAW	raw image
REF	reference image
RF	radio frequency
Sec.	section
TA	tapered amplifier
Tab.	table

Bibliography

- [1] J. F. Bertelsen, H. K. Andersen, S. Mai, and M. Budde, “Mixing of ultracold atomic clouds by merging of two magnetic traps”, *Phys. Rev. A* **75**, 013404 (2007).
- [2] J. F. Bertelsen and K. Mølmer, “Molecule formation in optical lattice wells by resonantly modulated magnetic fields”, *Phys. Rev. A* **73**, 013811 (2006).
- [3] J. F. Bertelsen and K. Mølmer, “Association of heteronuclear molecules in a harmonic oscillator well”, *e-print: Arxiv* 0706.4218 (Accepted for publication in *Phys. Rev. A*) (2007).
- [4] W. Ketterle, D. Durfee, and D. Stamper-Kurn, “Making, probing and understanding Bose-Einstein condensates (contribution to [14])”, *e-print: Arxiv cond-mat/9904034v2* (1999).
- [5] C. J. Pethick and H. Smith, *Bose-Einstein Condensation in Dilute Gases* (Cambridge University Press, Cambridge, 2002).
- [6] F. Mandl, *Statistical Physics*, 2nd ed. (John Wiley & Sons Ltd., Chichester, 1988).
- [7] N. W. Ashcroft and N. D. Mermin, *Solid State Physics* (Thomson Learning, US, 1976).
- [8] P. A. Martin and F. Rothen, *Many-Body Problems and Quantum Field Theory, An Introduction* (Springer, Berlin-Heidelberg, 2002).
- [9] M. H. Anderson, J. R. Ensher, M. R. Matthews, C. E. Wieman, and E. A. Cornell, “Observation of Bose-Einstein Condensation in a Dilute Atomic Vapor”, *Science* **269**, 198 (1995).
- [10] E. A. Cornell and C. E. Wieman, “Nobel Lecture: Bose-Einstein condensation in a dilute gas, the first 70 years and some recent experiments”, *Rev. Mod. Phys.* **74**, 875 (2002).

- [11] K. B. Davis, M. O. Mewes, M. R. Andrews, N. J. van Druten, D. S. Durfee, D. M. Kurn, and W. Ketterle, “Bose-Einstein Condensation in a Gas of Sodium Atoms”, *Phys. Rev. Lett.* **75**, 3969 (1995).
- [12] W. Ketterle, “Nobel lecture: When atoms behave as waves: Bose-Einstein condensation and the atom laser”, *Rev. Mod. Phys.* **74**, 1131 (2002).
- [13] L. Pitaevskii and S. Stringari, *Bose-Einstein Condensation* (Oxford University Press, New York, 2003).
- [14] M. Inguscio (Editor), S. Stringari (Editor), and C. Wieman (Editor), *Bose-Einstein Condensation in Atomic Gases* (IOS Press, Amsterdam, 1999).
- [15] C. C. Bradley, C. A. Sackett, and R. G. Hulet, “Bose-Einstein Condensation of Lithium: Observation of Limited Condensate Number”, *Phys. Rev. Lett.* **78**, 985 (1997).
- [16] G. Roati, M. Zaccanti, C. D’Errico, J. Catani, M. Modugno, A. Simoni, M. Inguscio, and G. Modugno, “³⁹K Bose-Einstein Condensate with Tunable Interactions”, *Phys. Rev. Lett.* **99**, 010403 (2007).
- [17] G. Modugno, G. Ferrari, G. Roati, R. J. Brecha, A. Simoni, and M. Inguscio, “Bose-Einstein Condensation of Potassium Atoms by Sympathetic Cooling”, *Science* **294**, 1320 (2001).
- [18] S. L. Cornish, N. R. Claussen, J. L. Roberts, E. A. Cornell, and C. E. Wieman, “Stable ⁸⁵Rb Bose-Einstein Condensates with Widely Tunable Interactions”, *Phys. Rev. Lett.* **85**, 1795 (2000).
- [19] T. Weber, J. Herbig, M. Mark, H.-C. Nägerl, and R. Grimm, “Bose-Einstein Condensation of Cesium”, *Science* **299**, 232 (2003).
- [20] A. Robert, O. Sirjean, A. Browaeys, J. Poupard, S. Nowak, D. Biron, C. I. Westbrook, and A. Aspect, “A Bose-Einstein Condensate of Metastable Atoms”, *Science* **292**, 461 (2001).
- [21] F. Pereira Dos Santos, J. Léonard, J. Wang, C. J. Barrelet, F. Perales, E. Rasel, C. S. Unnikrishnan, M. Leduc, and C. Cohen-Tannoudji, “Bose-Einstein Condensation of Metastable Helium”, *Phys. Rev. Lett.* **86**, 3459 (2001).
- [22] D. G. Fried, T. C. Killian, L. Willmann, D. Landhuis, S. C. Moss, D. Kleppner, and T. J. Greytak, “Bose-Einstein Condensation of Atomic Hydrogen”, *Phys. Rev. Lett.* **81**, 3811 (1998).

- [23] A. Griesmaier, J. Werner, S. Hensler, J. Stuhler, and T. Pfau, “Bose-Einstein Condensation of Chromium”, *Phys. Rev. Lett.* **94**, 160401 (2005).
- [24] F. Gerbier, J. H. Thywissen, S. Richard, M. Hugbart, P. Bouyer, and A. Aspect, “Experimental study of the thermodynamics of an interacting trapped Bose-Einstein condensed gas”, *Phys. Rev. A* **70**, 013607 (2004).
- [25] H. J. Lewandowski, D. M. Harber, D. L. Whitaker, and E. A. Cornell, “Simplified System for Creating a Bose-Einstein Condensate”, *Journal of Low Temperature Physics* **132**, 309 (2003).
- [26] K. Dieckmann, Ph.D. thesis, University of Amsterdam, 2001.
- [27] I. Bloch, J. Dalibard, and W. Zwerger, “Many-Body Physics with Ultracold Gases”, *e-print: Arxiv* 0704.3011 (2007).
- [28] B. DeMarco and D. S. Jin, “Onset of Fermi Degeneracy in a Trapped Atomic Gas”, *Science* **285**, 1703 (1999).
- [29] K. Mølmer, “Bose Condensates and Fermi Gases at Zero Temperature”, *Phys. Rev. Lett.* **80**, 1804 (1998).
- [30] L. Viverit, C. J. Pethick, and H. Smith, “Zero-temperature phase diagram of binary boson-fermion mixtures”, *Phys. Rev. A* **61**, 053605 (2000).
- [31] M. Zaccanti, C. D’Errico, F. Ferlaino, G. Roati, M. Inguscio, and G. Modugno, “Control of the interaction in a Fermi-Bose mixture”, *Phys. Rev. A* **74**, 041605 (2006).
- [32] S. Ospelkaus, C. Ospelkaus, L. Humbert, K. Sengstock, and K. Bongs, “Tuning of Heteronuclear Interactions in a Degenerate Fermi-Bose Mixture”, *Phys. Rev. Lett.* **97**, 120403 (2006).
- [33] V. Ahufinger, L. Sanchez-Palencia, A. Kantian, A. Sanpera, and M. Lewenstein, “Disordered ultracold atomic gases in optical lattices: A case study of Fermi-Bose mixtures”, *Phys. Rev. A* **72**, 063616 (2005).
- [34] M. Lewenstein, A. Sanpera, V. Ahufinger, B. Damski, A. Sen, and U. Sen, “Ultracold atomic gases in optical lattices: mimicking condensed matter physics and beyond”, *Advances in Physics* **56**, 243 (2007).
- [35] L. Santos, G. V. Shlyapnikov, P. Zoller, and M. Lewenstein, “Bose-Einstein Condensation in Trapped Dipolar Gases”, *Phys. Rev. Lett.* **85**, 1791 (2000).

- [36] K. Góral, K. Rzażewski, and T. Pfau, “Bose-Einstein condensation with magnetic dipole-dipole forces”, *Phys. Rev. A* **61**, 051601 (2000).
- [37] M. G. Kozlov and D. DeMille, “Enhancement of the Electric Dipole Moment of the Electron in PbO”, *Phys. Rev. Lett.* **89**, 133001 (2002).
- [38] D. DeMille, “Quantum Computation with Trapped Polar Molecules”, *Phys. Rev. Lett.* **88**, 067901 (2002).
- [39] A. Micheli, G. K. Brennen, and P. Zoller, “A toolbox for lattice-spin models with polar molecules”, *Nature Physics* **2**, 341 (2006).
- [40] R. A. Nyman, G. Varoquaux, B. Villier, D. Sacchet, F. Moron, Y. L. Coq, A. Aspect, and P. Bouyer, “Tapered-amplified antireflection-coated laser diodes for potassium and rubidium atomic-physics experiments”, *Review of Scientific Instruments* **77**, 033105 (2006).
- [41] J. Goldwin, S. B. Papp, B. DeMarco, and D. S. Jin, “Two-species magneto-optical trap with ^{40}K and ^{87}Rb ”, *Phys. Rev. A* **65**, 021402 (2002).
- [42] J. Goldwin, S. Inouye, M. L. Olsen, B. Newman, B. D. DePaola, and D. S. Jin, “Measurement of the interaction strength in a Bose-Fermi mixture with ^{87}Rb and ^{40}K ”, *Phys. Rev. A* **70**, 021601 (2004).
- [43] S. B. Papp and C. E. Wieman, “Observation of Heteronuclear Feshbach Molecules from a ^{85}Rb - ^{87}Rb Gas”, *Phys. Rev. Lett.* **97**, 180404 (2006).
- [44] C. Marzok, B. Deh, P. Courteille, and Z. C., “Ultracold Thermalization of ^7Li and ^{87}Rb ”, *e-print: Arxiv* 0705.2750 (2007).
- [45] A. Mosk, S. Kraft, M. Mudrich, K. Singer, W. Wohlleben, R. Grimm, and M. Weidemüller, “Mixture of ultracold lithium and cesium atoms in an optical dipole trap”, *Appl. Phys. B* **73**, 791 (2001).
- [46] J. P. Shaffer, W. Chalupczak, and N. P. Bigelow, “Trap loss in a two-species Na-Cs magneto-optical trap: Intramultiplet mixing in heteronuclear ultracold collisions”, *Phys. Rev. A* **60**, R3365 (1999).
- [47] C. Haimberger, J. Kleinert, M. Bhattacharya, and N. P. Bigelow, “Formation and detection of ultracold ground-state polar molecules”, *Phys. Rev. A* **70**, 021402 (2004).
- [48] J. M. Sage, S. Sainis, T. Bergeman, and D. DeMille, “Optical Production of Ultracold Polar Molecules”, *Phys. Rev. Lett.* **94**, 203001 (2005).

- [49] M. W. Mancini, G. D. Telles, A. R. L. Caires, V. S. Bagnato, and L. G. Marcassa, “Observation of Ultracold Ground-State Heteronuclear Molecules”, *Phys. Rev. Lett.* **92**, 133203 (2004).
- [50] S. D. Kraft, P. Staantum, J. Lange, L. Vogel, R. Wester, and M. Weidemüller, “Formation of ultracold LiCs molecules”, *Journal of Physics B* **39**, S993 (2006).
- [51] S. Hensler, A. Griesmaier, J. Werner, A. Görlitz, and T. Pfau, “A two species trap for chromium and rubidium atoms”, *Journal of Modern Optics* **51**, 1807 (2004).
- [52] R. Chicireanu, A. Pouderous, R. Barbe, B. Laburthe-Tolra, E. Marechal, L. Vernac, J.-C. Keller, and O. Gorceix, “Simultaneous magneto-optical trapping of bosonic and fermionic chromium atoms”, *Phys. Rev. A* **73**, 053406 (2006).
- [53] G. Roati, F. Riboli, G. Modugno, and M. Inguscio, “Fermi-Bose Quantum Degenerate ^{40}K - ^{87}Rb Mixture with Attractive Interaction”, *Phys. Rev. Lett.* **89**, 150403 (2002).
- [54] J. Goldwin, S. Inouye, M. L. Olsen, B. Newman, B. D. DePaola, and D. S. Jin, “Measurement of the interaction strength in a Bose-Fermi mixture with ^{87}Rb and ^{40}K ”, *Phys. Rev. A* **70**, 021601 (2004).
- [55] S. Ospelkaus, C. Ospelkaus, L. Humbert, K. Sengstock, and K. Bongs, “Tuning of Heteronuclear Interactions in a Degenerate Fermi-Bose Mixture”, *Phys. Rev. Lett.* **97**, 120403 (2006).
- [56] C. Silber, S. Gunther, C. Marzok, B. Deh, P. W. Courteille, and C. Zimmermann, “Quantum-Degenerate Mixture of Fermionic Lithium and Bosonic Rubidium Gases”, *Phys. Rev. Lett.* **95**, 170408 (2005).
- [57] I. Bloch, M. Greiner, O. Mandel, T. W. Hänsch, and T. Esslinger, “Sympathetic cooling of ^{85}Rb and ^{87}Rb ”, *Phys. Rev. A* **64**, 021402 (2001).
- [58] Z. Hadzibabic, C. A. Stan, K. Dieckmann, S. Gupta, M. W. Zwierlein, A. Görlitz, and W. Ketterle, “Two-Species Mixture of Quantum Degenerate Bose and Fermi Gases”, *Phys. Rev. Lett.* **88**, 160401 (2002).
- [59] A. G. Truscott, K. E. Strecker, W. I. McAlexander, G. B. Partridge, and R. G. Hulet, “Observation of Fermi Pressure in a Gas of Trapped Atoms”, *Science* **291**, 2570 (2001).
- [60] F. Schreck, L. Khaykovich, K. L. Corwin, G. Ferrari, T. Bourdel, J. Cubizolles, and C. Salomon, “Quasipure Bose-Einstein Condensate Immersed in a Fermi Sea”, *Phys. Rev. Lett.* **87**, 080403 (2001).

- [61] J. M. McNamara, T. Jelten, A. S. Tychkov, W. Hogervorst, and W. Vassen, “Degenerate Bose-Fermi Mixture of Metastable Atoms”, *Phys. Rev. Lett.* **97**, 080404 (2006).
- [62] U. Schlöder, H. Engler, U. Schünemann, R. Grimm, and M. Weidemüller, “Cold inelastic collisions between lithium and cesium in a two-species magneto-optical trap”, *European Physical Journal D* **7**, 331 (1999).
- [63] M. Taglieber, A.-C. Voigt, F. Henkel, S. Fray, T. W. Hänsch, and K. Dieckmann, “Simultaneous magneto-optical trapping of three atomic species”, *Phys. Rev. A* **73**, 011402 (2006).
- [64] G. Auböck, C. Binder, L. Holler, V. Wippel, K. Rumpf, J. Szczepkowski, W. E. Ernst, and L. Windholz, “Trap loss collisions of ^6Li and ^7Li with ^{23}Na in a combined magneto-optical trap”, *Journal of Physics B* **39**, S871 (2006).
- [65] R. Grimm, M. Weidemüller, and Y. B. Ovchinnikov, “Optical dipole traps for neutral atoms”, *Advances in Atomic Molecular, and Optical Physics* **42**, 95 (2000).
- [66] D. Jaksch, C. Bruder, J. I. Cirac, C. W. Gardiner, and P. Zoller, “Cold Bosonic Atoms in Optical Lattices”, *Phys. Rev. Lett.* **81**, 3108 (1998).
- [67] M. Greiner, O. Mandel, T. Esslinger, T. W. Hänsch, and I. Bloch, “Quantum phase transition from a superfluid to a Mott insulator in a gas of ultracold atoms”, *Nature* **415**, 39 (2002).
- [68] J. H. Denschlag, J. E. Simsarian, H. Haffner, C. McKenzie, A. Browaeys, D. Cho, K. Helmerson, S. L. Rolston, and W. D. Phillips, “A Bose-Einstein condensate in an optical lattice”, *Journal of Physics B-Atomic Molecular and Optical Physics* **35**, 3095 (2002).
- [69] O. Morsch and M. Oberthaler, “Dynamics of Bose-Einstein condensates in optical lattices”, *Reviews of Modern Physics* **78**, 179 (2006).
- [70] M. Olshanii, “Atomic Scattering in the Presence of an External Confinement and a Gas of Impenetrable Bosons”, *Phys. Rev. Lett.* **81**, 938 (1998).
- [71] B. Paredes, A. Widera, V. Murg, O. Mandel, S. Fölling, I. Cirac, G. V. Shlyapnikov, T. W. Hänsch, and I. Bloch, “Tonks-Girardeau gas of ultracold atoms in an optical lattice”, *Nature* **429**, 277 (2004).
- [72] S. Ospelkaus, C. Ospelkaus, O. Wille, M. Succo, P. Ernst, K. Sengstock, and K. Bongs, “Localization of Bosonic Atoms by Fermionic Impurities in a Three-Dimensional Optical Lattice”, *Phys. Rev. Lett.* **96**, 180403 (2006).

- [73] J. J. Sakurai, *Modern Quantum Mechanics*, revised ed. (Addison Wesley Longman, US, 1994).
- [74] T. Köhler, K. Góral, and P. S. Julienne, “Production of cold molecules via magnetically tunable Feshbach resonances”, *Reviews of Modern Physics* **78**, 1311 (2006).
- [75] D. J. Griffiths, *Introduction to Quantum Mechanics* (Prentice Hall, New Jersey, 1995).
- [76] S. Gasiorowicz, *Quantum Physics*, 2nd ed. (John Wiley & Sons, New York, 1996).
- [77] A. Messiah, *Quantum Mechanics, Vol. 1* (North-Holland Publishing Company, Amsterdam, 1961).
- [78] A. J. Moerdijk, B. J. Verhaar, and A. Axelsson, “Resonances in ultracold collisions of ${}^6\text{Li}$, ${}^7\text{Li}$, and ${}^{23}\text{Na}$ ”, *Phys. Rev. A* **51**, 4852 (1995).
- [79] N. R. Claussen, S. J. J. M. F. Kokkelmans, S. T. Thompson, E. A. Donley, E. Hodby, and C. E. Wieman, “Very-high-precision bound-state spectroscopy near a ${}^{85}\text{Rb}$ Feshbach resonance”, *Phys. Rev. A* **67**, 060701 (2003).
- [80] A. Marte, T. Volz, J. Schuster, S. Dürr, G. Rempe, E. G. M. van Kempen, and B. J. Verhaar, “Feshbach Resonances in Rubidium 87: Precision Measurement and Analysis”, *Phys. Rev. Lett.* **89**, 283202 (2002).
- [81] T. Volz, S. Dürr, S. Ernst, A. Marte, and G. Rempe, “Characterization of elastic scattering near a Feshbach resonance in ${}^{87}\text{Rb}$ ”, *Phys. Rev. A* **68**, 010702 (2003).
- [82] S. Inouye, M. R. Andrews, J. Stenger, H. J. Miesner, D. M. Stamper-Kurn, and W. Ketterle, “Observation of Feshbach resonances in a Bose-Einstein condensate”, *Nature* **392**, 151 (1998).
- [83] S. Jochim, M. Bartenstein, G. Hendl, J. H. Denschlag, R. Grimm, A. Mosk, and M. Weidemüller, “Magnetic Field Control of Elastic Scattering in a Cold Gas of Fermionic Lithium Atoms”, *Phys. Rev. Lett.* **89**, 273202 (2002).
- [84] C. Chin, V. Vuletic, A. J. Kerman, S. Chu, E. Tiesinga, P. J. Leo, and C. J. Williams, “Precision Feshbach spectroscopy of ultracold Cs_2 ”, *Phys. Rev. A* **70**, 032701 (2004).
- [85] C. A. Regal and D. S. Jin, “Measurement of Positive and Negative Scattering Lengths in a Fermi Gas of Atoms”, *Phys. Rev. Lett.* **90**, 230404 (2003).

- [86] C. D’Errico, M. Zaccanti, M. Fattori, G. Roati, M. Inguscio, G. Modugno, and A. Simoni, “Feshbach resonances in ultracold ^{39}K ”, *e-print: Arxiv* 0705.3036v1 (2007).
- [87] J. Werner, A. Griesmaier, S. Hensler, J. Stuhler, T. Pfau, A. Simoni, and E. Tiesinga, “Observation of Feshbach Resonances in an Ultracold Gas of ^{52}Cr ”, *Phys. Rev. Lett.* **94**, 183201 (2005).
- [88] F. Ferlaino, C. D’Errico, G. Roati, M. Zaccanti, M. Inguscio, G. Modugno, and A. Simoni, “Erratum: Feshbach spectroscopy of a K-Rb atomic mixture [Phys. Rev. A **73**, 040702 (2006)]”, *Phys. Rev. A* **74**, 039903 (2006).
- [89] S. Inouye, J. Goldwin, M. L. Olsen, C. Ticknor, J. L. Bohn, and D. S. Jin, “Observation of Heteronuclear Feshbach Resonances in a Mixture of Bosons and Fermions”, *Phys. Rev. Lett.* **93**, 183201 (2004).
- [90] C. A. Stan, M. W. Zwierlein, C. H. Schunck, S. M. F. Raupach, and W. Ketterle, “Observation of Feshbach Resonances between Two Different Atomic Species”, *Phys. Rev. Lett.* **93**, 143001 (2004).
- [91] S. T. Thompson, E. Hodby, and C. E. Wieman, “Ultracold Molecule Production via a Resonant Oscillating Magnetic Field”, *Phys. Rev. Lett.* **95**, 190404 (2005).
- [92] J. P. D’Incao and B. D. Esry, “Scattering Length Scaling Laws for Ultracold Three-Body Collisions”, *Phys. Rev. Lett.* **94**, 213201 (2005).
- [93] C. Regal and D. S. Jin, “Experimental realization of BCS-BEC crossover physics with a Fermi gas of atoms (Cindy Regal’s PhD thesis)”, *e-print: Arxiv cond-mat/0601054* (2006).
- [94] M. W. Zwierlein, C. H. Schunck, A. Schirotzek, and W. Ketterle, “Direct observation of the superfluid phase transition in ultracold Fermi gases”, *Nature* **442**, 54 (2006).
- [95] M. W. Zwierlein, J. R. Abo-Shaeer, A. Schirotzek, C. H. Schunck, and W. Ketterle, “Vortices and superfluidity in a strongly interacting Fermi gas”, *Nature* **435**, 1047 (2005).
- [96] B. Marcelis, E. G. M. van Kempen, B. J. Verhaar, and S. J. J. M. F. Kokkelmans, “Feshbach resonances with large background scattering length: Interplay with open-channel resonances”, *Phys. Rev. A* **70**, 012701 (2004).
- [97] J. Herbig, T. Kraemer, M. Mark, T. Weber, C. Chin, H.-C. Nägerl, and R. Grimm, “Preparation of a Pure Molecular Quantum Gas”, *Science* **301**, 1510 (2003).

- [98] K. Xu, T. Mukaiyama, J. R. Abo-Shaeer, J. K. Chin, D. E. Miller, and W. Ketterle, “Formation of Quantum-Degenerate Sodium Molecules”, *Phys. Rev. Lett.* **91**, 210402 (2003).
- [99] S. Dürr, T. Volz, A. Marte, and G. Rempe, “Observation of Molecules Produced from a Bose-Einstein Condensate”, *Phys. Rev. Lett.* **92**, 020406 (2004).
- [100] M. Greiner, C. A. Regal, and D. S. Jin, “Emergence of a molecular Bose-Einstein condensate from a Fermi gas”, *Nature* **426**, 537 (2003).
- [101] S. Jochim, M. Bartenstein, A. Altmeyer, G. Hendl, S. Riedl, C. Chin, J. Hecker Denschlag, and R. Grimm, “Bose-Einstein Condensation of Molecules”, *Science* **302**, 2101 (2003).
- [102] E. Hodby, S. T. Thompson, C. A. Regal, M. Greiner, A. C. Wilson, D. S. Jin, E. A. Cornell, and C. E. Wieman, “Production Efficiency of Ultracold Feshbach Molecules in Bosonic and Fermionic Systems”, *Phys. Rev. Lett.* **94**, 120402 (2005).
- [103] K. Góral, T. Köhler, S. A. Gardiner, E. Tiesinga, and P. S. Julienne, “Adiabatic association of ultracold molecules via magnetic-field tunable interactions”, *Journal of Physics B: Atomic, Molecular and Optical Physics* **37**, 3457 (2004).
- [104] C. A. Regal, M. Greiner, and D. S. Jin, “Lifetime of Molecule-Atom Mixtures near a Feshbach Resonance in K”, *Phys. Rev. Lett.* **92**, 083201 (2004).
- [105] D. S. Petrov, C. Salomon, and G. V. Shlyapnikov, “Weakly Bound Dimers of Fermionic Atoms”, *Phys. Rev. Lett.* **93**, 090404 (2004).
- [106] S. Fölling, A. Widera, T. Müller, F. Gerbier, and I. Bloch, “Formation of Spatial Shell Structure in the Superfluid to Mott Insulator Transition”, *Phys. Rev. Lett.* **97**, 060403 (2006).
- [107] G. Thalhammer, K. Winkler, F. Lang, S. Schmid, R. Grimm, and J. H. Denschlag, “Long-Lived Feshbach Molecules in a Three-Dimensional Optical Lattice”, *Phys. Rev. Lett.* **96**, 050402 (2006).
- [108] C. Ospelkaus, S. Ospelkaus, L. Humbert, P. Ernst, K. Sengstock, and K. Bongs, “Ultracold Heteronuclear Molecules in a 3D Optical Lattice”, *Phys. Rev. Lett.* **97**, 120402 (2006).
- [109] K. Winkler, F. Lang, G. Thalhammer, P. v. d. Straten, R. Grimm, and J. H. Denschlag, “Coherent Optical Transfer of Feshbach Molecules to a Lower Vibrational State”, *Phys. Rev. Lett.* **98**, 043201 (2007).

- [110] D. Jaksch, V. Venturi, J. I. Cirac, C. J. Williams, and P. Zoller, “Creation of a Molecular Condensate by Dynamically Melting a Mott Insulator”, *Phys. Rev. Lett.* **89**, 040402 (2002).
- [111] D. Steck, “Rubidium 87 D Line Data”, Available online at <http://www.steck.us/alkalidata> (2003).
- [112] H. J. Metcalf and P. van der Straten, *Laser Cooling and Trapping* (Springer, New York, 1999).
- [113] A. M. Steane, M. Chowdhury, and C. J. Foot, “Radiation force in the magneto-optical trap”, *J. Opt. Soc. Am. B* **9**, 2142 (1992).
- [114] P. J. Ungar, D. S. Weiss, E. Riis, and S. Chu, “Optical molasses and multilevel atoms: theory”, *J. Opt. Soc. Am. B* **6**, 2058 (1989).
- [115] D. S. Weiss, E. Riis, Y. Shevy, P. J. Ungar, and S. Chu, “Optical molasses and multilevel atoms: experiment”, *J. Opt. Soc. Am. B* **6**, 2072 (1989).
- [116] P. D. Lett, W. D. Phillips, S. L. Rolston, C. E. Tanner, R. N. Watts, and C. I. Westbrook, “Optical molasses”, *J. Opt. Soc. Am. B* **6**, 2084 (1989).
- [117] K. B. MacAdam, A. Steinbach, and C. Wieman, “A narrow-band tunable diode laser system with grating feedback, and a saturated absorption spectrometer for Cs and Rb”, *American Journal of Physics* **60**, 1098 (1992).
- [118] C. Wieman, G. Flowers, and S. Gilbert, “Inexpensive laser cooling and trapping experiment for undergraduate laboratories”, *American Journal of Physics* **63**, 317 (1995).
- [119] C. E. Wieman and L. Hollberg, “Using diode lasers for atomic physics”, *Review of Scientific Instruments* **62**, 1 (1991).
- [120] E. D. Black, “An introduction to Pound-Drever-Hall laser frequency stabilization”, *American Journal of Physics* **69**, 79 (2001).
- [121] U. Schünemann, H. Engler, R. Grimm, M. Weidemüller, and M. Zielonkowski, “Simple scheme for tunable frequency offset locking of two lasers”, *Review of Scientific Instruments* **70**, 242 (1999).
- [122] G. Breit and I. I. Rabi, “Measurement of Nuclear Spin”, *Phys. Rev.* **38**, 2082 (1931).
- [123] W. H. Wing, “On neutral particle trapping in quasistatic electromagnetic fields”, *Progress in Quantum Electronics* **8**, 181 (1984).

- [124] T. Bergeman, G. Erez, and H. J. Metcalf, “Magnetostatic trapping fields for neutral atoms”, *Phys. Rev. A* **35**, 1535 (1987).
- [125] W. Petrich, M. H. Anderson, J. R. Ensher, and E. A. Cornell, “Stable, Tightly Confining Magnetic Trap for Evaporative Cooling of Neutral Atoms”, *Phys. Rev. Lett.* **74**, 3352 (1995).
- [126] M. Greiner, I. Bloch, T. W. Hänsch, and T. Esslinger, “Magnetic transport of trapped cold atoms over a large distance”, *Phys. Rev. A* **63**, 031401 (2001).
- [127] T. Esslinger, I. Bloch, and T. W. Hänsch, “Bose-Einstein condensation in a quadrupole-Ioffe-configuration trap”, *Phys. Rev. A* **58**, R2664 (1998).
- [128] O. J. Luiten, M. W. Reynolds, and J. T. M. Walraven, “Kinetic theory of the evaporative cooling of a trapped gas”, *Phys. Rev. A* **53**, 381 (1996).
- [129] T. H. Bergeman, P. McNicholl, J. Kycia, H. Metcalf, and N. L. Balazs, “Quantized motion of atoms in a quadrupole magnetostatic trap”, *J. Opt. Soc. Am. B* **6**, 2249 (1989).
- [130] J. P. Burke, J. L. Bohn, B. D. Esry, and C. H. Greene, “Prospects for Mixed-Isotope Bose-Einstein Condensates in Rubidium”, *Phys. Rev. Lett.* **80**, 2097 (1998).
- [131] U. Schünemann, H. Engler, M. Zielonkowski, M. Weidemüller, and R. Grimm, “Magneto-optic trapping of lithium using semiconductor lasers”, *Optics Communications* **158**, 263 (1998).
- [132] T. Busch, B. G. Englert, K. Rzazewski, and M. Wilkens, “Two cold atoms in a harmonic trap”, *Foundations of Physics* **28**, 549 (1998).
- [133] B. Borca, D. Blume, and C. H. Greene, “A two-atom picture of coherent atom-molecule quantum beats”, *New Journal of Physics* **5**, 111 (2003).
- [134] M. Block and M. Holthaus, “Pseudopotential approximation in a harmonic trap”, *Phys. Rev. A* **65**, 052102 (2002).
- [135] D. Blume and C. H. Greene, “Fermi pseudopotential approximation: Two particles under external confinement”, *Phys. Rev. A* **65**, 043613 (2002).
- [136] E. Tiesinga, C. J. Williams, F. H. Mies, and P. S. Julienne, “Interacting atoms under strong quantum confinement”, *Phys. Rev. A* **61**, 063416 (2000).

- [137] E. L. Bolda, E. Tiesinga, and P. S. Julienne, “Effective-scattering-length model of ultracold atomic collisions and Feshbach resonances in tight harmonic traps”, *Phys. Rev. A* **66**, 013403 (2002).
- [138] Y. Chen and B. Gao, “Multiscale quantum-defect theory for two interacting atoms in a symmetric harmonic trap”, *Phys. Rev. A* **75**, 053601 (2007).
- [139] F. Deuretzbacher, K. Plassmeier, D. Pfannkuche, F. Werner, C. Ospelkaus, S. Ospelkaus, K. Sengstock, and K. Bongs, “Heteronuclear molecules in an optical lattice: Theory and experiment”, *e-print: Arxiv cond-mat/0703322* (2007).
- [140] K. Huang, *Statistical Mechanics* (John Wiley & Sons, New York, 1963).
- [141] K. Huang and C. N. Yang, “Quantum-Mechanical Many-Body Problem with Hard-Sphere Interaction”, *Phys. Rev.* **105**, 767 (1957).
- [142] Y. Castin, “Bose-Einstein condensates in atomic gases: simple theoretical results”, *e-print: Arxiv cond-mat/0105058* (2001).
- [143] R. Stock, A. Silberfarb, E. L. Bolda, and I. H. Deutsch, “Generalized Pseudopotentials for Higher Partial Wave Scattering”, *Phys. Rev. Lett.* **94**, 023202 (2005).
- [144] A. Derevianko, J. F. Babb, and A. Dalgarno, “High-precision calculations of van der Waals coefficients for heteronuclear alkali-metal dimers”, *Phys. Rev. A* **63**, 052704 (2001).
- [145] B. H. Bransden and C. J. Joachain, *Introduction to Quantum Mechanics*, 2nd ed. (John Wiley & Sons, New York, 1989).
- [146] M. Abramowitz and I. A. Stegun, *Handbook of Mathematical Functions with Formulas, Graphs, and Mathematical Tables* (Dover, New York, 1965).
- [147] M. P. Avakian, G. S. Pogosyan, A. N. Sissakian, and V. M. Ter-Antonyan, “Spectroscopy of a Singular Linear Oscillator”, *Physics Letters A* **124**, 233 (1987).
- [148] M. Greiner, C. A. Regal, and D. S. Jin, “Probing the Excitation Spectrum of a Fermi Gas in the BCS-BEC Crossover Regime”, *Phys. Rev. Lett.* **94**, 070403 (2005).
- [149] S. B. Papp and C. E. Wieman, “Observation of Heteronuclear Feshbach Molecules from a ^{85}Rb - ^{87}Rb Gas”, *Phys. Rev. Lett.* **97**, 180404 (2006).

- [150] J. P. Gaebler, J. T. Stewart, J. L. Bohn, and D. S. Jin, “p-Wave Feshbach Molecules”, *Phys. Rev. Lett.* **98**, 200403 (2007).
- [151] C. A. Regal, C. Ticknor, J. L. Bohn, and D. S. Jin, “Creation of ultracold molecules from a Fermi gas of atoms”, *Nature* **424**, 47 (2003).
- [152] S. Gupta, Z. Hadzibabic, M. W. Zwierlein, C. A. Stan, K. Dieckmann, C. H. Schunck, E. G. M. van Kempen, B. J. Verhaar, and W. Ketterle, “Radio-Frequency Spectroscopy of Ultracold Fermions”, *Science* **300**, 1723 (2003).
- [153] T. M. Hanna, T. Kohler, and K. Burnett, “Association of molecules using a resonantly modulated magnetic field”, *Phys. Rev. A* **75**, 013606 (2007).
- [154] E. A. Donley, N. R. Claussen, S. T. Thompson, and C. E. Wieman, “Atom-molecule coherence in a Bose-Einstein condensate”, *Nature* **417**, 529 (2002).
- [155] C. Ryu, X. Du, E. Yesilada, A. M. Dudarev, S. Wan, Q. Niu, and D. Heinzen, “Raman-induced oscillation between an atomic and a molecular quantum gas”, *e-print: Arxiv cond-mat/0508201* (2005).
- [156] N. Syassen, D. M. Bauer, M. Lettner, D. Dietze, T. Volz, S. Dürr, and G. Rempe, “Atom-Molecule Rabi Oscillations in a Mott Insulator”, *Phys. Rev. Lett.* **99**, 033201 (2007).
- [157] M. Mark, T. Krämer, P. Waldburger, J. Herbig, C. Chin, H.-C. Nägerl, and R. Grimm, ““Stückelberg Interferometry” with Ultracold Molecules”, *Phys. Rev. Lett.* **99**, 113201 (2007).
- [158] J. P. Gaebler, J. T. Stewart, and D. S. Jin, *Private Communication* (2006).
- [159] S. B. Papp, *Private Communication* (2006).
- [160] T. Volz, S. Dürr, N. Syassen, G. Rempe, E. van Kempen, and S. Kokkelmans, “Feshbach spectroscopy of a shape resonance”, *Phys. Rev. A* **72**, 010704 (2005).
- [161] S. Dürr, T. Volz, N. Syassen, G. Rempe, E. van Kempen, S. Kokkelmans, B. Verhaar, and H. Friedrich, “Dissociation of Feshbach molecules into different partial waves”, *Phys. Rev. A* **72**, 052707 (2005).
- [162] B. H. Bransden and C. J. Joachain, *Physics of Atoms and Molecules*, 2nd ed. (Pearson Education, Essex, 2003).
- [163] I. S. Gradshteyn and I. M. Ryzhik, *Table of Integrals, Series, and Products* (Academic Press, New York, 1965).